Quantum Effects and Dynamics in Hydrogen-Bonded Systems: A First-Principles Approach to Spectroscopic Experiments

Dissertation zur Erlangung des Grades

"Doktor der Naturwissenschaften"

am Fachbereich Physik
der Johannes Gutenberg-Universität
in Mainz

Jochen Schmidt
geboren in Mainz

Mainz 2007

Tag der mündlichen Prüfung: 14.09.2007

Contents

1 Introduction **1**

2 Basic Theory **5**

2.1 Density Functional Theory 5

2.1.1 Motivation 5

2.1.2 The Born-Oppenheimer Approximation 7

2.1.3 The Hohenberg-Kohn Theorem 9

2.1.4 The Kohn-Sham Method 14

2.1.5 The Local-Density Approximation 18

2.1.6 Gradient Corrected functionals 19

2.2 Pseudopotentials and Basis Sets 21

2.2.1 The Pseudopotential Approximation 21

2.2.2 Basis sets 23

2.3 Computational Realizations 27

2.3.1 Gaussian and Plane Waves Method (GPW) 27

2.3.2 Gaussian and Augmented Plane Waves Method (GAPW) . 30

2.4 Molecular Dynamics Simulations 34

2.4.1 Overview 34

2.4.2 Born-Oppenheimer MD 35

2.4.3 Car-Parrinello MD 36

2.4.4 Realization of the NVT-Ensemble 38

3 Calculation of Spectroscopic Properties **41**

3.1 Introduction 41

3.2 Ground State Properties 43

3.2.1 Nuclear Quadrupole Coupling Constants (NQCC) 43

3.2.2 Calculation of Electric Field Gradients 47

3.2.3 Relaxation via Quadrupole Couplings 49
3.3 Second-Order Properties 53
3.3.1 General 53
3.3.2 Chemical Shifts 54
3.3.3 The gauge origin problem 56

4 The Path Integral Formalism 59
4.1 Motivation 59
4.2 Formal Derivation of Path Integrals 61
4.3 Path Integrals in MD Simulations 64
4.3.1 Representation with Ring Polymers 64
4.3.2 The Staging Transformation 65
4.3.3 Finite-Discretization Errors 67

5 Nuclear Quantum Effects in Molecular Systems 69
5.1 Motivation 69
5.2 Staging Transformation and Spectroscopic Properties 71
5.3 Tunneling Effects in Acetylacetone 77
5.3.1 Introduction 77
5.3.2 Proton Density from a Path Integral Simulation 78
5.3.3 Electric Field Gradients: Classic vs. Quantum MD 83
5.3.4 NMR: Classical vs. Quantum MD 86
5.4 Nuclear quadrupole couplings in benzoic acid 91
5.4.1 Introduction 91
5.4.2 Quantum effects on the NQCC 93
5.5 Conclusions 96

6 Quadrupole Relaxation in Water 99
6.1 Introduction 99
6.2 EFG in GAPW - Tests and Benchmarks 100
6.3 MD Simulation of Liquid Water 103
6.4 Autocorrelation and Relaxation 107
6.5 Conclusions 117

7 Constant Pressure Simulations **119**
7.1 Theoretical Background 119
7.1.1 Motivation 119
7.1.2 Basic Thermodynamics 120
7.1.3 Stress-Tensor 122
7.1.4 Pressure and Periodic Boundary Conditions 127
7.2 Stress Tensor in the GPW framework 128
7.2.1 Forces in GPW 128
7.2.2 Grid Independent Terms of the Stress Tensor 132
7.2.3 Grid Dependent Terms of the Stress Tensor 133
7.2.4 Test of the Implementation 138
7.3 Simulation of Liquid Water at Ambient Conditions 139
7.3.1 Prelude: The NPT Integrator 139
7.3.2 Introduction 141
7.3.3 Technical Details 142
7.3.4 Results 144
7.4 Conclusions 155

8 Summary and Outlook **157**

A Derivation of the Stress Tensor **161**

B Technical Details: Simulations **164**

C Technical Details: NMR Measurements **165**

D Atomic units **167**

E Abbreviations **169**

Bibliography **170**

1 Introduction

The year 1985 can be considered a milestone for the field of computational materials science. Car and Parrinello published their "Unified Approach for Molecular Dynamics and Density-Functional Theory" [1]. This work provided a novel basis for molecular dynamics simulations based on a potential energy surface computed from electronic structure, nowadays known as "Car-Parrinello molecular dynamics". Secondly, Cray Research released the Cray-2 supercomputer, yielding a performance of 3.9 GigaFLOPS[1], which was not outperformed by another machine until 1990. Starting in the late 80's, the power of the new techniques, both conceptual and technical, led to an explosion of the activity in this field. 22 years later, the fastest supercomputer is BlueGene/L with 280 TeraFLOPS. Interestingly, both Cray-2 and BlueGene/L have been built for the Lawrence Livermore National Laboratory, where also a part of this work has been conducted.

While the Cray-2 cannot be found on 2007's TOP500 list of the fastest supercomputers[2], the Car-Parrinello method is still in widespread use. By July 2007, the original paper has been cited in more than 4000 publications. The first applications of ab-initio molecular dynamics were limited to a few atoms and several tens of femtoseconds, both using the Car-Parrinello method and other approaches, such as Born-Oppenheimer molecular dynamics. Modern computer clusters, such as BlueGene/L, which provides the impressive number of 131,000 processors, enable the ab-initio treatment of thousands of atoms and simulation times up to several nanoseconds. This has been achieved by pure computational power on the one hand, but also by developing efficient and sophisticated algorithms. "Linear scaling techniques" that circumvent the cubic scaling with the system size exhibited by many conventional schemes, are mentioned here as an example that

[1] Floating Point Operations Per Second
[2] see `http://www.top500.org/`

opens the way for the modeling of biological systems. Before, these have been accessible only with the help of methods that use empirical and pre-parameterized potentials.

Typically, a molecular dynamics simulation is carried out for investigating the energetics and structure of a system under conditions that include physical parameters such as temperature and pressure. Ab initio quantum chemical methods, which form the basis of the dynamics scheme, have also proven to be capable of predicting other experimentally accessible quantities, e.g. spectroscopic parameters. Still, the combination of these two features, dynamics simulations and property calculations, is not commonly used, although it provides valuable information, for instance the temperature dependence of the parameters. This is due to the fact that both types of calculations are computationally very demanding, leading to an immense effort for the combined scheme.

Furthermore, conventional molecular dynamics consider the nuclei as classical particles that are subject to the forces created by the potential due to the quantum mechanically treated electrons. Not only motional effects, but also the quantum nature of the nuclei are expected to influence the properties of a molecular system. This has already been investigated using approximate methods, but a scheme based on path integrals provides a computational method for the rigorous inclusion of such effects at a high level of accuracy.

In this work, the computational methods mentioned above have been combined, aiming for a more realistic and complete description of properties that are accessible via NMR[3] experiments, such as the NMR chemical shift or Nuclear Quadrupole Coupling Constants. Isotope effects, caused by the quantum mechanical behavior of the involved particles, are well known and experimentally observed in NMR. Here, a computational approach for handling them, based on ab-initio path integral methods is presented, allowing a direct comparison to the respective experiments. With the help of efficiently parallelized computer codes, a consistent description on the first-principles level of theory could be achieved, leading to quantitative agreement with the experiment.

Besides the disregard of nuclear quantum effects, pseudopotentials are commonly

[3] Nuclear Magnetic Resonance

used. These treat the core electrons of an atom as a contribution to an effective potential, leading to computational savings because only the valence electrons have to be taken into account explicitly in the actual simulation. Especially in the solid state, where periodic boundary conditions are applied, this method is crucial. Unfortunately, for the calculation of spectroscopic properties, this approach is not sufficient. This holds in particular for spectroscopic parameters which are sensitive to the interaction of nuclei with the core electrons. Therefore, in the second part of this work, a new method for all-electron calculations in periodic systems has been used for the evaluation of quadrupole interactions that lead to relaxation in water, both for ^{17}O and ^{2}H. Again, this scheme has been combined with molecular dynamics simulations, allowing for a realistic description of the dynamics and therefore the relaxation mechanisms.

In the last part of this work, a technical contribution to the development of the quantum chemical program package CP2K[4] has been made. This code employs a newly developed method that combines the advantages of different basis sets, leading to a speed-up of the calculations and also allowing for sophisticated schemes as the above mentioned all-electron calculations. Such calculations are supposed to resemble the experiment, which in many cases is carried out under ambient conditions, i.e. temperature and pressure are defined by the environment. Therefore, the calculation of the internal pressure of a computed system is necessary, which has been implemented in this work. Subsequently, water under ambient conditions has been simulated using the new routines.

[4] more information at `http://cp2k.berlios.de/`

2 Basic Theory

2.1 Density Functional Theory

2.1.1 Motivation

The ab-initio description of molecular systems in a quantum mechanical framework commonly starts with the Schrödinger equation. Theories that include spin and relativistic effects are available, e.g. Pauli or Dirac equation, but they are used rarely because for most compounds the Schrödinger equation is sufficient. For a system consisting of n electrons and N nuclei, it is given by:

$$\mathcal{H}\chi(\boldsymbol{r}_1,\ldots,\boldsymbol{r}_n,\boldsymbol{R}_1,\ldots\boldsymbol{R}_N) = E\chi(\boldsymbol{r}_1,\ldots,\boldsymbol{r}_n,\boldsymbol{R}_1,\ldots\boldsymbol{R}_N)\ . \tag{2.1}$$

The Hamiltonian $\mathcal{H}$ is defined as

$$\begin{aligned}\mathcal{H} \;=\; & \sum_i -\frac{\hbar^2}{2m_e}\nabla_i^2 + \sum_I -\frac{\hbar^2}{2M_I}\nabla_I^2 + \frac{1}{2}\sum_{i\neq j}\frac{e^2}{|\boldsymbol{r}_i-\boldsymbol{r}_j|} + \\ & \frac{1}{2}\sum_{I\neq J}\frac{e^2Q_IQ_J}{|\boldsymbol{R}_I-\boldsymbol{R}_J|} - \sum_{iI}\frac{e^2Q_I}{|\boldsymbol{r}_i-\boldsymbol{R}_I|}\ .\end{aligned} \tag{2.2}$$

Electrons are denoted by small indices (i), nuclei by capital ones (I), $\boldsymbol{r}$ and $\boldsymbol{R}$ are the position operators of the electrons and nuclei, respectively[1]. M is the nuclear mass, m_e the mass of the electron, Q and e are the charges of the nuclei and electrons. Here, gaussian units are used, but in lateron, *atomic units* will be introduced.

The Schrödinger equation suggests, that the exact wave function is the most straightforward quantity to use in quantum chemical calculations. But actually, it turns out to be difficult to handle and inconvenient for a practical computation.

[1] Throughout this work vectors are printed in bold letters.

Let a model system consist of 10 particles. It is described by a wave function of the form

$$\chi(\boldsymbol{r}_1, \boldsymbol{r}_2, \ldots, \boldsymbol{r}_{10}). \tag{2.3}$$

During a numerical calculation, this wave function has to be stored on a spatial grid. If each axis is represented by only 10 points and each value of χ is given by a 10 bytes variable, the needed total data capacity is:

$$10\ \frac{\text{bytes}}{\text{point}} \times \left(10\ \frac{\text{points}}{\text{axis}}\right)^{3\text{axes}\times 10\text{particles}} \quad = \quad 10^{31}\ \text{bytes}. \tag{2.4}$$

That means, that the storage of this wave function on DVDs, each being capable of 10 GB, requires 10^{21} DVDs. One DVD weighs about 10 grams, resulting in a total weight of 10^{16} tons. If these disks were shipped with trucks with a length of 10 m, each carrying 10 tons, they would line up to 10^{13} km, corresponding to 100,000 times the distance between sun and earth.

Although the capacity of modern storage media is increasing rapidly, such an amount of data will cause severe problems. Thus, approximations are needed to reduce the data, that are actually needed during the calculation. Most of these methods are based on the fact, that anti-symmetric many-particle wave functions can be written as a linear combination of Slater determinats of atomic basis functions. So, the first approach is to express the wave function as *single* Slater determinant of the occupied atomic states, which is referred to as *Hartree-Fock wave function*. Starting from this, several improvements are possible. A natural extension is the usage of additional, unoccupied states or the description of the wave function by a sum of determinants. In principle, that is the idea of the *Confuguration-Interaction-* or the *Coupled-Cluster Method*. These can treat molecular systems with a high accuracy. The *Møller-Plesset Theory*, on the other hand, includes many-particle effects as quantum mechanical perturbations. A detailed introduction to these techniques can be found in Ref. [2].

The above-mentioned methods are referred to as *Post-Hartree-Fock methods*. They can yield highly accurate results, but require an enormous computational effort. Therefore, they are limited to relatively small systems. The *Density Functional Theory* (DFT) follows a different approach where only the probability den-

sity

$$\rho(\boldsymbol{r}) = n \int \cdots \int |\chi(\boldsymbol{r}, \boldsymbol{r}_2, \ldots, \boldsymbol{r}_n)|^2 \; d\boldsymbol{r}_2 \cdots d\boldsymbol{r}_n \tag{2.5}$$

instead of the whole wave function is used. The density is a function of only *one* position variable, but according to the *Hohenberg-Kohn Theorem* it contains the same information as the wave function. Or, putting it the other way around, the wave function, that depends on $3n$ variables, plus n spin variables, contains more information than is actually needed, because the Hamiltonian of Eq. (2.2) consists of only one- and two-electron spatial terms.

2.1.2 The Born-Oppenheimer Approximation

The Schrödinger equation contains nuclear and electronic degrees of freedom and both are treated under equal footing. Thus, the wave function of the systems also depends on the positions of the electrons and nuclei. While both types of particles appear to be similar in theory, there is a significant difference: The masses are separated by several orders of magnitude. For instance, the proton mass is approximately 2000 times larger than the mass of an electron. This fact allows for a further simplification of the problem, often referred to as the *Born-Oppenheimer approximation* [3].

In the first step, a new parameter is introduced, which only depends on the masses of the involved particles:

$$\kappa = \frac{m_e}{M} \; . \tag{2.6}$$

In this equation M can be one of the ionic masses M_I. For simplification, it will be assumed in the following, that $M_I = M$ for all I. Using the new parameter κ, the Hamiltonian of Eq. (7.1) can be rewritten. Therefore, some abbreviations have to be defined:

$$\begin{aligned} \mathcal{H} &= \sum_i -\frac{\hbar^2}{2m_e}\nabla_i^2 + \sum_I -\frac{\hbar^2}{2M_I}\nabla_I^2 + \frac{1}{2}\sum_{i\neq j}\frac{e^2}{|\boldsymbol{r}_i - \boldsymbol{r}_j|} + \\ &\quad \frac{1}{2}\sum_{I\neq J}\frac{e^2 Q_I Q_J}{|\boldsymbol{R}_I - \boldsymbol{R}_J|} - \sum_{iI}\frac{e^2 Q_I}{|\boldsymbol{r}_i - \boldsymbol{R}_I|} \\ &= \mathcal{T}_E + \mathcal{T}_N + \mathcal{U} \;=\; \mathcal{H}_0 + \mathcal{T}_N \; . \end{aligned} \tag{2.7}$$

Using these equations, the kinetic energy of the ions $\mathcal{T}_N$ is

$$\mathcal{T}_N = \kappa\mathcal{H}_1, \qquad \mathcal{H}_1 = \sum_I -\frac{\hbar^2}{2m_e}\nabla_I^2 \ . \tag{2.8}$$

The Hamiltonian $\mathcal{H}$ thus reads

$$\mathcal{H} = \mathcal{H}_0 + \kappa\mathcal{H}_1 \ . \tag{2.9}$$

Since $\kappa \ll 1$, the ionic kinetic energy can be treated as perturbation. From this approximation, it can be found that the evolution of the nuclei is decoupled from the electronic degrees of freedom. Thus, the total wave function can be written as a product of an electronic and a nuclear wave function:

$$\chi(\boldsymbol{r}_1, \ldots, \boldsymbol{r}_n, \boldsymbol{R}_1, \ldots, \boldsymbol{R}_N) = \Psi_{R_1,\ldots,R_N}(\boldsymbol{r}_1, \ldots, \boldsymbol{r}_n)\ \xi(\boldsymbol{R}_1, \ldots, \boldsymbol{R_N}) \ . \tag{2.10}$$

This is referred to as the Born-Oppenheimer approximation. The positions of the nuclei $\{\boldsymbol{R}_1, \ldots \boldsymbol{R}_N\}$ are only parameters in the electronic wave function. Furthermore, the nuclei will be treated as classical point-particles. This is done in the framework of the WKB[2] method, which will not be explained in detail here. An introduction to that can be found in [4]. The dynamics of the nuclei can thus be described by a Newtonian equation of motion, i.e.

$$M_I\ddot{\boldsymbol{R}}_I = -\nabla_I \int d\boldsymbol{r}\ \Psi^*\mathcal{H}_0\Psi \ . \tag{2.11}$$

In conclusion, it can be stated, that the nuclei are moving as classical particles in an effective potential, that is created by the electrons. The electrons are the only particles that are treated quantum mechanically here, but later on, there are special cases where the nuclei have to be included in the quantum mechanical framework via the *path integral method* (see Chapter 4). Employing this approximation, which is justified in many cases, only the following Schrödinger equation for the electrons has to be solved:

$$\mathcal{H}^{el}\Psi_{R_1,\ldots,R_N}(\boldsymbol{r}_1, \ldots, \boldsymbol{r}_n) = E_{R_1,\ldots,R_N}\Psi_{R_1,\ldots,R_N}(\boldsymbol{r}_1, \ldots, \boldsymbol{r}_n) \ , \tag{2.12}$$

[2] developed by G. Wentzel, H. A. Kramers and L. Brillouin

where

$$\begin{aligned}\mathcal{H}^{el} &= \sum_i -\frac{\hbar^2}{2m_e}\nabla_i^2 + \frac{1}{2}\sum_{i\neq j}\frac{e^2}{|\boldsymbol{r}_i-\boldsymbol{r}_j|} - \sum_{iI}\frac{e^2 Q_I}{|\boldsymbol{r}_i-\boldsymbol{R}_I|} \\ &= \sum_i -\frac{\hbar^2}{2m_e}\nabla_i^2 + \frac{1}{2}\sum_{i\neq j}\frac{e^2}{|\boldsymbol{r}_i-\boldsymbol{r}_j|} + \sum_i v_{ext}(\boldsymbol{r}_i)\ . \end{aligned} \tag{2.13}$$

In Eq. 2.13 the interaction between electrons and nuclei has been replaced by a generalized potential v_{ext}. Both the electronic wave function and the eigenvalues depend parametrically on the positions of the nuclei $\boldsymbol{R}_I$. In contrast to the total wave function from Eq. 2.1, χ, the number of degrees of freedom is $3n$ instead of $3N+3n$, which is a major improvement of the Born-Oppenheimer approximation compared to the exact problem. Eq. 2.13 is a time-independent Schrödinger equation for the electrons within the constant field of the nuclei. The dynamics of the latter is now described in the framework of classical Newtonian mechanics.

While the previous equations have used the Gaussian system of units, in the following sections, atomic units will be employed. The transition can be done by transforming the energy- and lengthscales in a way, that the electronic charge, mass and $\hbar$ do not appear explicitly in the equations anymore. Details can be found in Appendix D or [2]. The Hamiltonian then becomes:

$$\mathcal{H}^{el} = \sum_i -\frac{1}{2}\nabla_i^2 + \frac{1}{2}\sum_{i\neq j}\frac{1}{|\boldsymbol{r}_i-\boldsymbol{r}_j|} + \sum_i v_{ext}(\boldsymbol{r}_i)\ . \tag{2.14}$$

2.1.3 The Hohenberg-Kohn Theorem

As stated in Sec. 2.1.1, instead of the wave function, the electronic density can be used to describe a quantum mechanical system. Pierre Hohenberg and Walter Kohn showed in 1964 that these two possibilities are actually equivalent [5].

The Hohenberg-Kohn Theorem. *For systems with a nondegenerate ground state, the ground-state wave function* $\Psi_0(\boldsymbol{r}_1,...,\boldsymbol{r}_n)$ *and thus all properties that are based on the electronic structur are uniquely determined by the ground-state*

electronic density $\rho_0(\boldsymbol{r})$.

$$\Psi_0(\boldsymbol{r}_1, ..., \boldsymbol{r}_n) = \Psi_0[\rho_0(\boldsymbol{r})](\boldsymbol{r}_1, ..., \boldsymbol{r}_n) \tag{2.15}$$

$$\rho_0(\boldsymbol{r}) = n \int \cdots \int |\Psi_0(\boldsymbol{r}, \boldsymbol{r}_2, \ldots, \boldsymbol{r}_n)|^2 \, d\boldsymbol{r}_2 \cdots d\boldsymbol{r}_n \tag{2.16}$$

Here, $\Psi_0(\boldsymbol{r}_1, \cdots, \boldsymbol{r}_n)$ is already anti-symmetrized and normalized. Hence, it is not necessary to know the actual wave function of the system, the electronic density $\rho_0(\boldsymbol{r})$ is sufficient for the evaluation of properties, that depend on the electronic structure. Additionally, the number of degrees of freedom can be limited to three. Unfortunately it turns out, that some observables, e.g. the kinetic energy, cannot be assigned to a closed expression depending on the density.

The most important foundation for this theorem is the *Variational Theorem for the ground-state wave function*. It states, that ground-state wave function $\Psi_0(\boldsymbol{r}_1, ..., \boldsymbol{r}_n)$ is the wave function, that minimizes the energy functional

$$E[\Psi] = \frac{\langle \Psi | \mathcal{H} | \Psi \rangle}{\langle \Psi | \Psi \rangle} \ , \tag{2.17}$$

where

$$\langle \Psi | \mathcal{H} | \Psi \rangle = \int \Psi^* \mathcal{H} \Psi d\boldsymbol{r} \ . \tag{2.18}$$

If the ground state is nondegenerate, this means, that for each wave function $\Psi \neq \Psi_0$ the following equation holds:

$$E[\Psi] > E_0 = E[\Psi_0] \ . \tag{2.19}$$

According to Eq. (2.14), the Hamiltonian is uniquely determined by the potential $v_{ext}(\boldsymbol{r})$ (in the following simply denoted by $v(\boldsymbol{r})$) and the number of electrons n. Because of the above Variational Theorem, the wave function of the ground state with the Hamiltonian $\mathcal{H}^{el}$ is then determined, too. Thus, the wave function can be considered a functional of the external potential. In conclusion, the Hohenberg-Kohn Theorem states, that the external potential, i.e. *not* the Coulomb potential of the electrons themselves, is identified by the electronic density of the ground state.

The number of electrons n is given by density, which becomes clear, if Eq. (2.16) is integrated over the whole space and the normalization of the n-particle wave function $\Psi_0(\boldsymbol{r}_1, \ldots, \boldsymbol{r}_n)$ is taken into account:

$$\int \rho_0(\boldsymbol{r}) d\boldsymbol{r} = n \ . \tag{2.20}$$

Finally, the above statement that the potential $v(\boldsymbol{r})$ is determined by the electronic density has to be verified. Still, there will be the freedom of an additive, arbitrary constant in the potential, but this will be neglected in the following. It is now assumed, that there are *two* potentials $v(\boldsymbol{r})$ and $v'(\boldsymbol{r})$ that give rise to the same density $\rho(\boldsymbol{r})$. From now on, the index "0" will be omitted, i.e. ρ is equivalent to ρ_0. $\mathcal{H}$ and $\mathcal{H}'$ are Hamiltonians connected with v and v', respectively. Furthermore, Ψ and Ψ' are the corresponding ground-state wave functions, E_0 and E_0' the energies. The Variational Theorem for the wave function then gives:

$$E_0 = \langle \Psi | \mathcal{H} | \Psi \rangle < \langle \Psi' | \mathcal{H} | \Psi' \rangle \tag{2.21}$$

$$E_0' = \langle \Psi' | \mathcal{H}' | \Psi' \rangle < \langle \Psi | \mathcal{H}' | \Psi \rangle \ . \tag{2.22}$$

If Eq. (2.21) and Eq. (2.22) are added, one finds

$$\begin{aligned} E_0 + E_0' &< \langle \Psi' | \mathcal{H} | \Psi' \rangle + \langle \Psi | \mathcal{H}' | \Psi \rangle \\ &= \langle \Psi' | \mathcal{H}' | \Psi' \rangle + \langle \Psi' | \mathcal{H} - \mathcal{H}' | \Psi' \rangle \\ &\quad + \langle \Psi | \mathcal{H} | \Psi \rangle + \langle \Psi | \mathcal{H}' - \mathcal{H} | \Psi \rangle \\ 0 &< \langle \Psi' | \mathcal{H} - \mathcal{H}' | \Psi' \rangle + \langle \Psi | \mathcal{H}' - \mathcal{H} | \Psi \rangle \ . \end{aligned} \tag{2.23}$$

Since the operators $\mathcal{H}$ and $\mathcal{H}'$ only differ by the external potential, Eq. (2.23) can be written as

$$0 < \langle \Psi' | \sum_{i=1}^{n} (v(\boldsymbol{r}_i) - v'(\boldsymbol{r}_i)) | \Psi' \rangle + \langle \Psi | \sum_{i=1}^{n} (v'(\boldsymbol{r}_i) - v(\boldsymbol{r}_i)) | \Psi \rangle \ . \tag{2.24}$$

A one-particle operator $\mathcal{B}(\boldsymbol{r}_i)$, which is only a function of the coordinates x_i, y_i

and z_i, fulfills the equation (see [2, p. 423])

$$\langle\Psi|\sum_{i=1}^{n}\mathcal{B}(\boldsymbol{r}_i)|\Psi\rangle = \int \rho(\boldsymbol{r})\mathcal{B}(\boldsymbol{r})d\boldsymbol{r}\ . \tag{2.25}$$

Using this formula, Eq. (2.23) can be reformulated:

$$0 < \int \left[\rho'(\boldsymbol{r})(v(\boldsymbol{r}) - v'(\boldsymbol{r})) + \rho(\boldsymbol{r})(v'(\boldsymbol{r}) - v(\boldsymbol{r}))\right] d\boldsymbol{r}\ . \tag{2.26}$$

By hypothesis, the two different wave functions give the same electron density. So, the right side of Eq. (2.26) cancels and a contradiction is found:

$$0 < 0\ . \tag{2.27}$$

Thus, the initial assumption was wrong. The external potential, the Hamiltonian $\mathcal{H}^{el}$, the ground-state energy and many other properties of the system are uniquely determined by the density $\rho(\boldsymbol{r})$. The ground-state energy can now be written as a functional of the density:

$$E_0 = E_v[\rho] = \int \rho(\boldsymbol{r})v(\boldsymbol{r})d\boldsymbol{r} + T[\rho] + V_{ee}[\rho] = \int \rho(\boldsymbol{r})v(\boldsymbol{r})d\boldsymbol{r} + F[\rho]\ , \tag{2.28}$$

where the index "v" of the energy functional indicates, that the energy depends on the potential $v(\boldsymbol{r})$. $T[\rho]$ is the kinetic energy of the electrons, $V_{ee}[\rho]$ the Coulomb energy (also referred to as Hartree energy). Unfortunately, for these contributions, yielding $F[\rho]$, the actual functional form is unknown. Therefore, another method for calculating the energy and $\rho(\boldsymbol{r})$ itself is needed.

This method is based on a second theorem proven by Hohenberg and Kohn. It can be seen as a consequence of the above-mentioned Variational Principle for the ground-state wave function.

Variational Principle for the ground-state density. *For each trial density* $\rho'(\boldsymbol{r})$*, which satisfies*

$$\int \rho'(\boldsymbol{r})d\boldsymbol{r} = n \qquad \textit{and} \tag{2.29}$$

$$\rho'(\boldsymbol{r}) \geq 0 \tag{2.30}$$

for all $\boldsymbol{r}$*, the following inequality holds:*

$$E_0 = E_v[\rho] \leq E_v[\rho'] \ , \tag{2.31}$$

where ρ *is the true ground-state density and* $E_v[\cdot]$ *is the energy functional of Eq. (2.28).*

This can be shown as follows. Let ρ' satisfy the above two conditions. By the Hohenberg-Kohn theorem, ρ' determines the external potential v', and this in turn determines the wave function Ψ'. This wave function is now subject to the Variational Principle for the wave functions:

$$\langle \Psi' | \mathcal{H}^{el} | \Psi' \rangle \geq E_0 = E_v[\rho] \ . \tag{2.32}$$

Using the fact, that the kinetic and potential energies are functionals of the electron density, Eq. (2.32) becomes

$$E_v[\rho'] = \int \rho'(\boldsymbol{r}) v(\boldsymbol{r}) d\boldsymbol{r} + T[\rho'] + V_{ee}[\rho'] \geq E_v[\rho] \ . \qquad \square \tag{2.33}$$

The Variational Principle, now extended to the electron density, allows for the evaluation of both the ground-state density and the corresponding energy. This can be achieved by minimizing the energy functional, which makes DFT an interesting tool for quantum chemical calculations of molecular properties.

Finally, a requirement for the trial densities $\rho'(\boldsymbol{r})$ should be mentioned. The trial functions, that can be used for $\rho'(\boldsymbol{r})$ have to be limited to these ones, for which a potential v exists and which can be obtained from an anti-symmetrical wave function, that solves the Schrödinger equation with this potential. Such a density is called *v-representable*. It turns out, that not all $\rho'(\boldsymbol{r})$'s are v-representable. This has not caused any practical difficulties in applications of DFT. Also, Levy has reformulated the Hohenberg-Kohn theorems in a way that eliminated the need for v-representability. A detailed description of this problem can be found in [6].

2.1.4 The Kohn-Sham Method

The theorems of Hohenberg and Kohn show that it is possible to determine the ground-state energy and other molecular properties from the electronic ground-state density alone without actually knowing the wave function. Still, it has not been mentioned yet how to calculate the energy functional $E_v[\rho]$, even if the density is given. An important milestone in this quest was the development of the *Kohn-Sham (KS) method*, which was published in 1965 [7].

Kohn and Sham's method is based on a fictitious reference system of non-interacting electrons, which will be denoted by the index "s" in the following. It is introduced additionally to the considered real system of n electrons, which do interact with each other. The connection between these two sets of particles is the electron density. The fictitious electrons experience the potential energy $v_s(\boldsymbol{r}_i)$, where $v_s(\boldsymbol{r}_i)$ is such as to make the ground-state electron probability density $\rho_s(\boldsymbol{r})$ of the reference system equal to the exact ground-state electron density $\rho(\boldsymbol{r})$ of the molecule. According to the Hohenberg-Kohn theorem, the potential $v_s(\boldsymbol{r}_i)$ is known, once the density is determined. Since the particles do not interact anymore, the Hamiltonian $\mathcal{H}_s$ is simply a sum of one-particle operators:

$$\mathcal{H}_s = \sum_{i=1}^{n} \left[-\frac{1}{2}\nabla_i^2 + v_s(\boldsymbol{r}_i) \right] \equiv \sum_{i=1}^{n} h_i^{KS} \ , \tag{2.34}$$

where

$$h_i^{KS} \equiv -\frac{1}{2}\nabla_i^2 + v_s(\boldsymbol{r}_i) \ . \tag{2.35}$$

h_i^{KS} is the one-electron Kohn-Sham Hamiltonian. Hence, the solution of Eq. (2.34) is an antisymmetrized product (Slater determinant) of the lowest-energy Kohn-Sham orbitals $\theta_i^{KS}(\boldsymbol{r}_i)$ of the reference system. The anti-symmetrization is necessary to fulfill the Pauli principle for fermions. The orbitals $\theta_i^{KS}(\boldsymbol{r}_i)$ are eigenfunctions of the Kohn-Sham Hamiltonian h_i^{KS}.

$$\Psi_s = |\theta_1^{KS} \cdots \theta_n^{KS}| \tag{2.36}$$

$$h_i^{KS}\theta_i^{KS} = \varepsilon_i^{KS}\theta_i^{KS} \tag{2.37}$$

The ε_i^{KS} are effective one-electron energies. The Kohn-Sham orbitals have no

physical significance other than in allowing the exact molecular ground-state density $\rho(\boldsymbol{r})$ to be calculated. Furthermore, the energies ε_i^{KS} cannot be compared to the orbital energies of the real system. Still, it turns out, that the highest ε_i^{KS} can be proved to be equal to minus the molecular ionization energy [8].

Follwing the work of Kohn and Sham, two new quantities are defined:

$$\Delta T[\rho] \equiv T[\rho] - T_s[\rho] \tag{2.38}$$

$$\Delta V_{ee}[\rho] \equiv V_{ee}[\rho] - \frac{1}{2}\int\int \frac{\rho(\boldsymbol{r}_1)\rho(\boldsymbol{r}_2)}{r_{12}}\, d\boldsymbol{r}_1 d\boldsymbol{r}_2 \ , \tag{2.39}$$

where r_{12} is the distance between $\boldsymbol{r}_1$ and $\boldsymbol{r}_2$. $\Delta T[\rho]$ is the difference between the kinetic energy of the real and the fictitious system, $\Delta V_{ee}[\rho]$ is the difference between the electrostatic energy of the quantum mechanical system and the energy that a classical charge distribution $\rho(\boldsymbol{r})$ exhibits. Using these definitions, Eq. (2.28) reads:

$$E_v[\rho] = \int \rho(\boldsymbol{r})v(\boldsymbol{r}) + T_s[\rho] + \frac{1}{2}\int\int \frac{\rho(\boldsymbol{r}_1)\rho(\boldsymbol{r}_2)}{r_{12}}\, d\boldsymbol{r}_1 d\boldsymbol{r}_2 + \Delta T[\rho] + \Delta V_{ee}[\rho] \ . \tag{2.40}$$

The exact functional form of $\Delta T[\rho]$ and $\Delta V_{ee}[\rho]$ is unknown, as the energies $T[\rho]$ and $V_{ee}[\rho]$ before. Defining the *exchange-correlation energy functional* $E_{xc}[\rho]$ by

$$E_{xc}[\rho] \equiv \Delta T[\rho] + \Delta V_{ee}[\rho] \ , \tag{2.41}$$

the energy functional can be written as

$$E_v[\rho] = \int \rho(\boldsymbol{r})v(\boldsymbol{r}) + T_s[\rho] + \frac{1}{2}\int\int \frac{\rho(\boldsymbol{r}_1)\rho(\boldsymbol{r}_2)}{r_{12}}\, d\boldsymbol{r}_1 d\boldsymbol{r}_2 + E_{xc}[\rho] \ . \tag{2.42}$$

The motivation for the previous definitions is to express $E_v[\rho]$ in terms of three quantities, the first three terms on the right side of Eq. (2.42), that are easy to evalute from ρ and that include the main contributions to the ground-state energy, plus a fourth quantity $E_{xc}[\rho]$, which, although not easy to compute accurately, will be a relatively small term. The key to an accurate KS DFT calculation of molecular properties is to get a good approximation to $E_{xc}[\rho]$.

So far, two important steps on the way to a successful DFT calculation are not

clear: Firstly, how to evaluate the first three terms of Eq. (2.42) given the density and secondly, how to find the ground-state density itself. The answer to the first problem can be found by assuming, that the Kohn-Sham orbitals are known and calculating the electron density, which is the same for the reference and the real system:

$$\rho = \rho_s = \sum_{i=1}^{n} |\theta_i^{KS}|^2 \ . \tag{2.43}$$

Now the integrations in Eq. (2.42) can easily be carried out. The kinetic term is given by

$$T_s[\rho] = -\frac{1}{2}\langle\Psi_s|\sum_{i=1}^{n}\nabla_i^2|\Psi_s\rangle \ . \tag{2.44}$$

Using the *Condon-Slater rules* for one-particle operators (see [2, p. 341]), the Slater determinant collapses to a sum over the orbitals, if the orbitals are orthonormal:

$$T_s[\rho] = -\frac{1}{2}\sum_{i=1}^{n}\langle\theta_i^{KS}(1)|\nabla_1^2|\theta_i^{KS}(1)\rangle \ . \tag{2.45}$$

Thus, the total energy can be obtained from the above formulas, if the exchange-correlation function is determined.

Still, it is not clear how to obtain the Kohn-Sham orbitals. Therefore, the Variational Principle for the ground-state density (see Sec. 2.1.3) is needed. The desired density minimizes the energy functional, i.e. the first variation of Eq. (2.42) with respect to the density, or the Kohn-Sham orbitals, vanishes:

$$\delta E_v[\{\theta_i^{KS}\}] = 0 \ . \tag{2.46}$$

For writing the kinetic energy as given in Eq. (2.45) the Kohn-Sham orbitals have to be orthonormal. This is achieved by introducing the additional condition

$$\int \theta_i^{KS*}(\boldsymbol{r})\theta_j^{KS}(\boldsymbol{r})\ d\boldsymbol{r} = \delta_{ij} \ . \tag{2.47}$$

Thus, the following functional has to be minimized:

$$\Omega[\{\theta_i^{KS}\}] = E_v[\{\theta_i^{KS}\}] - \sum_{i=1}^{n}\sum_{j=1}^{n}\varepsilon_{ij}\int \theta_i^{KS*}(\boldsymbol{r})\theta_j^{KS}(\boldsymbol{r})\ d\boldsymbol{r} \ , \tag{2.48}$$

where ε_{ij} are Lagrangian multipliers. The condition of stationarity applied to Eq. (2.48),

$$\delta\Omega[\{\theta_i^{KS}\}] = 0 \ , \tag{2.49}$$

leads to the n equations

$$\begin{aligned}\left[-\frac{1}{2}\nabla_1^2 + v(\boldsymbol{r}_1) + \int \frac{\rho(\boldsymbol{r}_2)}{r_{12}}\, d\boldsymbol{r}_2 + v_{xc}(\boldsymbol{r}_1)\right]\theta_i^{KS}(\boldsymbol{r}_1) &= \varepsilon_i^{KS}\theta_i^{KS}(\boldsymbol{r}_1) \\ h_1^{KS}\theta_i^{KS}(\boldsymbol{r}_1) &= \varepsilon_i^{KS}\theta_i^{KS}(\boldsymbol{r}_1) \ ,\end{aligned} \tag{2.50}$$

where the potential $v_{xc}(\boldsymbol{r})$ is defined via the functional derivative

$$v_{xc}(\boldsymbol{r}) \equiv \frac{\delta E_{xc}[\rho(\boldsymbol{r})]}{\delta\rho(\boldsymbol{r})} \ . \tag{2.51}$$

$h^{KS}(1)$ is the one-electron operator from Eq. (2.35). These equations are usually referred to as *Kohn-Sham equations*, a detailed derivation can be found in [6]. Since the potentials in Eq. (2.50) depend on the density, these equations have to be solved in a self-consistent manner.

The Kohn-Sham equations also show that this method is only a compromise between practical applicability and the original aims of DFT. The fundamental quantity is not the density, but rather the Kohn-Sham orbitals, which is necessary for evaluating the kinetic energy functional. So far, no formula for the kinetic energy which only depends on the density and yields sufficiently accurate results could be found.

The exchange-correlation energy $E_{xc}[\rho]$ contains the following components: the *kinetic correlation energy*, i.e. the difference in the kinetic energy for the real molecule and the fictitious reference system, the *exchange energy*, which arises from the antisymmetry requirement for the wave function, the *Coulombic correlation energy*, which is associated with interelectronic repulsions and a *self-interaction correction* (SIC). The SIC arises from the fact that the classical charge-cloud electrostatic-repulsion expression in Eq. (2.39) erroneously allows an electron to interact with the charge distribution created by itself. The SIC compensates for this error.

At first glance, the Kohn-Sham method seems not to simplify the problem, since there are n equations that have to be solved, now. But these equations are only n one-particle problems, which are much easier to treat than one n-particle problem. The only drawback is the missing exchange-correlation functional. If we knew its exact form, DFT would yield *exact* solutions of the Schrödinger equation. Unfortunately, this is not the case, so adequate approximations for $E_{xc}[\rho]$ have to be found.

2.1.5 The Local-Density Approximation

As seen in the previous section, the equations of Kohn and Sham contain the exchange-correlation functional. Therefore, a practical calculation requires an explicit form of this term. The simplest approximation, actually introduced by Kohn and Sham in 1965, is the *Local-Density Approximation* (LDA). Although it is based on very basic assumptions, it yields accurate results for many systems.

Hohenberg and Kohn showed, that $E_{xc}[\rho]$ can be approximated by

$$E_{xc}^{LDA}[\rho] = \int \rho(\boldsymbol{r})\epsilon_{xc}(\rho)\ d\boldsymbol{r} \tag{2.52}$$

if the density varies extremely slowly with position. $\epsilon_{xc}(\rho)$ is the exchange plus correlation energy per electron in a homogeneous electron gas with electron density ρ. Taking the functional derivative of Eq. (2.52) with respect to $\rho(\boldsymbol{r})$, one finds the potential:

$$v_{xc}^{LDA}(\boldsymbol{r}) = \frac{\delta E_{xc}^{LDA}[\rho(\boldsymbol{r})]}{\delta\rho(\boldsymbol{r})} = \epsilon_{xc}(\rho(\boldsymbol{r})) + \rho(\boldsymbol{r})\frac{\delta\epsilon_{xc}(\rho(\boldsymbol{r}))}{\delta\rho(\boldsymbol{r})}\ . \tag{2.53}$$

The self-consistent solution of the Kohn-Sham equations Eq. (2.50) using the potential from Eq. (2.53) is the LDA.

One can show that $\epsilon_{xc}(\rho)$ can be written as the sum of exchange and correlation parts:

$$\epsilon_{xc}(\rho) = \epsilon_x(\rho) + \epsilon_c(\rho)\ . \tag{2.54}$$

The first term is the exchange energy, the second the correlation energy per electron in a homogeneous electron gas. Furthermore, an analytical expression for

Atom	LDA	Hartree-Fock	Experiment
He	-2.83	-2.86	-2.90
Li	-7.33	-7.43	-7.48
Ne	-128.12	-128.55	-128.94
Ar	-525.85	-526.82	-527.60

Table 2.1: Total energies in atomic units, comparison of various methods to experimental data [6, p.156].

$\epsilon_x(\rho)$ can be given:

$$\epsilon_x(\rho) = -\frac{3}{4}\left(\frac{3}{\pi}\right)^{\frac{1}{3}} \rho^{\frac{1}{3}} \ . \tag{2.55}$$

A complete dervation of this result can be found in [6]. Ceperley and Alder obtained precise values for $\epsilon_c(\rho)$ from a Monte-Carlo simulation [9], which then have been parameterized by Vosko et al. [10]. This analytical formula can be used in Eq. (2.54).

According to Eq. (2.52), the LDA method applies the results for a homogeneous electron gas to infinitesimal regions of the inhomogeneous system with the density $\rho(\boldsymbol{r})$. Each of these regions contains $\rho(\boldsymbol{r})d\boldsymbol{r}$ electrons, that cause a contribution to the energy of $\epsilon_{xc}(\rho(\boldsymbol{r}))\rho(\boldsymbol{r})d\boldsymbol{r}$. These contributions are subsequently integrated over the whole space. The first application of this procedure has been done by Sham and Tong in 1966 [11]. They calculated the total energy for various atoms and compared the results from different methods to experimental data. A summary of their findings can be found in Table 2.1. LDA can be used with reasonable accuracy for systems with only slowly varying density with respect to position. It turns out, that this approximation is very successful in many atomic and molecular systems. In cases where hydrogen bonds are present, LDA results are less accurate. Therefore, many different reformulations of the exchange-correlation functional have been developed to correct for these deficiencies and will be presented in the next section.

2.1.6 Gradient Corrected functionals

As presented, the LDA is based on a homogeneous electron gas which gives accurate results for systems which exhibit slowly varying electron densities. Function-

als that go beyond this approximation aim to correct the LDA for the variation of the electron density with position by including the gradients of ρ:

$$E_{xc}^{GGA}[\rho] = \int e_{xc}(\rho(\boldsymbol{r}), \nabla\rho(\boldsymbol{r}))\ d\boldsymbol{r}\ . \tag{2.56}$$

Such functionals are called *Generalized Gradient Approximation* (GGA) functionals. Again, the functional $E_{xc}^{GGA}[\rho]$ is a sum of two parts:

$$E_{xc}^{GGA}[\rho] = E_{x}^{GGA}[\rho] + E_{c}^{GGA}[\rho]\ . \tag{2.57}$$

Over the past years, a variety of GGA functionals has been developed, based on theoretical considerations such as the known behavior of the true (but unknown) functionals E_x and E_c in various limiting situations as a guide, with some empiricism thrown in. Special attention has been given to capturing a more accurate description of hydrogen bonded systems. A commonly used functional for the exchange is Becke's 1988 functional, denoted B88, Bx88, Becke88 or B [12]:

$$E_{x}^{B88}[\rho] = E_{x}^{LDA}[\rho] - b\int \frac{\rho^{\frac{4}{3}}\chi^2}{1 + 6b\chi\sinh^{-1}\chi}\ d\boldsymbol{r}\ , \tag{2.58}$$

where $\chi \equiv |\nabla\rho|/\rho^{\frac{4}{3}}$ and b is an empirical parameter whose value 0.0042 atomic units was determined by fitting known Hartree-Fock exchange energies of several atoms. This functional for the exchange energy can now be added to another functional for the correlation energy, according to Eq. (2.57). An example of widespread use is the Lee-Yang-Parr (LYP) functional [13]. This combination, denoted BLYP, is in many cases an improvement to the LDA approximation and will be used mostly in this work. Besides that, there are many different exchange correlation functionals. Commonly used is also B3LYP (or Becke3LYP), a *Hybrid functional*. Effects of correlation can be partially reproduced by PW91 (Perdew-Yang 1991), a parameter-free functional as PBE, the functional of Perdew, Burke and Ernzerhof. The most recent development are the *meta-GGA functionals*, which not only depend on the density $\rho(\boldsymbol{r})$, but also on the *kinetic energy density*[3] $\tau(\boldsymbol{r})$, a sum over all occupied Kohn-Sham orbitals [14].

[3] which is defined as $\tau(\boldsymbol{r}) = \sum_i^{occup} \frac{1}{2}|\nabla\theta_i^{KS}(\boldsymbol{r})|^2$

2.2 Pseudopotentials and Basis Sets

2.2.1 The Pseudopotential Approximation

The computational expense of a quantum chemical calculation increases rapidly with the number of electrons and the size of the basis set used (see Sec. 2.2.2). Since different orbitals have to be orthogonal with respect to each other, they exhibit large oscillations in the core region of an atom. An exact representation of this behavior would require a huge basis set, leading to a very unfavorable computational effort. There are various approaches to this problem, as *Generalized Plane Waves* [15] or the *Gaussian and augmented plane waves* (GAPW) method (see Sec. 2.3.2). A commonly used solution is to employ *Pseudopotentials*, which will be introduced here.

The strong oscillations of the wave functions in the vicinity of the core are caused by the $1/r$ divergence of the potential. This potential is screened by the electrons in the inner shells. Since these electrons hardly contribute to chemical bonds, they can be included into the core potential, yielding a much smoother effective potential. This is the fundamental idea of pseudopotentials. The treatment of the core electrons as "spectators" of the chemical activity of the valence electrons is known as *frozen core* approximation. A new potential, which is smooth in the core region, is thus generated such as to reproduce the original valence wave functions accurately outside of a given radius r_c. The core electrons themselves are completely absorbed by the pseudopotential and do not contribute to the calculation anymore. The remaining task is to find a pseudopotential that is as smooth as possible, which also makes the wave functions of the valence electrons smooth in the core region, but does not change them for $r > r_c$.

The quality of a pseudopotential is characterized by two factors. First, a pseudopotential should have good transferability, i.e. the potential should reproduce the valence wave function for various different chemical environments. Once generated, the potential should be applicable to many systems with the same parameters. Second, the pseudopotential should be smooth which allows for the use of small basis sets and improves the overall computational efficiency. So, the development of new pseudopotentials always looks for the best compromise between these two requirements.

It turned out, that *norm-conserving* pseudopotentials yield good results [16]. This means, that valence wave functions from a pseudopotential calculation should include the same integrated charge in the core region as their all-electron counterparts. In other words, the physical system should not "see" any difference between the original and the "pseudo" atom for $r > r_c$. Such a pseudopotential in general has the following *non-local* form for an atom, which is situated in the origin of the coordinate system [17]:

$$V^{PP}(\boldsymbol{r},\boldsymbol{r'}) = V^{loc}(\boldsymbol{r})\ \delta(\boldsymbol{r}-\boldsymbol{r'}) + \sum_{l=0}^{l_{max}} \sum_{m=-l}^{m=l} Y_{lm}^{*}(\theta,\phi) V_l^{nl}(r) \frac{\delta(r-r')}{r^2} Y_{lm}(\theta',\phi')\ , \tag{2.59}$$

where $V^{lok}(\boldsymbol{r})$ is the local part of the potential and $V_l^{nl}(r)$ the non-local one, which depends on both the norm $r = |\boldsymbol{r}|$ angular momentum l. The spherical harmonics act as a projector that isolates the contribution to the wave function that belongs to l and m. So, the effect of the pseudopotential depends on the actual state of the particle.

Similarly as for the exchange-correlation functionals, there exist many different parameterizations of the local and non-local parts of Eq. (2.59). In this work, the pseudopotentials developed by Gödecker are employed [18]. The local part is given by:

$$\begin{aligned} V^{loc}(r) \ &= \ \frac{-Z_{ion}}{r}\ \mathrm{erf}\left(\frac{r}{\sqrt{2}r_{loc}}\right) + \exp\left[-\frac{1}{2}\left(\frac{r}{r_{loc}}\right)^2\right] \\ &\quad \times \left[C_1 + C_2\left(\frac{r}{r_{loc}}\right)^2 + C_3\left(\frac{r}{r_{loc}}\right)^4 + C_4\left(\frac{r}{r_{loc}}\right)^6\right]\ . \end{aligned} \tag{2.60}$$

Z_{ion} is the ionic charge of the core, i.e. the nuclear charge minus the charge of the core electrons, erf is the error function and r_{loc} the range of the potential. The constante $C_1, \ldots, C_4$ are determined with the help of all-electron reference calculations [19]. The usage of these pseudopotentials significantly reduces the size of the basis set, that has to be employed. In turn, the pseudo-wave functions do not resemble the all-electron functions in the core region anymore. However, this does not cause large effects on forces, geometries or other properties that mostly depend on the valence electrons. Unfortunately, spectroscopic properties such

as NMR chemical shifts or nuclear quadrupole couplings exhibit a dependence on the core electrons and can thus not be calculated with a good accuracy in the pseudopotential approximation. A possible solution to this is the above-mentioned GAPW method, that will be introduced in Sec. 2.3.2.

2.2.2 Basis sets

In general, the molecular wave functions, determined as described in Sec. 2.1.4, are expanded in functions, given by the used basis set. In this work, two different kinds of basis sets will be employed. On the one hand, there are *localized basis sets*. These are derived from atomic wave functions and are thus centered at the respective atom. Commonly used functions are gaussians or exponentials in combination with spherical harmonics. Such basis sets are typically used in the "traditional" quantum chemical programs, since they are a good choice for isolated molecules and the interpretation of the results is straightforward. On the other hand, there are *plane waves*. This possibility originally was used in solid state physics. There, the periodicity of crystals plays a crucial role and thus plane waves seem to be an appropriate choice, since they naturally obey periodic boundary conditions. In contrary to the localized basis sets mentioned before, plane waves are delocalized, i.e. they can not be assigned to a specific atom. Thus, the chemical interpretation of the results is somewhat more involved.

Localized basis sets

A commonly used choice for localized basis sets, especially in the first years of quantum chemical calculations, are *Slater-type orbitals* (STOs). Their main ingredient are exponential functions, since these are the correct atomic wave functions. An STO centered on an atom a has the form

$$\chi(r_a, \theta_a, \phi_a) = N r_a^{n-1} e^{-\zeta r_a} Y_l^m(\theta_a, \phi_a) \ , \tag{2.61}$$

where Y_l^m is a spherical harmonic and N is a normalization constant. Each molecular orbital (MO) is now described by a linear combination of different basis functions χ.

It turned out, that STOs, although a physically motivated choice, are not favorable for practical calculations. For this purpose, Boys proposed in 1950 the use of *Gaussian-type functions* (GTFs) instead of the STOs. A *Cartesian Gaussian* centered on atom b is defined as

$$g_{ijk} = N x_b^i y_b^j z_b^k e^{-\alpha r_b^2} \ , \tag{2.62}$$

where i, j, k are nonnegative integers, α is a positive orbital exponent and x_b, y_b, z_b are Cartesian coordinates with the origin at nucleus b. N, again, is a normalization constant. When $i + j + k = 0$, the GTF is called an *s-type* Gaussian; when $i + j + k = 1$, it is a *p-type* Gaussian and so on. To accurately describe an atomic orbital, a linear combination of several GTFs has to be used, leading to many more terms in a GTF-based calculation than in one that employs STOs. But still, since integrals over basis functions are the most demanding task in such a computation and integrals over GTFs can be solved much faster than those over STOs, GTFs are the preferred basis functions.

Instead of using individual Gaussians as basis functions, each basis function is usually taken as a linear combination of a few Gaussian, according to

$$\chi_r = \sum_u d_{ur} g_u \ , \tag{2.63}$$

where the g_u's are normalized Cartesian Gaussian, as in Eq. (2.62), centered on the same atom and having the same i, j, k values, but different α's. The *contraction coefficients* d_{ur} are constants that are held fixed during the calculation. χ_r is called *contracted Gaussian-type function* (CGTF) and the g_u's are called *primitive Gaussians*. The terminology for Gaussian basis sets is manifold and often there are even different names for the same set of basis functions. A good introduction to this can be found in [2]. It should be mentioned, that often additional functions with a higher angular momentum (given by i, j, k) than necessary for the actual electronic configuration are added, referred to as *polarization functions*. A second class of special functions are those with exceptionally small orbital coefficients (typically 0.01 to 0.1), which are called *diffuse* functions.

Plane waves

Quantum chemical codes that employ plane waves as a basis, i.e. CPMD [20] or CP2K [21], usually impose periodic boundary conditions and use basis functions of the form

$$f_{\boldsymbol{G}}(\boldsymbol{r}) = N \exp\left[i\boldsymbol{G}\boldsymbol{r}\right] . \tag{2.64}$$

The normalization N is given by $N = 1/\sqrt{\Omega}$, where Ω is the volume of the unit cell. The vectors $\boldsymbol{G}$ are the reciprocal lattice vectors, thus also given by the periodicity of the crystal. Plane waves are not localized, i.e. they do not depend parametrically on a point in space. Therefore, they can be considered an ultimately "balanced basis set" in the language of quantum chemistry. Furthermore, this means that they do not give rise to any Pulay forces [15].

Any function the is periodic in space can be expanded in plane waves,

$$\Psi(\boldsymbol{r}) = \Psi(\boldsymbol{r}+\boldsymbol{L}) = \frac{1}{\sqrt{\Omega}} \sum_{\boldsymbol{G}} \Psi(\boldsymbol{G}) \exp\left[i\boldsymbol{G}\boldsymbol{r}\right] . \tag{2.65}$$

The vector $\boldsymbol{L}$ is an arbitrary linear combination of the lattice vectors. According to *Bloch's theorem* each solution of a Schrödinger equation with periodic potential can be written as product of a plane wave envelope function and a second function (*Bloch function*), that also is periodic on the lattice:

$$\begin{aligned} \phi_{i\boldsymbol{k}}(\boldsymbol{r}) &= \exp\left[i\boldsymbol{k}\boldsymbol{r}\right]\, u_i(\boldsymbol{r},\boldsymbol{k}) \\ u_i(\boldsymbol{r},\boldsymbol{k}) &= u_i(\boldsymbol{r}+\boldsymbol{L},\boldsymbol{k}) . \end{aligned} \tag{2.66}$$

$\boldsymbol{k}$ is a vector from the first Brillouin zone and i is the band index [22]. This theorem can be applied to the Kohn-Sham orbitals, since the Kohn-Sham potential from Eq. (2.35) satisfies the required periodicity:

$$\theta_i^{KS}(\boldsymbol{r},\boldsymbol{k}) = \exp[i\boldsymbol{k}\boldsymbol{r}] u_i(\boldsymbol{r},\boldsymbol{k}) . \tag{2.67}$$

The periodic function $u_i(\boldsymbol{r},\boldsymbol{k})$ can be expanded in the plane wave basis:

$$u_i(\boldsymbol{r},\boldsymbol{k}) = \frac{1}{\sqrt{\Omega}} \sum_{\boldsymbol{G}} c_i(\boldsymbol{G},\boldsymbol{k}) \exp[i\boldsymbol{G}\boldsymbol{r}] . \tag{2.68}$$

Substitution into Eq. (2.67) yields:

$$\theta_i^{KS}(\boldsymbol{r},\boldsymbol{k}) = \frac{1}{\sqrt{\Omega}} \sum_{\boldsymbol{G}} c_i(\boldsymbol{G},\boldsymbol{k}) \exp[i(\boldsymbol{G}+\boldsymbol{k})\boldsymbol{r}] \ . \tag{2.69}$$

The summation over all reciprocal lattice vectors cannot be done in a practical calculation and therefore a terminating condition has to be introduced. This condition is coupled to the kinetic energy given by the respective orbital. This energy can easily be calulated:

$$\begin{aligned} T_i &= -\frac{1}{2}\langle\theta_i^{KS}|\nabla^2|\theta_i^{KS}\rangle \\ &= \frac{1}{2\Omega} \sum_{\boldsymbol{G}} |\boldsymbol{k}+\boldsymbol{G}|^2 \ |c_i(\boldsymbol{G},\boldsymbol{k})|^2 \ . \end{aligned} \tag{2.70}$$

Since the coefficients $c_i(\boldsymbol{G},\boldsymbol{k})$ are small for large values of $\boldsymbol{G}$, a cutoff energy is set, that only allows vectors $\boldsymbol{G}$ with

$$\frac{1}{2}|\boldsymbol{k}+\boldsymbol{G}|^2 \ \leq \ E_c \ . \tag{2.71}$$

In large and non-metallic systems the usage of only one special value for $\boldsymbol{k}$ is sufficient. This vector is called the Γ-point, with $\boldsymbol{k} = 0$. In this work, this approximation will always be used, since the systems investigated do not require a treatment beyond that.

2.3 Computational Realizations

2.3.1 Gaussian and Plane Waves Method (GPW)

So far, only the general framework of DFT and some concepts such as pseudopotentials and basis sets have been introduced. In this section, an efficient and accurate method for performing DFT calculations is presented, namely the *Gaussian and plane waves* (GPW) method. Although there are other ways of conducting a DFT calculation, e.g. using only plane waves or Gaussians as basis, the somewhat advanced hybrid GPW method will be explained here, because a part of this work was the implementation of the stress tensor into the CP2K [21] code (see Chapter 7), which employs GPW. Additionally, GPW opens the way for all-electron calculations in a periodic description, which will be described in the next section.

Many quantum chemical programs, that use periodic boundary conditions, make use of plane waves (PW) for the expansion of the Kohn-Sham orbitals (see Sec. 2.1.4). A famous example is CPMD [20], which has also been used for this work. PW as a basis set for quantum chemical calculations are a rather unnatural choice, although they have a couple of advantages compared to the standard Gaussian basis sets. PW are atomic position independent and therefore they do not give rise to Pulay forces. The calculation of the Hartree potential is easy and checking the convergence with respect to the basis set size is trivial (see Sec. 2.2.2). Last, but not least, the use of the fast Fourier transform technique considerably simplifies many algebraic manipulations and allows for almost linear scaling with the system size. But there are also some disadvantages. Most noticeably, a large number of PW is needed to reproduce wave functions close to the nuclei, even with the use of pseudopotentials. Even more disturbing is the fact, that all space is filled with the same number of basis functions, i.e. empty space, where no electron density is presented, is described in the same way as atom-filled regions. PW also complicate the interpretation of the results, since they have to be projected on localized basis sets before the relevant chemistry can be extracted.

The use of Gaussians, in turn, leads to very unfavorable scaling with the system size due to the Hartree term. Additionally, they give rise to Pulay forces and basis set superposition errors (BSSE). A periodic description, as desired in solid state

calculations, is not natural for such a basis set. Thus, the GPW method tries to combine the usage of both basis sets [23]. The aim, of course, is to remove the main defects of the individual methods, while preserving most of the advantages. For example, the bottleneck of calculations using Gaussians, the Hartree term, can be removed by solving the Poisson equation with plane waves, leading then to a linear scaling. This work follows closely the descriptions given in [24].

The central idea of GPW is the representation of the density in two different basis sets. These are, as mentioned above, Gaussian functions and plane waves. Thus, the density ρ is given by

$$\rho(\boldsymbol{r}) = \sum_{\mu,\nu} P^{\mu\nu} \phi_\mu(\boldsymbol{r}) \phi_\nu(\boldsymbol{r}) \ , \tag{2.72}$$

where $P^{\mu\nu}$ is a density matrix element, or by plane waves

$$\tilde{\rho}(\boldsymbol{r}) = \frac{1}{\Omega} \sum_{\boldsymbol{G}} \tilde{n}(\boldsymbol{G}) \exp\left(i\boldsymbol{G} \cdot \boldsymbol{r}\right) \ , \tag{2.73}$$

where Ω is the volume of the unit cell and $\boldsymbol{G}$ are the reciprocal lattice vectors. The expansion coefficients are such that $\tilde{\rho}(\boldsymbol{r})$ is equal to $\rho(\boldsymbol{r})$. Using this dual representation, the Kohn-Sham DFT energy expression is defined as

$$\begin{aligned} E[\rho] &= E_T[\rho] + E_V[\rho] + E_H[\rho] + E_{xc}[\rho] + E_{II} \\ &= \sum_{\mu,\nu} P^{\mu\nu} \langle \phi_\mu(\boldsymbol{r}) | -\frac{1}{2}\nabla^2 | \phi_\nu(\boldsymbol{r}) \rangle \\ &\quad + \sum_{\mu,\nu} P^{\mu\nu} \langle \phi_\mu(\boldsymbol{r}) | V_{loc}^{PP}(r) | \phi_\nu(\boldsymbol{r}) \rangle \\ &\quad + \sum_{\mu,\nu} P^{\mu\nu} \langle \phi_\mu(\boldsymbol{r}) | V_{nl}^{PP}(\boldsymbol{r}, \boldsymbol{r}') | \phi_\nu(\boldsymbol{r}') \rangle \\ &\quad + 2\pi\Omega \sum_{\boldsymbol{G}} \frac{\tilde{\rho}^*(\boldsymbol{G}) \tilde{\rho}(\boldsymbol{G})}{\boldsymbol{G}^2} + \int e_{xc}(\boldsymbol{r}) d\boldsymbol{r} \\ &\quad + \frac{1}{2} \sum_{I \neq J} \frac{Z_I Z_J}{|\boldsymbol{R}_I - \boldsymbol{R}_J|} \ , \end{aligned} \tag{2.74}$$

where $E_T[\rho]$ is the electronic kinetic energy, $E_V[\rho]$ is the electronic interaction with the ionic cores, $E_H[\rho]$ is the electronic Hartree energy, $E_{xc}[\rho]$ is the exchange-

correlation energy and E_{II} is the interaction energy of the ionic cores with charges Z_A and positions $\boldsymbol{R}_A$. This formula can be compared directly to Eq. (2.42), only here, the interaction energy of the ionic cores has been added. Furthermore, the external potential $v(\boldsymbol{r})$ has been written as sum of the local and non-local contributions of the pseudopotential (see Sec. 2.2.1). The sum over the Kohn-Sham orbitals is now replaced by the summation over all primitive Gaussians, i.e. the basis functions. In Eq. (2.74) the major advantage of the GPW method can be seen. The Hartree energy is now given in the reciprocal space. The Hartree potential, which is non-trivial to obtain in real space, can be found as

$$v_H(\boldsymbol{G}) = \frac{4\pi\tilde{\rho}_{tot}(\boldsymbol{G})}{\boldsymbol{G}^2} \ , \tag{2.75}$$

where the total charge distribution $\tilde{\rho}_{tot}(\boldsymbol{G}) = \tilde{\rho}(\boldsymbol{G}) + \tilde{\rho}_c(\boldsymbol{G})$ with the nuclear charge density $\tilde{\rho}_c(\boldsymbol{G})$ has been used. The real-space potential is then obtained by a simple Fourier transformation.

The treatment of the Hartree term with plane waves naturally includes the periodic boundary conditions. The remaining terms, which use the Gaussian basis set, do not obey this requirement. Therefore, the Cartesian Gaussians $\phi_\mu(\boldsymbol{r})$ have to be turned into periodic functions. This is accomplished by extending $\phi_\mu(\boldsymbol{r})$ over all its periodic images:

$$\phi_\mu^P(\boldsymbol{r}) = \sum_{\boldsymbol{i}} \phi_\mu(\boldsymbol{r} - \boldsymbol{l_i}) \ , \tag{2.76}$$

where the sum is over all triplets of positive and negative integers $\boldsymbol{i} = i, j, k$, $\boldsymbol{l_i} = i\boldsymbol{l}_1 + j\boldsymbol{l}_2 + k\boldsymbol{l}_3$. $\boldsymbol{l}_1$, $\boldsymbol{l}_2$ and $\boldsymbol{l}_3$ are the three lattice vectors. Of course, this summation has to be truncated at some point. This is usually done by a distance criterion, i.e. the image is only taken into account, if the product of the two gaussians is non-negligible to within some threshold, typically 10^{-10} to 10^{-14}.

In conclusion, GPW treats all terms but the Hartree energy in the Gaussian basis. These parts are all calculated analytically, since they only involve integrals over Gaussian functions and products of Gaussians. A product of two Gaussians is again a Gaussian, so these terms can be computed easily in real space. Only the Hartree term, which is difficult to evaluate in real space is obtained in the recipro-

cal space, which saves computational time and leads to a better scaling behavior. Furthermore, this method can be extended to the *Gaussian and Augmented Plane Waves* (GAPW) method, which is introduced in the next section.

2.3.2 Gaussian and Augmented Plane Waves Method (GAPW)

The GPW method was invented for combining the benefits from both Gaussians and plane waves as basis set. But still, pseudopotentials have been used. Although these potentials give very accurate results in many cases, there are situations, where such an approximation is not favorable. When spectroscopic properties as Nuclear Quadrupole Coupling Constants (NQCC) or NMR chemical shifts are calculated, the absence of the core electrons can be disturbing (see also Chapter 3). In these cases, the full all-electron potential of the ionic cores has to be used. Since in GPW the whole electron density is expanded in plane waves for the computation of the Hartree term, a very high cutoff (see Sec. 2.2.2) would be necessary for the Gaussians with a large orbital exponent. Therefore, all-electron calculations are usually not carried out in GPW, or a pure plane wave environment. Lippert et al. have presented an extension of the GPW method, the *Gaussian and Augmented Plane Waves* (GAPW) method [25]. While it has originally been proposed for accelerating the GPW method by separating the very hard Gaussians from the smooth ones, it can also be used for all-electron calculations [26]. Here, only the basic ideas of the method will be presented, details can be found in the cited literature.

The fundamental idea of GAPW is the separation of the electron density into three contributions:

$$\rho = \tilde{\rho} - \tilde{\rho}^1 + \rho^1 \ , \tag{2.77}$$

where $\tilde{\rho}$ is smooth and distributed over all space, and

$$\rho^1 = \sum_A \rho_A^1 \qquad \text{and} \qquad \tilde{\rho}^1 = \sum_A \tilde{\rho}_A^1 \tag{2.78}$$

are sums of atom-centered contributions ρ_A^1 and $\tilde{\rho}_A^1$ which are hard and soft, respectively. The densities ρ_A^1 and $\tilde{\rho}_A^1$ are constructed such as to cancel each other outside a spherical atomic region U_A. The regions U_A of different atoms do not

overlap. Inside U_A the soft density $\tilde{\rho}$ is equal to its atom-centered contribution $\tilde{\rho}^1$

$$\tilde{\rho}(\boldsymbol{r}) = \tilde{\rho}^1(\boldsymbol{r}) \qquad \text{for} \qquad \boldsymbol{r} \in \mathrm{U}_A \tag{2.79}$$

and outside the atomic region, in the interstitial region I, $\tilde{\rho}$ is equal to the total density ρ

$$\tilde{\rho}(\boldsymbol{r}) = \rho(\boldsymbol{r}) \qquad \text{for} \qquad \boldsymbol{r} \in \mathrm{I}\ . \tag{2.80}$$

These requirements lead to the following equations, that have to be fulfilled:

$$\begin{aligned}
\rho(\boldsymbol{r}) - \tilde{\rho}(\boldsymbol{r}) &= 0 \qquad \text{for} \qquad \boldsymbol{r} \in \mathrm{I}\ , \\
\rho_A^1(\boldsymbol{r}) - \tilde{\rho}_A^1(\boldsymbol{r}) &= 0 \qquad \text{for} \qquad \boldsymbol{r} \in \mathrm{I}\ , \\
\tilde{\rho}(\boldsymbol{r}) - \tilde{\rho}_A^1(\boldsymbol{r}) &= 0 \qquad \text{for} \qquad \boldsymbol{r} \in \mathrm{U}_A\ , \\
\rho(\boldsymbol{r}) - \rho_A^1(\boldsymbol{r}) &= 0 \qquad \text{for} \qquad \boldsymbol{r} \in \mathrm{U}_A\ .
\end{aligned} \tag{2.81}$$

This way of partitioning the density leads to a separation of the contributions from the different densities to the total energy, i.e. for the exchange-correlation energy one finds:

$$E_{xc}[\rho] = E_{xc}[\tilde{\rho}] - \sum_A E_{xc}[\tilde{\rho}_A^1] + \sum_A E_{xc}[\rho_A^1]\ . \tag{2.82}$$

The treatment of the Hartree energy with the Ewald method [27] requires a somewhat more involved procedure, which will not be described here. Still, as in the GPW formulation, the computation of the Hartree energy can be separated into a global term that involves only smooth densities and local terms that involve short-ranged one-, two- and three center integrals. Therefore, the global part can be calculated in the PW representation using a PW basis of modest size, while the local parts can be evaluated analytically in the Gaussian representation. In an all-electron calculation, where the full potential of the ions is employed, the critical part of the potential is incorporated into the local part and the plane wave contribution is not affected by this.

Finally, the construction of the different densities has to be explained. As in GPW, the starting point is the density ρ, which is expanded in a set of contracted

Gaussian functions

$$\rho(\boldsymbol{r}) = \sum_{\mu,\nu} P^{\mu\nu} \phi_\mu(\boldsymbol{r}) \phi_\nu(\boldsymbol{r}) \ , \tag{2.83}$$

where

$$\phi_\mu(\boldsymbol{r}) = \sum_a C_{a\mu} g_a(\boldsymbol{r}) \ . \tag{2.84}$$

The g_a's are primitive Gaussian functions, the $C_{a\mu}$ are the respective contraction coefficients. The soft part of the electronic density can be expanded in smoothed Gaussians $\tilde{\phi}_\mu$

$$\tilde{\rho}(\boldsymbol{r}) = \sum_{\mu,\nu} P^{\mu\nu} \tilde{\phi}_\mu(\boldsymbol{r}) \tilde{\phi}_\nu(\boldsymbol{r}) \ , \tag{2.85}$$

which can be obtained from Eq. (2.83), if all primitive Gaussian functions g_a with an exponent larger than a certain threshold are removed. As before, the soft density can also be represented by plane waves

$$\tilde{\rho}(\boldsymbol{r}) = \frac{1}{\Omega} \sum_{\boldsymbol{G}} \tilde{n}(\boldsymbol{G}) \exp\left(i\boldsymbol{G} \cdot \boldsymbol{r}\right) \ , \tag{2.86}$$

with definitions as in Sec. 2.3.1. The remaining task is the construction of the one-center densities ρ^1 and $\tilde{\rho}^1$. This is achieved by using the primitive orbital functions of the current atom A. The contributions to the orbital ϕ_μ, that are centered on the atom A anyway, are trivial to treat, their coefficients are given by the appropriate $C_{a\mu}$. More difficult are the Gaussians that are centered on other atoms. Since the one-center density of atom A is only represented by Gaussians centered on A, the parts due to other atoms have to be projected on the basis functions belonging to A. Therefore, a new projector basis set $\{p_a\}$ is defined with a number of primitive Gaussian functions p_a equal to the number of Gaussians g_a. The projection is then performed by

$$\langle p_b | \phi_\mu \rangle = \sum_a C'_{a\mu} \langle p_b | g_a \rangle \ , \tag{2.87}$$

where the coefficients $C'_{a\mu}$ are defined by this equation. They can be obtained by

inverting the overlap matrix $\langle p_b|g_a\rangle$:

$$C'_{a\mu} = \sum_b \langle p|g\rangle^{-1}_{ab} \langle p_b|\phi_\mu\rangle \ . \tag{2.88}$$

As mentioned before, the coefficients $C'_{a\mu}$ for the case that the respective primitive Gaussian is already centered on A, are just given by Eq. (2.84). Thus, the one-center density can be written as

$$\rho^1_A = \sum_{ab\in A} \sum_{\mu\nu} C'_{a\mu} P^{\mu\nu} C'_{b\nu} g_a g_b \ . \tag{2.89}$$

The one-center expansion of the soft basis functions $\tilde{\rho}^1_A$ can be obtained easily from the previous equations. In principle, the same procedure could be applied to the soft basis, but there is actually no need for that. Since $\tilde{\rho}^1_A$ and ρ^1_A coincide in the interstitial region I, the coefficients obtained for the hard basis can also be used for the soft basis. Only the set of coefficients has to be restricted to the functions present in the soft basis:

$$\tilde{\rho}^1_A = \sum_{ab\in A} \sum_{\mu\nu} \tilde{C}'_{a\mu} P^{\mu\nu} \tilde{C}'_{b\nu} g_a g_b \ . \tag{2.90}$$

Now the individual contributions can be summed and the total GAPW density is found as

$$\begin{aligned} \rho &= \tilde{\rho} - \tilde{\rho}^1 + \rho^1 \\ &= \frac{1}{\Omega} \sum_{\boldsymbol{G}} \tilde{n}(\boldsymbol{G}) \exp\left(i\boldsymbol{G}\cdot\boldsymbol{r}\right) - \sum_{ab\in A} \sum_{\mu\nu} \tilde{C}'_{a\mu} P^{\mu\nu} \tilde{C}'_{b\nu} g_a g_b \\ &\quad + \sum_{ab\in A} \sum_{\mu\nu} C'_{a\mu} P^{\mu\nu} C'_{b\nu} g_a g_b \ . \end{aligned} \tag{2.91}$$

Making use of this separation of the density, all-electron DFT calculations can be carried out at modest computational expense. This enables the computation of spectroscopic properties under periodic boundary conditions, without any approximation introduced by pseudopotentials.

2.4 Molecular Dynamics Simulations

2.4.1 Overview

Molecular dynamics (MD) is well established as a powerful tool to investigate many-body condensed matter systems. A central point in molecular dynamics simulations is the question how to describe the interatomic interactions. The traditional route is to determine these in advance, leading to some kind of parameterized potential, which is then employed in the actual dynamics simulation. This approach is still in widespread use, especially for the investigation of biological systems, that contain a large number of atoms (typically $N > 1000$). With the advent of ab initio electronic structure calculations, following for example the route proposed by Kohn and Sham (see Sec. 2.1.4), molecular dynamics schemes for a simulation within this framework had to be developed. Three approaches will be mentioned here, while only two of them are of interest for this work.

Firstly, there are *Ehrenfest Molecular Dynamics*. In this method, classical equations of motion for the electrons are solved simultaneously with the Schrödinger equation for the electrons. Thus, this approach is seen to include rigorously non-adiabatic transitions between different electronic states. However, in Ehrenfest dynamics the time scale and therefore the time step to integrate the equations of motion simultaneously is dictated by the intrinsic dynamics of the electrons, which leads to a tremendous computational effort. This method has not been used in this work, an introduction can be found in [15].

The bottleneck of Ehrenfest dynamics is the simultaneous treatment of electrons and nuclei. In *Born-Oppenheimer Molecular dynamics* this is circumvented by first solving the Schrödinger equation for the electrons with fixed ions and then the equations of motion for the nuclei, which are moving on the potential energy surface (PES) created by the electrons. Thus, much larger time steps can be achieved. In turn, the inclusion of transitions between electronic states is much more difficult. The basic steps of a Born-Oppenheimer (BO) MD simulation are presented in Sec. 2.4.2.

Finally, there is the method introduced by Car and Parrinello in 1985, thus called *Car-Parrinello Molecular Dynamics*. It can be seen as a combination of the

advantages of the methods mentioned before. Again, the nuclei move on the PES given by the electrons, but the Schrödinger equation is not solved in each step. Instead, the orbitals are treated as "fictitious particles" and thus are given a mass and move according to their own equations of motion. Details are given in Sec. 2.4.3.

In most cases, the quantities of interest are properties that are averaged over a long MD simulation. That means, that actually a sampling of the whole available phase space is desired, leading to a statistical average for the observed quantity. This is necessary, if the experimental time scale is much longer than the time scale of the molecular motion. In this work, mostly NMR parameters are investigated and the typical time scales for NMR experiments are longer than 10^{-8}s, which is at least a factor of 10^6 longer than e.g. molecular vibrations. In principle, the necessary sampling of the phase space can also be achieved with a Monte Carlo scheme, which has originally been invented for the numerical treatment of phase space integrals. An advantage of MD simulations is that they capture the time evolution of the system and therefore allow the investigation of properties that rely on the actual time dependence of the degrees of freedom. Such a parameter, the NMR longitudinal relaxation time T_1, is presented in Chapter 6.

2.4.2 Born-Oppenheimer MD

The scheme for Born-Oppenheimer MD relies on the Born-Oppenheimer approximation. Still, there is a further approximation, that is not included in the original work of Born and Oppenheimer. As shown in Sec. 2.1.2, the molecular wave function can be separated into a nuclear and an electronic contribution due to the different masses of the respective particles. The additional assumption is, that the nuclei can be treated as classical particles, that move on the potential energy surface given by the electrons. As pointed out in Eq. (2.13), the electronic Hamiltonian depends parametrically on the positions of the nuclei, it is given by

$$\mathcal{H}^{el} = \sum_i -\frac{\hbar^2}{2m_e}\nabla_i^2 + \frac{1}{2}\sum_{i\neq j}\frac{e^2}{|\boldsymbol{r}_i - \boldsymbol{r}_j|} - \sum_{iI}\frac{e^2 Q_I}{|\boldsymbol{r}_i - \boldsymbol{R}_I|} \,. \tag{2.92}$$

The electronic ground-state wave function is found as the wave function, that minimizes the energy functional, the forces acting on the nuclei can be obtained as the gradient of the energy with respect to the atomic position. The resulting Born-Oppenheimer MD is defined by

$$\begin{aligned} M_I \ddot{\boldsymbol{R}}_I &= -\nabla_I \min_{\Psi_0} \{\langle \Psi_0 | \mathcal{H}^{el} | \Psi_0 \rangle\} \\ E_0 | \Psi_0 \rangle &= \mathcal{H}^{el} | \Psi_0 \rangle \ . \end{aligned} \tag{2.93}$$

This implies that the electronic Schrödinger equation must first be solved assuming fixed nuclear positions. Next, the nuclei are moved according to the classical equations of motion due to the forces calculated from the electronic ground-state wave function as given above. A typical algorithm can be described as follows:

1. Solve the Schrödinger equation for the electrons. The positions of the nuclei are fixed parameters.
2. Calculate the forces on the nuclei as the gradient of the energy obtained with the wave function from the previous step.
3. Move the nuclei according to the forces.
4. Start over with the first step, now with the updated atomic positions as parameters.

The major drawback of this method is, that the Schrödinger equation has to be solved explicitly for every MD step. This is by far the most computationally demanding task and limits the speed of the calculation. Modern quantum chemical codes, as CPMD or CP2K, make use of elaborated methods for the optimization of the wave function. For example, the wave function from the previous step is extrapolated as initial guess, which improves the convergence significantly. Besides that, efficient and reliable minimization techniques are employed that lead to an additional speed-up of the calculation [24].

2.4.3 Car-Parrinello MD

As mentioned in Sec. 2.4.1, the approach proposed by Car and Parrinello [1] can be seen as a compromise between Ehrenfest and Born-Oppenheimer MD. In the

beginning, the wave function is optimized, i.e. the wave function that minimizes the molecular energy is determined. Subsequently, the nuclei are moved similar as in BOMD, but then the wave function is not re-optimized, but rather adapted to the new nuclear configuration using fictitious equations of motion for the orbitals.

The derivation starts with the Lagrangian formulation of the system, instead of the Hamiltonian. Of course, both approaches are equivalent. Car and Parrinello postulated the following class of Lagrangians

$$\mathcal{L}_{CP} = \sum_I \tfrac{1}{2} M_I \ddot{\boldsymbol{R}}_I^2 + \sum_i \tfrac{1}{2}\mu_i \langle \dot{\psi}_i | \dot{\psi}_i \rangle - \langle \Psi_0 | \mathcal{H}^{el} | \Psi_0 \rangle + constraints \tag{2.94}$$

to exhibit the desired properties. The wave function Ψ_0 is assumed to be a Slater determinant (or a sum of several determinants) using one-particle orbitals ψ_i, e.g. Kohn-Sham orbitals. The μ_i are the crucial parameters of this method, which act as a "fictitious mass" or inertia parameter for the orbitals. The first and second terms on the right hand side of Eq. (2.94) are the kinetic energy of the whole system, which now consists of both nuclear and electronic degrees of freedom. The third part is the potential energy and the last term is due to constraints, as for example the orthonormality of the wave functions. This terms gives rise to "constraint forces" in the equations of motion. These can be obtained from the associated Euler-Lagrange equations

$$\begin{aligned} \frac{d}{dt}\frac{\partial \mathcal{L}}{\partial \dot{\boldsymbol{R}}_I} &= \frac{\partial \mathcal{L}}{\partial \boldsymbol{R}_I} \\ \frac{d}{dt}\frac{\delta \mathcal{L}}{\delta \dot{\psi}_i^*} &= \frac{\delta \mathcal{L}}{\delta \psi_i^*} \ , \end{aligned} \tag{2.95}$$

where $\psi_i^* = \langle \psi_i |$. Following this route, the Car-Parrinello equations of motion can be found to be of the form

$$\begin{aligned} M_I \ddot{\boldsymbol{R}}_I(t) &= -\frac{\partial}{\partial \boldsymbol{R}_I}\langle \Psi_0 | \mathcal{H}^{el} | \Psi_0 \rangle + \frac{\partial}{\partial \boldsymbol{R}_I}\{constraints\} \\ \mu_i \ddot{\psi}_i(t) &= -\frac{\delta}{\delta \psi_i^*}\langle \Psi_0 | \mathcal{H}^{el} | \Psi_0 \rangle + \frac{\delta}{\delta \psi_i^*}\{constraints\} \ . \end{aligned} \tag{2.96}$$

Thus, the orbitals are treated as fictitious particles with mass μ_i. These orbital masses are therefore the most important parameters in the CP formalism. Since

the kinetic energy of the orbitals, as given in Eq. (2.94) contribute to the total energy, one has to make sure, that this term is small compared to the nuclear energy. Additionally, there should be no coupling, i.e. energy exchange, between the fictitious and the real degrees of freedom. If the μ_i are chosen carefully, the electronic wave functions can be propagated due to the equations of motion Eq. (2.96) and no re-optimization of the wave function is necessary. The system will stay close to the exact "Born-Oppenheimer surface", i.e. the real, instantaneous ground state. In order to have well separated electronic and nuclear energy spectra, the fictitious masses have to be kept small, which, in turn, requires a small time step, because otherwise the orbitals gain to much "momentum" and deviate far from the BO surface. Typically the time step in a CP simulation is five times shorter than the time step in a corresponding BO simulation.

The fact that the system is only close and not on the BO surface and the effects arising from that have been discussed extensively in the literature. Recently, it has been shown, that the instantaneous forces in a CPMD do not agree with a respective BOMD [28]. However, in most cases it is not the instantaneous properties that are of interest, but rather a statistical average over a long MD simulation. These averages, instead, seem not to exhibit a difference for BO and CP [29, 30].

2.4.4 Realization of the NVT-Ensemble

The MD schemes that have been presented in the previous sections only used the intrinsic energy of the system for the calculation of the forces, i.e. a closed system has been assumed. Thus, the total energy is preserved. Besides that, the volume V and the number of particles N is constant. Therefore, the microcanonical ensemble, also referred to as NVE ensemble, is simulated. In many cases, this does not represent the experimental situation, where the temperature T of the sample is given by the environment, corresponding to a NVT or canonical ensemble. There are several methods for obtaining such an ensemble in a MD simulation. Anderson has proposed to include stochastic "collisions" of the particles, i.e. at intervals some or all of the velocities are resampled according to the Boltzmann distribution [31]. This method has the disadvantage that it does not yield a con-

tinuous trajectory with well defined conserved quantities anymore. The approach used in this work is based on the *extended-phase-space* approach, originally proposed by Nosé [32], then extended by Nosé and Hoover [33] and finally brought to its final form by Tuckerman and Martyna [34]. It is based on the introduction of new, unphysical degrees of freedom that represent the coupling to the heat bath. The equations of motion are defined as follows:

$$\begin{aligned}
\dot{q}_i &= \frac{p_i}{m} \\
\dot{p}_i &= -\frac{\partial V(\boldsymbol{q})}{\partial q_i} - p_i \frac{p_\eta}{Q} \\
\dot{p}_\eta &= \sum_{i=1}^{3N} \frac{p_i^2}{m_i} - NkT \\
\dot{\eta} &= \frac{p_\eta}{Q} \ .
\end{aligned} \tag{2.97}$$

The system contains N particles with coordinates q_i and momenta p_i, V is the potential, T the temperature of the heat bath and k the Boltzmann constant. The variable η and its momentum p_η corresponds to the new degree of freedom, the thermostat, which is only introduced for reproducing the desired ensemble. η is actually decoupled from the dynamics, it is only shown for completeness. Additionally, the equation for η helps with the interpretation of the parameter Q. It can be considered the mass of the new, fictitious particle. This mass has to be chosen in a way, that the coupling between the thermostat and the real degrees of freedom is optimal. Often, the fastest vibrational frequency of the real system is taken as a good reference for Q. Eq. (2.97) reveals, that the momentum p_η acts as a friction term for the momenta p_i. It is increased, if the kinetic energy of the real system is greater than NkT, decreased if the energy is smaller. These equations of motion are supposed to reproduce the desired Boltzmann distribution for the canonical ensemble.

Unfortunately it turns out, that even for the harmonic oscillator this is not the case. However, the problem can be cured, if not only a single thermostat, but a chain of thermostat is used. That means, that the thermostat η itself is coupled to a second thermostat, which is coupled to a third one, and so on. Tuckerman and Martyna showed, that a chain of length 3 is sufficient to yield almost perfect

agreement with the theoretical distribution. The equations of motion for the general case can be found in [34].

Finally, it should be noted that within this extended system approach, the conserved quantity is not the total energy of the real system but the extended Hamiltonian below:

$$H' = V(\boldsymbol{q}) + \sum_{i=1}^{3N} \frac{p_i^2}{2m_i} + \frac{p_\eta^2}{2Q} + NkT\eta \ . \tag{2.98}$$

Therefore, this quantity needs to be monitored during the simulation and is a measure for the quality of the MD run. A good conservation of H' lends credence to the choices of the parameters used.

3 Calculation of Spectroscopic Properties

3.1 Introduction

In the previous chapter, the DFT formalism has been introduced. Furthermore, some practical aspects, such as basis sets and pseudopotentials, have also been treated. However, the above has focused on finding the ground-state probability density of the considered system. Although quantum chemists have spent most of their effort on the construction of wave functions and densities, the final aim of a quantum chemical calculation is often neither the wave function nor the energy, but rather some physical property, that can be measured directly. There is a huge variety of such properties, but in general one can say, that the response of the system to an external perturbation is interrogated. The perturbation can e.g. be a magnetic or an electric field, but also a combination of various fields.

In this work, two specific experimental properties are treated. Both can be parameters of a Nuclear Magnetic Resonance (NMR) experiment: The *NMR chemical shift* and the *Nuclear Quadrupole Coupling Constant* (NQCC). While both start with the solution of the Schrödinger equation for the unperturbed problem, the subsequent calculation is different:

- On the one hand, there are the NQCCs, which are, roughly speaking, proportional to the electric field gradient (EFG) at the nucleus. The EFG, in turn, can be computed from the ground-state electronic density and is therefore called a "first-order" or "ground-state" property. Other examples for this class of properties are the dipole moment and higher multipole moments or the density or spin density at the nucleus, from which hyperfine coupling constants can be obtained.
- On the other hand, there is the NMR chemical shift, which is a "second-order property". It is the result of chemical bonding environments interacting with

the applied magnetic field. In order to treat it properly, theoretically, its calculation requires some kind of perturbation theory after the ground-state has been determined. Besides the chemical shift, there other examples, as electric polarizability, magnetic susceptibilities or indirect spin-spin coupling.

Of course, there are many more properties, that can be calculated in a quantum chemical calculation, as for example those that involve more than one electronic state, e.g. optical transition energies and intensities or ionization potentials. Sometimes even the Born-Oppenheimer approximation is not sufficient for some parameters, as non-adiabatic transition probabilities or Jahn-Teller distortions. Another class that should be mentioned are harmonic force constants, which imply harmonic vibration frequencies and eventually infrared and Raman spectra. These can be obtained from the potential energy surface (PES), i.e. the electronic energy as a function of the nuclear coordinates.

While all these properties can give valuable insight into the structure and dynamics of a molecular system, and all of these are also subject to theoretical investigations, this work will only deal with the two above-mentioned, chemical shifts and NQCCs, and therefore only an introduction these is given in the following. For a more detailed and complete overview, the reader is referred to Ref. [35].

3.2 Ground State Properties

3.2.1 Nuclear Quadrupole Coupling Constants (NQCC)

Besides the NMR chemical shift (see Sec. 3.3.2), that is often considered in NMR spectroscopy, there are other interactions, as for example dipole-dipole couplings, or, if the involved nucleus possesses a spin $I \geq 1$, the nuclear quadrupole coupling. Then, the nucleus can exhibit a static quadrupole moment and therefore interact with the electric field gradient (EFG) at its position.

Starting point for the derivation of the NQCC is the classical quadrupole energy E^Q of a nucleus with charge density ρ_n with respect to the EFG [36, 37]:

$$E^Q = \frac{1}{6} \sum_{i,j} V_{ij} Q_{ij} \ , \tag{3.1}$$

where

$$Q_{ij} = \int (3x_i x_j - \delta_{ij} r^2) \rho_n d\tau \tag{3.2}$$

is the *electric quadrupole moment tensor* and

$$V_{ij} \equiv \left. \frac{\partial^2 V}{\partial x_i \partial x_j} \right|_{r=0} , \tag{3.3}$$

is the *electric field gradient* of the external potential V with the nucleus at the origin of the coordinate system. The quadrupole moment tensor from Eq. (3.2) can be simplified, if one considers that the nucleus consists of nuclear particles, i.e. neutrons and protons, which can be treated as point-particles. Since the neutrons are neutral, the nuclear charge density is

$$\rho_n(\boldsymbol{r}) = \sum_{protons} \delta(\boldsymbol{r}_p - \boldsymbol{r}) \ . \tag{3.4}$$

Substituting this into Eq. (3.2) yields:

$$\begin{aligned} Q_{ij} &= \int (3x_i x_j - \delta_{ij} r^2) \rho_n d\tau \\ &= \sum_{protons} \int (3x_i x_j - \delta_{ij} r^2) \delta(\boldsymbol{r}_p - \boldsymbol{r}) d\tau \end{aligned}$$

$$= \sum_{protons} (3x_{ip}x_{jp} - \delta_{ij}r_p^2) \ . \tag{3.5}$$

The last equation is the classical expression for the electric quadrupole moment tensor of a system of charged point-particles. The corresponding quantum mechanical operator can be found by replacing the classical variables by operators, i.e.

$$Q_{ij}^{Op} \equiv \mathcal{Q}_{ij} = \sum_p (3\hat{x}_{ip}\hat{x}_{jp} - \delta_{ij}\hat{r}_p^2) \ . \tag{3.6}$$

The sum "over p" is equivalent with the sum "over the protons". Thus, the quantum mechanical Hamiltonian of the quadrupole coupling is given by

$$\mathcal{H}_Q = \frac{1}{6}\sum_{i,j} V_{ij}\mathcal{Q}_{ij} = \frac{1}{6}\sum_{i,j} V_{ij} \sum_p (3\hat{x}_{ip}\hat{x}_{jp} - \delta_{ij}\hat{r}_p^2) \ . \tag{3.7}$$

In NMR theory, one always considers transitions with respect to the magnetic quantum number m. Therefore, it is useful to express the above equations in terms of spin operators $\mathcal{I}_i$ and $\mathcal{I}^2$ instead of position operators. This can be done with help of the *Wigner-Eckart theorem* [38, 36]. According to this theorem, the matrix elements of the operator $\mathcal{Q}_{ij}$ with the eigenstates $|Im\alpha\rangle$[1] of the nucleus can be written as

$$\begin{aligned} \langle Im\alpha|\mathcal{Q}_{ij}|Im'\alpha\rangle &= \langle Im\alpha| \sum_p (3\hat{x}_{ip}\hat{x}_{jp} - \delta_{ij}\hat{r}_p^2)|Im'\alpha\rangle \\ &= \langle Im\alpha|3\frac{(\mathcal{I}_i\mathcal{I}_j + \mathcal{I}_j\mathcal{I}_i)}{2} - \delta_{ij}\mathcal{I}^2|Im'\alpha\rangle \ C \ , \end{aligned} \tag{3.8}$$

where the summation over the protons disappears, because I is the total spin of the system and thus already contains the sum. C is the *reduced matrix element* and is a constant with respect to m, i and j. This constant can be determined, if the matrix element for $m = m' = I$ and $i = j = 3$ is considered:

$$\begin{aligned} \langle II\alpha| \sum_p (3\hat{x}_{3p}^2 - \hat{r}_p^2)|II\alpha\rangle &= C \ \langle II\alpha|3\mathcal{I}_3^2 - \mathcal{I}^2|II\alpha\rangle \\ &= C \ I(2I-1) \ . \end{aligned} \tag{3.9}$$

[1] Besides I and m there might be other quantum numbers, which are combined into α. They commutate with the spin operators and therefore are not of further importance here.

If the *quadrupole moment* Q of the nucleus is defined by

$$Q \equiv \langle II\alpha | \sum_p (3\hat{x}_{3p}^2 - \hat{r}_p^2) | II\alpha \rangle \ , \tag{3.10}$$

the constant C is given by

$$C = \frac{Q}{I(2I-1)} \ . \tag{3.11}$$

The quantum numbers I and α are unchanged in an NMR experiment and thus, the set of possible states can be limited to those with fixed I and α. The Hamiltonian from Eq. (3.7) then reads

$$\mathcal{H}_Q = \frac{Q}{6I(2I-1)} \sum_{ij} V_{ij} \left[3\frac{\mathcal{I}_i\mathcal{I}_j + \mathcal{I}_j\mathcal{I}_i}{2} - \delta_{ij}\mathcal{I}^2 \right] \ . \tag{3.12}$$

A further simplification can be achieved if the problem is treated in the principle axes system of the tensor V_{ij} and Laplace's equation,

$$\Delta V(0) = \sum_i V_{ii} = 0 \ , \tag{3.13}$$

is used. The trace of V_{ij} is equated to zero, because the only contribution to the charge at the nucleus is due to the s-orbitals, which are isotropic and thus act as an additive constant that is not seen in the experiment. The Hamiltonian then becomes

$$\mathcal{H}_Q = \frac{Q}{4I(2I-1)} \left[V_{33}(3\mathcal{I}_3^2 - \mathcal{I}^2) + (V_{11} - V_{22})(\mathcal{I}_1^2 - \mathcal{I}_2^2) \right] \ . \tag{3.14}$$

It can be seen, that only two parameters are needed for the characterization of the Hamiltonian: V_{33} and $V_{11} - V_{22}$. Therefore, two new quantities are defined, the *field gradient* q and the *asymmetry* η:

$$\begin{aligned} q &= V_{33} \\ \eta &= \frac{V_{11} - V_{22}}{V_{33}} \ . \end{aligned} \tag{3.15}$$

In the following the convention $|V_{33}| \geq |V_{11}| \geq |V_{22}|$ will be used. The field gradient q is directly proportional to the measured NQCC.

In an NMR experiment there is always a strong magnetic field present. If the asymmetry is assumed to vanish, i.e. $V_{11} = V_{22}$, the appropriate Hamiltonian is

$$\mathcal{H} = -\gamma_n H_0 \mathcal{I}_{3'} + \frac{qQ}{4I(2I-1)}(3\mathcal{I}_3^2 - \mathcal{I}^2) \ , \tag{3.16}$$

where the first term is the Zeeman interaction with the magnetic field H_0. As the primed spin operators indicate, the principal axes system of the EFG and the system given by the external magnetic do not coincide. In case the quadrupole coupling is weak compared to the magnetic interaction, the spin can be considered quantized along the $3'$ axis. The quadrupole interaction can then be treated as perturbation, i.e. the energy is in first approximation the expectation value of the unperturbed states $|Im\alpha\rangle \equiv |m\rangle$. Since the quantum numbers I and α are not changed, they will be omitted in the following. If the operators in the unprimed system are expressed in the primed coordinates, the energy in the state $|m\rangle$, given as $\langle m|\mathcal{H}|m\rangle$, can be written as follows [36, p. 498]:

$$E_m = -\gamma_n H_0 m + \frac{qQ}{4I(2I-1)} \left(\frac{3\cos^2\theta - 1}{2} \right) [3m^2 - I(I+1)] \ . \tag{3.17}$$

If one considers transitions with $\Delta m = \pm 1$, the possible transition energies for a nucleus with $I = 1$ are $|E_{-1} - E_0|$ and $|E_0 - E_1|$. In Fig. 3.1 the shift of the states and the transitions are shown. The difference of the energies is

$$\Delta E = \frac{3}{2} \frac{qQ}{I(2I-1)} \left(\frac{3\cos^2\theta - 1}{2} \right) \ . \tag{3.18}$$

Usually the NQCC is given as the frequency corresponding to the transition energy ΔE at $\theta = \pi/2$,

$$\nu_{NQCC} = \frac{3}{4} \frac{qQ}{Ih(2I-1)} \ . \tag{3.19}$$

The general case with $\eta \neq 0$ is treated in [39] and the equation for ΔE is then given by

$$\Delta E = \frac{3}{2} \frac{qQ}{I(2I-1)} \cdot \frac{1}{2} \left(3\cos^2\theta - 1 - \eta \ \sin^2\theta \cos(2\phi) \right) \ , \tag{3.20}$$

where (θ, ϕ) are the polar and azimuth angle of the magnetic field H_0 in the

principal axes system of the EFG.

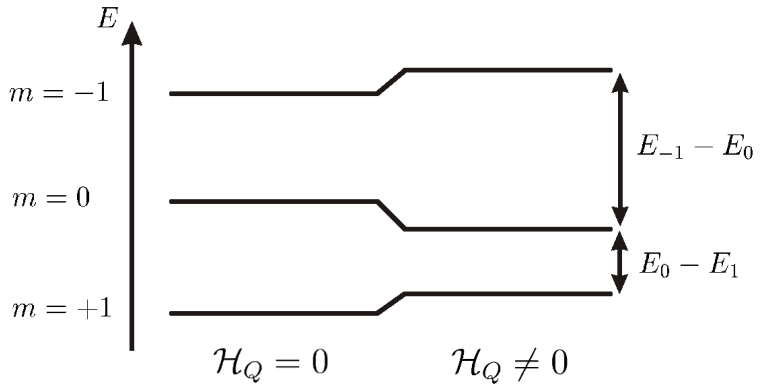

Figure 3.1: Schematic depiction of the shift of the energy levels due to the quadrupole coupling for a nucleus with $I = 1$.

The computation of the transition energies due to quadrupole interactions require the knowledge of the nuclear quadrupole moment and the EFG at the nucleus. The quadrupole moments are usually taken from experimental data, since it is very difficult to obtain theoretically. The EFG, instead, can be computed from the electron density of the considered system. How this is done in the framework of DFT is described in the following section.

3.2.2 Calculation of Electric Field Gradients

The NQCC is proportional to the EFG at the nucleus. This has been demonstrated in Sec. 3.2.1. Still, it is not clear how the EFG can be obtained in a quantum chemical calculation. In this section, the computation as implemented in CP2K [21] is introduced, following the method of Blöchl et al. [40]. The procedure is applied to the GAPW method (see Sec. 2.3.2) and is thus somewhat more complicated than in a pure plane wave environment as employed in CPMD [20]. In this work both "pure" plane waves and GAPW have been used for the calculation of EFG. Since in GAPW the smooth density is represented by plane waves, the method presented here includes the one used in a pure plane wave code. Only the one-center terms have to be omitted in this case.

In general the EFG of an electrostatic potential is given by the second derivative with respect to the position. The potential is in this case the full Hartree potential

$v^H(\boldsymbol{r})$, similar to Eq. (2.75). Since the NQCC is a interaction of the EFG at the nucleus site with the spin, the derivatives are taken at the nuclear site $\boldsymbol{R}$:

$$V_{ij} = \lim_{\boldsymbol{r}\to\boldsymbol{R}} (\partial_i \partial_j - \tfrac{1}{3}\delta_{ij}\nabla^2) v^H(\boldsymbol{r}) \ . \tag{3.21}$$

The δ-term is introduced in order to make V_{ij} traceless (see Eq. 3.13). As described in Sec. 2.3.2, the density in the GAPW method is given as a sum of three terms

$$\rho = \tilde{\rho} - \sum_A \tilde{\rho}_A^1 + \sum_A \rho_A^1 \ , \tag{3.22}$$

and each of them gives rise to a contribution to the potential, i.e.

$$v^H(\boldsymbol{r}) = \tilde{v}(\boldsymbol{r}) - \sum_A \tilde{v}_A^1(\boldsymbol{r}) + \sum_A v_A^1(\boldsymbol{r}) \ . \tag{3.23}$$

The first term $\tilde{v}(\boldsymbol{r})$ is called *pseudopotential*. It should not be confused with the pseudopotential as presented in Sec. 2.2.1. In this case, the pseudopotential is just the plane wave part of the all-electron potential. The remaining two terms are the one-center expansions of the pseudopotential and the all-electron potential, respectively, at the atomic site $\boldsymbol{R}$. Each part of the potential contributes to the EFG individually:

$$V_{ij} = \tilde{V}_{ij} - \tilde{V}_{ij}^1 + V_{ij}^1 \ . \tag{3.24}$$

In a pure plane wave environment, only $\tilde{V}_{ij}$ is present. The corresponding EFG can be obtained easily in the reciprocal space. This is achieved by evaluating the EFG in the reciprocal space. It is then a function of the reciprocal lattice vectors $\boldsymbol{G}$. A subsequent Fourier transformation at the nucleus yields the desired EFG:

$$\tilde{V}_{ij} = -\sum_{\boldsymbol{G}} (G_i G_j - \delta_{ij}\tfrac{1}{3}|\boldsymbol{G}|^2)\tilde{v}(\boldsymbol{G}) e^{i\boldsymbol{G}\boldsymbol{R}} \ . \tag{3.25}$$

The one-center contributions can be treated analytically, since the wave functions are given by Gaussians and therefore the potential can be evaluated easily. In the following, the calculation for $v_A^1(\boldsymbol{r})$ is shown, the procedure for $\tilde{v}_A^1(\boldsymbol{r})$ is equivalent. The potential is expanded in spherical harmonics, an approach appropriate to the symmetry of the problem. Y_L are the respective harmonics with angular

momentum $L = (l, m)$. The potential is then given by

$$v_A^1(\boldsymbol{r}) = \sum_A v_{A,L}^1(|\boldsymbol{r} - \boldsymbol{R}|) Y_L(\boldsymbol{r} - \boldsymbol{R}) \ , \tag{3.26}$$

where $v_{A,L}^1$ is the radial part of the potential for a given L, centered at an atomic site R. In the following, the new variable $\boldsymbol{s} = \boldsymbol{r} - \boldsymbol{R}$ will be used for simplification, s is the absolute value of $\boldsymbol{s}$. Then the second derivatives of the potential can be written as

$$\begin{aligned} \partial_i \partial_j \sum_A v_{A,L}^1(s) Y_L(\boldsymbol{s}) = \lim_{s \to 0} \sum_A & [(\partial_i \partial_j v_{A,L}^1(s) s^{-l})(Y_L(\boldsymbol{s}) s^l)] \\ & + (\partial_i v_{A,L}^1(s) s^{-l})(\partial_j Y_L(\boldsymbol{s}) s^l) \\ & + (\partial_j v_{A,L}^1(s) s^{-l})(\partial_i Y_L(\boldsymbol{s}) s^l) \\ & + v_{A,L}^1(s) s^{-l} (\partial_i \partial_j Y_L(\boldsymbol{s}) s^l)] \ . \end{aligned} \tag{3.27}$$

This expression can be reduced due the properties of the involved functions. The $Y_L(\boldsymbol{s}) s^l$ are polynomials of order l, so the first term vanishes except for the $l = 0$ contribution, the second and third except for the $l = 1$ contribution and the last term except for the $l = 2$ contribution. The term that is proportional to $l = 0$ does not play a role for the EFG, since it is isotropic and therefore only yields an additive constant, which is not seen experimentally. The $l = 1$ terms vanish, because they always appear in the form $\partial_j v_{A,L}^1(s)/s$ and such a spherical function has a vanishing gradient at the origin. Thus, only the $l = 2$ remains, yielding for the EFG

$$V_{ij}^1 = \sum_{m;l=2} \left(\lim_{s \to 0} \frac{v_{A,L}^1(s)}{s^2} \right) [(\partial_i \partial_j - \tfrac{1}{3} \delta_{ij} \nabla^2) Y_L(\boldsymbol{s}) s^2] \ . \tag{3.28}$$

Explicit formulas for the individual components can be found in [40]. At the end, the total EFG is obtained by adding all contributions according to Eq. (3.24).

3.2.3 Relaxation via Quadrupole Couplings

The NQCC can be observed directly in an NMR spectrum, as described in the previous sections. It leads to a typical line shape ("Pake pattern") in the solid state due to its angular dependence, shown in Eq. (3.20). In the liquid state,

or the gas phase, the molecular motion in general occurs on a much shorter time scale than the NMR measurement, and so the quadrupolar interaction is averaged out. Since it does not have an isotropic part, as the NMR chemical shift, it cannot be seen anymore in such an environment. Still, there is an indirect way of observing the quadrupole couplings even in the liquid state. For nuclei with a spin $I \geq 1$ it contributes to the relaxation of the spins, i.e. the re-equilibration of the system after it has been perturbed by an electro-magnetic pulse. The quadrupole coupling does not only contribute to the relaxation, it can even be considered the main term in many systems [41, 42, 43]. Since it depends both on the EFG and the molecular dynamics, relaxation times are a difficult quantity for quantum chemical simulations. Relaxation is an important issue in NMR and its theory has been discussed at length by many authors, therefore a complete description is beyond the scope of this work. A detailed introduction is given in Ref. [42] or Ref. [43]. Here, only a short summary will be provided, including the most important formulas and the necessary background of the calculation.

The starting point for the derivation is the equation of motion of the density matrix in the rotating frame ρ^* (see [43, Chapter VIII, Eq. (33)]):

$$\frac{d\rho^*}{dt} = -\int_0^\infty \langle [\mathcal{H}^*(t), [\mathcal{H}^*(t-\tau), \rho^*(t)]] \rangle \; d\tau \;, \tag{3.29}$$

where $\langle \cdots \rangle$ denotes an ensemble average. The asterisk indicates, that this is the equation in the interaction representation, or "rotating frame". This means, that the Zeeman-interaction has been separated and the coordinate system rotates with the Larmor-frequency ω. The density matrix ρ is the population matrix of the available spin states, i.e.

$$\rho_{mm'} = \langle m|\hat{\rho}|m'\rangle = \overline{a^+_{m'} a_m} \;, \tag{3.30}$$

with the density operator $\hat{\rho}$. $|a_m|^2$ is the probability of finding a spin in the state m and the bar denotes the ensemble average (different from Eq. (3.29)). The Hamiltonian $\mathcal{H}$ is the quadrupole interaction Hamiltonian, given here in its representation using irreducible tensor operators. Its explicit form can be found

in [42], especially see Tab. 2.3 and Tab. 2.4. The Hamiltonian can be written as

$$\mathcal{H} = C \sum_{m=-2}^{2} (-1)^m T_{2m} R_{2-m} \ , \tag{3.31}$$

where T_{2m} contains the spin part and R_{2m} the space dependent parts of the interaction, C is a constant which is specific for the considered interaction. For the case of the quadrupole interaction this means, that the R_{2m} are the elements of the EFG in its representation as irreducible tensor. If V_{ij} with $i, j = x, y, z$ are the cartesian elements, the R_{2m} are given as follows:

$$\begin{aligned} R_{20} &= \frac{3}{\sqrt{6}} V_{zz} \ , \\ R_{2\pm1} &= \mp V_{xz} \ , \\ R_{2\pm2} &= \tfrac{1}{2}[V_{xx} - V_{yy} \pm 2iV_{xy}] \end{aligned} \tag{3.32}$$

where the fact that the tensor is traceless and symmetric has been used. If the Hamiltonian from Eq. (3.31) is inserted in Eq. (3.29) and only the secular terms with $m' = -m$ are considered, one finds

$$\begin{aligned} \frac{d\rho^*}{dt} = -C^2 &\sum_{m=-2}^{2} [T_{2m}, [T_{2-m}, \rho^*]] \\ &\cdot \int_0^\infty \langle R_{2-m}(t) R_{2m}(t-\tau) \rangle e^{im\omega\tau} \, d\tau \ . \end{aligned} \tag{3.33}$$

The autocorrelation functions encountered here will be denoted by $f_{lm}(\tau)$:

$$f_{lm}(\tau) \equiv (-1)^{l+m} \langle R_{l-m}(t) R_{lm}(t-\tau) \rangle \ , \tag{3.34}$$

and their half-sided Fourier transforms by $g_{lm}(\omega)$:

$$g_{lm}(\omega) \equiv \int_0^\infty f_{lm}(\tau) e^{i\omega\tau} \, d\tau \ . \tag{3.35}$$

So far, the whole density matrix has been considered, while the quantity of interest is the expectation value of the spin operator I_z, which gives the ensemble magnetization in the z-direction if averaged over all spins. The longitudinal relax-

ation time T_1 is a measure for the buildup of this magnetization in the experiment. Thus, the the time dependence of the spin component I_z has to be calculated, which can be written as

$$\left\langle \frac{dI_z}{dt} \right\rangle = -C^2\{\frac{2}{\sqrt{10}}[4g_{22}(2\omega) + 4g_{2-2}(-2\omega) + g_{21}(\omega) + g_{2-1}(-\omega)]\langle T_{10}\rangle + \frac{4}{\sqrt{10}}[g_{22}(2\omega) + g_{2-2}(-2\omega) - g_{21}(\omega) - g_{2-1}(-\omega)]\langle T_{30}\rangle\} \ . \quad (3.36)$$

In the limit of rapid motions, i.e. the typical correlation time is much shorter than the NMR time scale, given by ω, the g_{lm} are independent of the frequency and independent of m. This means that the term proportional to T_{30} vanishes. This situation of *extreme narrowing* will always be present in the systems investigated here. Furthermore, the $\langle T_{10}\rangle$ can be expressed in terms of $\langle I_z\rangle$ with the help of the Wigner-Eckart theorem [42, p. 113]. Thus, Eq. (3.36) can be transformed into

$$\left\langle \frac{dI_z}{dt} \right\rangle = -\frac{e^2Q^2(2I+3)}{40I^2(2I-1)\hbar^2} G_{20}(\omega)\langle I_z\rangle \ , \quad (3.37)$$

with

$$G_{20}(\omega) = 4g_{22}(2\omega) + 4g_{2-2}(-2\omega) + g_{21}(\omega) + g_{2-1}(-\omega) \ . \quad (3.38)$$

In Eq. (6.1) the electron charge e and the quadrupole moment Q of the considered nucleus have been used. If this equation is compared to the Bloch equation for the spin component I_z,

$$\left\langle \frac{dI_z}{dt} \right\rangle = -\frac{1}{T_1}\langle I_z\rangle \ , \quad (3.39)$$

(see [43, p. 44]) the relaxation time T_1 is found as

$$\frac{1}{T_1} = \frac{e^2Q^2(2I+3)}{40I^2(2I-1)\hbar^2} G_{20}(\omega) \ . \quad (3.40)$$

A computational determination of the longitudinal relaxation time T_1 therefore requires the calculation of the autocorrelation functions $f_{lm}(\tau)$ in a molecular dynamics simulation of the considered system. Such a calculation is presented in Chapter 6.

3.3 Second-Order Properties

3.3.1 General

NMR chemical shifts are "second-order" properties and therefore require a treatment within perturbation theory. Since only the terms linear in the external perturbation are considered, such computations are commonly referred to as *Linear Response Calculations*. The chemical shift is actually caused by a change of the wave function due to an external magnetic field. This field induces electronic currents, which interacts with the nuclear spins, additionally to the external field. The dependence of this current and the induced magnetic field on the external field is described by the NMR chemical shift.

Before treating the problem of the chemical shifts itself, some basic facts about perturbation theory will be recalled. In perturbation theory it is assumed, that the unperturbed problem has already been solved, i.e.

$$\mathcal{H}_0|\Psi_0\rangle = E_0|\Psi_0\rangle \ , \tag{3.41}$$

where $|\Psi_0\rangle$ is the unperturbed ground-state wave function. Now, a small perturbation $\lambda\mathcal{H}_1$ is added to the original Hamiltonian $\mathcal{H}_0$:

$$\mathcal{H} = \mathcal{H}_0 + \lambda\mathcal{H}_1 \quad \text{mit} \quad \lambda \ll 1 \ . \tag{3.42}$$

By expanding the perturbed state $|\Psi\rangle$ and the energy E with respect to λ the change of $|\Psi_0\rangle$ and E_0 due to the perturbation can be evaluated.

In the following, the derivation of the equations for the chemical shift will be done in the "normal" Hamiltonian framework. The treatment within DFT (see Sec. 2.1) is described in Ref. [44]. In this work, the chemical shifts are calculated with the quantum chemical code CPMD [20], where periodic boundary conditions are employed. The periodicity causes additional problems because the position operator is ill-defined. There is a solution to this problem which can be found in Ref. [45], a detailed description is out of the scope of this thesis.

3.3.2 Chemical Shifts

The calculation of the chemical shift is done in two steps. First, the induced current in the electronic system due to the external magnetic field will be evaluated. Second, the induced magnetic field at the considered nucleus will be computed from this current. The second step will be done completely classically, with the help of the *Biot-Savart Law*.

The quantum mechanical treatment is required in the first step. The starting point is the unperturbed problem

$$\mathcal{H}_0|\Psi_n\rangle = E_n|\Psi_n\rangle \ , \tag{3.43}$$

where

$$\mathcal{H}_0 = \frac{\hat{p}^2}{2m_e} + V. \tag{3.44}$$

Here, the Gaussian system of units is used. The potential is given according to Eq. (2.13). The eigenfunctions $|\Psi_n\rangle$ are orthonormal and the eigenvalues E_n are not degenerated. This means, that the states $|\Psi_n\rangle$ can be chosen to be real. In the ground-state the system is in the state $|\Psi_0\rangle$.

The perturbation is a static magnetic field. A particle in a electro-magnetic field is described by replacing the momentum operator $\hat{\boldsymbol{p}}$ by $\hat{\boldsymbol{\pi}} = \hat{\boldsymbol{p}} - q/c\,\boldsymbol{A}$, with the charge q, c is the speed of light,

$$\begin{aligned} \mathcal{H} &= \frac{1}{2m_e}\left(\hat{\boldsymbol{p}} - \frac{q}{c}\boldsymbol{A}\right)^2 + V \\ &= \frac{\hat{p}^2}{2m_e} + V - \frac{q}{2m_e c}(\hat{\boldsymbol{p}}\cdot\boldsymbol{A} + \boldsymbol{A}\cdot\hat{\boldsymbol{p}}) + \frac{q^2}{2m_e c^2}A^2 \ . \end{aligned} \tag{3.45}$$

Commonly, the vector potential $\boldsymbol{A}$ of a static, homogeneous field $\boldsymbol{B}^{ext}$ is given by

$$\boldsymbol{A} = \frac{1}{2}\,\boldsymbol{B}^{ext} \times \boldsymbol{r} \ . \tag{3.46}$$

As always in electrodynamics, the vector potential has to be gauged. This causes non-trivial problems in this case, and so the problem is postponed to the next section. The parameter λ (see Eq. (3.42)) is here substituted by $\boldsymbol{A}$. The last term of Eq. (3.45) depends quadratically on $\boldsymbol{A}$ and is thus neglected in first approximation.

Thus, the perturbation operator $\mathcal{H}_1$ is given by

$$\mathcal{H}_1 = -\frac{q}{2m_e c}(\hat{\boldsymbol{p}} \cdot \boldsymbol{A} + \boldsymbol{A} \cdot \hat{\boldsymbol{p}}) \ . \tag{3.47}$$

Since the eigenfunctions of the unperturbed Hamiltonian constitute a complete and orthonormal system, the perturbed ground-state wave function in first approximation yields [38]:

$$|\Psi_0'\rangle = |\Psi_0\rangle + \sum_n \frac{\langle\Psi_n|\mathcal{H}_1|\psi_0\rangle}{E_0 - E_n} \ |\Psi_n\rangle = |\Psi_0\rangle + \sum_n \varepsilon_{n0}|\Psi_n\rangle \ . \tag{3.48}$$

ε_{n0} is defined by Eq. (3.48). In the next step, the quantum mechanical current $\boldsymbol{j}_{qm}(\boldsymbol{r})$ is needed, which is defined as the expectation value of the operator

$$\hat{\boldsymbol{j}}_{qm} = \frac{1}{2m_e} \ [\hat{\boldsymbol{\pi}}|\boldsymbol{r}\rangle\langle\boldsymbol{r}| + |\boldsymbol{r}\rangle\langle\boldsymbol{r}|\hat{\boldsymbol{\pi}}] \ . \tag{3.49}$$

If this quantum mechanical current is multiplied with the charge q, the desired current density of the electrons is found. In the ground-state of the perturbed system the electronic current density $q \cdot \langle\Psi_0'|\hat{\boldsymbol{j}}_{qm}|\Psi_0'\rangle$ reads

$$\begin{aligned} \boldsymbol{j}_{el}(\boldsymbol{r}) \ &= \ \frac{\hbar q}{2m_e i}(\Psi_0^*\nabla\Psi_0 - \Psi_0\nabla\Psi_0^*) + \sum_n \frac{\hbar q}{2m_e i}(\Psi_0^*\nabla\Psi_n - \Psi_n\nabla\Psi_0^*)\varepsilon_{n0} \\ &\quad + \sum_n \frac{\hbar q}{2m_e i}(\Psi_n^*\nabla\Psi_0 - \Psi_0\nabla\Psi_n^*)\varepsilon_{n0}^* - \frac{q^2}{m_e c}\boldsymbol{A}|\Psi_0|^2 \ . \end{aligned} \tag{3.50}$$

The first term is the current density of the unperturbed system. Since $|\Psi_0\rangle$ was chosen to be real, it vanishes. Hence, the induced current density is

$$\begin{aligned} \boldsymbol{j}_{el}(\boldsymbol{r}) \ &= \ \sum_n \frac{\hbar q}{2m_e i}(\Psi_0^*\nabla\Psi_n - \Psi_n\nabla\Psi_0^*)\varepsilon_{n0} + \sum_n \frac{\hbar q}{2m_e i}(\Psi_n^*\nabla\Psi_0 \\ &\quad - \Psi_0\nabla\Psi_n^*)\varepsilon_{n0}^* - \frac{q^2}{m_e c}\boldsymbol{A}|\Psi_0|^2 \ . \end{aligned} \tag{3.51}$$

With the last equation, the first part of the calculation of the chemical shift is accomplished. Now, the induced magnetic field at the nucleus due to this current density has to be computed. According to the Biot-Savart law it can be found

with the formula

$$\boldsymbol{B}^{ind}(\boldsymbol{r}) = \frac{1}{c}\int d^3r' \boldsymbol{j}_{el}(\boldsymbol{r}') \times \frac{(\boldsymbol{r}-\boldsymbol{r}')}{|\boldsymbol{r}-\boldsymbol{r}'|^3} \ . \tag{3.52}$$

The *chemical shielding tensor* for a nucleus at $\boldsymbol{R}_n$ is defined by

$$\sigma_{ij}(\boldsymbol{R}_n) \equiv -\frac{\partial B_i^{ind}(\boldsymbol{R}_n)}{\partial B_j^{ext}} \ , \qquad i,j = 1,2,3 \ . \tag{3.53}$$

Since the shielding in this approximation depends linearly on the field (see Eq. (3.51)), the energy of the Zeeman interaction with the magnetic moment of the nucleus $\boldsymbol{\mu}_n$ can be written as

$$\begin{aligned} E_n &= -\boldsymbol{\mu}_n \cdot \boldsymbol{B}(\boldsymbol{R}_n) = -\boldsymbol{\mu}_n \cdot (\boldsymbol{B}^{ext} + \boldsymbol{B}^{ind}(\boldsymbol{R}_n)) \\ &= -\boldsymbol{\mu}_n \cdot (\mathbf{1} - \boldsymbol{\sigma}(\boldsymbol{R}_n)) \cdot \boldsymbol{B}^{ext} \ . \end{aligned} \tag{3.54}$$

The experimental chemical shift $\boldsymbol{\delta}$ is the difference between the shielding of the considered nucleus and the same nucleus in a reference system

$$\boldsymbol{\delta} = \boldsymbol{\sigma}_{ref} - \boldsymbol{\sigma}(\boldsymbol{R}_n) \ . \tag{3.55}$$

In the experiment, there are often many different orientations of the molecule with respect to the external magnetic field and thus, only the *isotropic* part is measured,

$$\delta \equiv \delta_{iso} = \frac{1}{3}\,\mathrm{Spur}(\boldsymbol{\delta}) \ . \tag{3.56}$$

The same holds for $\boldsymbol{\sigma}$ and therefore only the isotropic values δ and σ are given in most cases. Finally, the problem of the gauge of the vector potential, that has been postponed, has to be treated. This will be done in the next section.

3.3.3 The gauge origin problem

According to Maxwell's equations a magnetic field $\boldsymbol{B}$ exhibits vanishing divergence, i.e.

$$\nabla \cdot \boldsymbol{B}(\boldsymbol{r}) = 0 \ . \tag{3.57}$$

Thus, $\boldsymbol{B}$ can be found as the curl of a vector potential $\boldsymbol{A}$:

$$\boldsymbol{B}(\boldsymbol{r}) = \nabla \times \boldsymbol{A}(\boldsymbol{r}) \ . \tag{3.58}$$

The vector potential, however, is not unique, i.e. if a vector potential $\boldsymbol{A}$, that yields the magnetic field $\boldsymbol{B}$, is found, there is an infinite number of other potentials giving the same magnetic field. These new potentials are connected with the first one via a *gauge transformation* of the form

$$\boldsymbol{A} \ \rightarrow \ \boldsymbol{A}' = \boldsymbol{A} + \nabla\phi(\boldsymbol{r}) \ . \tag{3.59}$$

The functions $\phi(\boldsymbol{r})$ are arbitrary scalar functions of the position $\boldsymbol{r}$. The physical field $\boldsymbol{B}$ is not affected by this transformation and thus, this degree of freedom is called *gauge invariance*.

In Eq. (3.46) a typical vector potential for a static and homogeneous field has been used. A class of functions $\boldsymbol{B}$ for this potential is defined by

$$\phi(\boldsymbol{r}) = \frac{1}{2} \ \boldsymbol{r} \cdot \boldsymbol{R}_g \times \boldsymbol{B}^{ext} \ . \tag{3.60}$$

These functions contain a arbitrary point in space $\boldsymbol{R}_g$. The vector potential $\boldsymbol{A}'$ is given by

$$\boldsymbol{A}'(\boldsymbol{r}) = -\frac{1}{2} \ (\boldsymbol{r} - \boldsymbol{R}_g) \times \boldsymbol{B}^{ext} \ . \tag{3.61}$$

The gauge transformation only changes the origin of the coordinate system as seen by the vector potential. Since the physical field $\boldsymbol{B}^{ext}$ is not affected by this transformation, the *gauge origin* $\boldsymbol{R}_g$ is a cyclic variable, that influences the form of the potential, but not the resulting physics.

In a numerical calculation, instead, the results can depend strongly on the choice of the gauge origin. Several methods have been developed for solving this problem. The *Gauge Including Atomic Orbitals* (GIAO) method [46] chooses the position of each atom as gauge origin for all its orbitals. A second approach, the *Individual Gauges for Localized Orbitals* (IGLO) method [47], uses the center of charge of the molecular orbitals as origin. In the *Continuous Set of Gauge Transformations* (CSGT) method [48], finally, the gauge depends on the location, where the induced

current is calculated. This approach is implemented in the computer code CPMD and is thus used throughout this work.

4 The Path Integral Formalism

4.1 Motivation

Conventional applications of the density functional theory treat all nuclei as classical particles (point charges) without internal structure in the framework of the Born-Oppenheimer approximation. This has been introduced in Sec. 2.1.2. In reality, however, the atoms follow the principles of quantum mechanics, which implies that each particle is best represented by a probability distribution of positions, rather than being restricted to the point of the energetic minimum.

The path integral (PI) technique is an advanced approach to overcome this limitation; it offers a relatively inexpensive way to incorporate this uncertainty in the particle's positions. Adopting a certain number of approximations, it allows the computation of the nuclear density distribution explicitly [49, 50]. Furthermore, the PI formalism in its infinite limit yields the exact quantum mechanical result. The basic principle of this technique was developed by Richard Feynman [51] in 1948 already. He considered it a third formulation of non-relativistic quantum theory, besides the differential equation of Schrödinger and the matrix algebra of Heisenberg. The idea is, that the quantum-mechanical problem is transformed into a statistical problem of a number of classical (but otherwise identical) replicas which are mutually linked. This turned out to be a practical approach for the application in numerical simulations of systems that could not be treated analytically.

The method was employed by Ceperley for the description of condensed helium in combination with Monte Carlo simulation techniques [52]. These techniques have been used for a sampling of the involved integrals over the phase space and they allow accurate simulations without requiring the Born-Oppenheimer separation of electrons and nuclei [53]. However, due to numerical restrictions, most of the

PI applications are still based on model potentials to describe the interactions between the quantum nuclei instead of a pure Coulomb Hamiltonian. Besides Monte Carlo, molecular dynamics simulations have become popular over the past years. In this case, the interactions between the nuclei are directly obtained from electronic structure calculations, i.e. there is no need for an empirical potential. The flipside of the coin is, that the Born-Oppenheimer separation of the wave function is not overcome. Especially the method invented by Car and Parrinello (see Sec. 2.4.3 or [1]) has been used with great success. So, the PI method soon was introduced into the Car-Parrinello molecular dynamics framework. The basic work has been presented by Marx and Parrinello in 1995 [54].

In this chapter, the theoretical underpinnings of PIs are presented, as well as practical methods for the usage of PIs in a molecular dynamics simulation (PIMD). In particular, the *staging transformation* is introduced, which is used in Chapter 5 where PI simulations are combined with the computation of spectroscopic properties.

4.2 Formal Derivation of Path Integrals

The path integral formalism can be developed starting from the canonical partition function

$$Q \equiv Q(N,V,T) = \mathrm{Tr}\ e^{-\beta\mathcal{H}} \ , \tag{4.1}$$

with $\beta = 1/k_B T$. For the evaluation of the trace, a specific basis has to be chosen. A natural choice is the basis of the eigenfunctions of $\mathcal{H}$, but in this case, the coordinate basis is used. In this basis the partition function can be written as

$$Q = \int dR\ \langle R|e^{-\beta\mathcal{H}}|R\rangle \ . \tag{4.2}$$

If the Hamiltonian $\mathcal{H}$ is of the form

$$\mathcal{H} = \frac{\hat{p}^2}{2m} + \hat{\mathcal{U}}(\boldsymbol{R}) \equiv \hat{\mathcal{K}} + \hat{\mathcal{U}} \ , \tag{4.3}$$

where $\boldsymbol{R}$ is the vector of all involved position variables, the operator $\exp(-\beta\mathcal{H})$ cannot be evaluated explicitly, because the operators for kinetic ($\hat{\mathcal{K}}$) and potential ($\hat{\mathcal{U}}$) energies do not commute with each other, i.e.

$$[\hat{\mathcal{K}},\hat{\mathcal{U}}] \neq 0 \ . \tag{4.4}$$

In order to separate the kinetic and potential energies, the *Trotter theorem* can be employed, which states that given two non-commuting operators $\hat{\mathcal{A}}$ and $\hat{\mathcal{B}}$, then for any number λ,

$$e^{\lambda(\hat{\mathcal{A}}+\hat{\mathcal{B}})} = \lim_{P\to\infty}\left[e^{\lambda B/(2P)}e^{\lambda A/P}e^{\lambda B/(2P)}\right]^P \ . \tag{4.5}$$

Applying this to the Boltzmann operator $\exp(-\beta\mathcal{H})$ and inserting the result into Eq. (4.2) yields

$$Q = \lim_{P\to\infty}\int dR\ \langle R|\left[e^{-\beta\hat{\mathcal{U}}/(2P)}e^{-\beta\hat{\mathcal{K}}/P}e^{-\beta\hat{\mathcal{U}}/(2P)}\right]^P|R\rangle \ . \tag{4.6}$$

For simplification, the quantity Ω is defined as

$$\Omega = e^{-\beta\hat{\mathcal{U}}/(2P)}e^{-\beta\hat{\mathcal{K}}/P}e^{-\beta\hat{\mathcal{U}}/(2P)} \ , \tag{4.7}$$

and thus the previous equation becomes

$$Q = \lim_{P\to\infty} \int dR \ \langle R|\Omega^P|R\rangle \ . \tag{4.8}$$

In between each of the P factors of Ω, the coordinate space identity operator

$$\hat{\mathcal{I}} = \int dR|R\rangle\langle R| \tag{4.9}$$

is inserted. Since there are P factors, there will be $P-1$ such insertions. The additional variables will be labeled $R_2, \ldots, R_P$. Thus, the expression for the matrix element becomes

$$\begin{aligned}\langle R|\Omega^P|R\rangle &= \int dR_2 \cdots dR_P \ \langle R|\Omega|R_2\rangle\langle R_2|\Omega|R_3\rangle\langle R_3|\cdots|R_P\rangle\langle R_P|\Omega|R\rangle \\ &= \int dR_2 \cdots dR_P \ \prod_{i=1}^{P} \langle R_i|\Omega|R_{i+1}\rangle\big|_{R_1=R, R_{P+1}=R}\end{aligned} \tag{4.10}$$

The next step is the evaluation of the matrix element

$$\langle R_i|\Omega|R_{i+1}\rangle = \langle R_i|e^{-\beta\hat{\mathcal{U}}/(2P)}e^{-\beta\hat{p}^2/(2mP)}e^{-\beta\hat{\mathcal{U}}/(2P)}|R_{i+1}\rangle \ . \tag{4.11}$$

In the above expression, the operator $\hat{\mathcal{U}} = \hat{\mathcal{U}}(\boldsymbol{R})$ acts on its eigenvectors and can thus be replaced by the corresponding eigenvalues:

$$\langle R_i|\Omega|R_{i+1}\rangle = e^{-\beta(U(R_i)+U(R_{i+1}))/(2P)}\langle R_i|e^{-\beta\hat{p}^2/(2mP)}|R_{i+1}\rangle \ . \tag{4.12}$$

In order to evaluate the remaining matrix element, the momentum space identity operator

$$\hat{\mathcal{I}} = \int dp \ |p\rangle\langle p| \tag{4.13}$$

is introduced. Then the matrix element becomes

$$\begin{aligned}\langle R_i|e^{-\beta\hat{p}^2/(2mP)}|R_{i+1}\rangle &= \int dp \ \langle R_i|p\rangle\langle p|e^{-\beta\hat{p}^2/(2mP)}|R_{i+1}\rangle \\ &= \int dp \ \langle R_i|p\rangle\langle p|R_{i+1}\rangle \ e^{-\beta p^2/(2mP)}\end{aligned} \tag{4.14}$$

Using the fact that

$$\langle R|p\rangle = \frac{1}{\sqrt{2\pi\hbar}}\, e^{ipR/\hbar} \tag{4.15}$$

the integral can be performed, leading to the result

$$\langle R_i|e^{-\beta\hat{p}^2/(2mP)}|R_{i+1}\rangle = \left(\frac{mP}{2\pi\beta\hbar^2}\right)^{1/2} \exp\left(-\frac{mP}{2\beta\hbar^2}(R_{i+1}-R_i)^2\right) . \tag{4.16}$$

Finally, collecting all pieces together, the partition function Q becomes:

$$\begin{aligned} Q = \lim_{P\to\infty} \left(\frac{mP}{2\pi\beta\hbar^2}\right)^{P/2} \int dR_1 \cdots dR_P \cdot \\ \cdot \exp\left[-\beta \sum_{i=1}^{P} \left(\frac{1}{2} m\omega_P^2 (R_{i+1}-R_i)^2 + \frac{1}{P} U(R_i)\right)\right] \Bigg|_{R_{P+1}=R_1} . \end{aligned} \tag{4.17}$$

In the last equation, the frequency

$$\omega_P = \frac{\sqrt{P}}{\beta\hbar} \tag{4.18}$$

has been introduced. Eq. (4.17) is the formal result of this derivation. When expressed in this way, the partition function, for a finite value of P, is isomorphic to a classical configuration integral for a P-particle system, that is a cyclic chain of particles, with harmonic nearst neighbor interactions and an external potential U/P. This will be treated in detail in the next section, where the application to molecular dynamics simulations is explained.

4.3 Path Integrals in MD Simulations

4.3.1 Representation with Ring Polymers

The final result of the last section, Eq. (4.17) can be easily extended to an N-particle system [50]. Then the formula for the partition function reads

$$Q = \lim_{P\to\infty}\left[\prod_{I=1}^{N}\left(\frac{M_I P}{2\pi\beta}\right)^{3P/2}\int d\boldsymbol{R}_I^{(1)}\cdots d\boldsymbol{R}_I^{(P)}\right] \times \exp\left(-\beta\sum_{s=1}^{P}\left\{\sum_{I=1}^{N}\frac{1}{2}M_I\omega_P^2\left(\boldsymbol{R}_I^{(s)}-\boldsymbol{R}_I^{(s+1)}\right)^2+\frac{1}{P}U(\{\boldsymbol{R}_I^{(s)}\})\right\}\right), \tag{4.19}$$

where the path periodicity $\boldsymbol{R}_I^{(P+1)} = \boldsymbol{R}_I^{(1)}$ is assumed. In practice, the limit $P \to \infty$ cannot be taken and the summation has to be truncated at some point. Thus, in the following, a finite P (i.e. number of beads) is used. This, of course introduces an error, which has to be kept small by an appropriate choice of P. The accuracy of this description has been analyzed analytically and will be presented briefly in Sec. 4.3.3. Eq. (4.19) can also be written as "classical phase space integral":

$$Q = \left[\prod_{I=1}^{N}\mathcal{N}\int d\boldsymbol{R}_I^{(1)}\cdots d\boldsymbol{R}_I^{(P)}\int d\boldsymbol{P}_I^{(1)}\cdots d\boldsymbol{P}_I^{(P)}\right] \times \exp\left(-\beta\sum_{s=1}^{P}\left\{\sum_{I=1}^{N}\left\{\frac{P_I^{(s)2}}{2M_I'}+\frac{1}{2}M_I\omega_P^2\left(\boldsymbol{R}_I^{(s)}-\boldsymbol{R}_I^{(s+1)}\right)^2\right\}+\frac{1}{P}U(\{\boldsymbol{R}_I^{(s)}\})\right\}\right), \tag{4.20}$$

where $\mathcal{N}$ is a normalization factor and the M_I' are fictitious bead masses. Since the integrals over momentum are simply a set of uncoupled Gaussian integrals, the two equations are completely equivalent to each other. Eq. 4.20 looks exactly like a phase space integral for a $N \times P$-particle system and so the dynamical equations of motion that generate this ensemble can be constructed. The corresponding Hamiltonian can be obtained from the previous equation:

$$H = \sum_{s=1}^{P}\left\{\sum_{I=1}^{N}\left\{\frac{P_I^{(s)2}}{2M_I'}+\frac{1}{2}M_I\omega_P^2\left(\boldsymbol{R}_I^{(s)}-\boldsymbol{R}_I^{(s+1)}\right)^2\right\}+\frac{1}{P}U(\{\boldsymbol{R}_I^{(s)}\})\right\}. \tag{4.21}$$

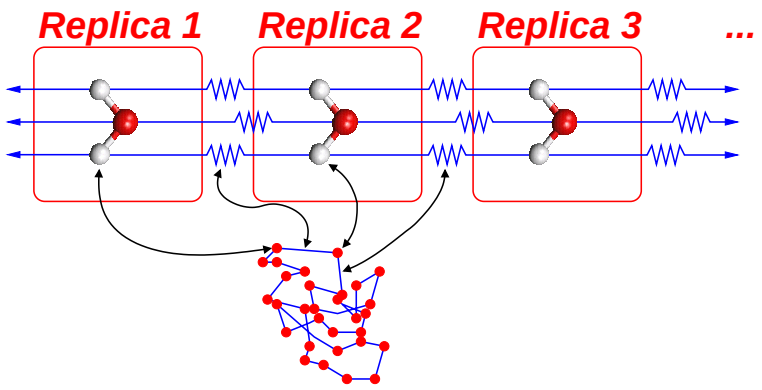

Figure 4.1: Schematic of the principle of the path integral approach, illustrated on a water molecule. The harmonic springs are represented by blue lines.

The new $N \times P$ particle system can be interpreted as follows: The original quantum system is transformed into a P-fold array of corresponding classical systems which are interlinked by harmonic springs. This classical system is isomorphic to the original quantum system, whose quantum-mechanical description is achieved by the thermodynamical sampling of the phase space of the isomorphic classical system. Due to its cyclic topology, caused by the path periodicity, the classical system is often called a "ring polymer" or "ring necklace". An illustration of this transformation is given in Fig. 4.1 for a water molecule. Each physical nucleus is represented by a ring polymer composed of classical particles ("beads"). The beads are connected with harmonic springs, and each bead interacts with all corresponding beads of the other atoms via the physical potential. Each set of corresponding beads is called a replica, as illustrated in Fig. 4.1.

4.3.2 The Staging Transformation

Although a dynamical scheme could be employed simply using the Hamiltonian found in Eq. (4.21), this is not the most efficient method. The difficulty with this straightforward approach is that the more "quantum" a system is, the larger the parameter P must be chosen in order to converge the path integral. However, if P is large, the Hamiltonian describes a system with extremely stiff nearest-neighbor harmonic bonds interacting with a very weak potential U/P. It this therefore almost impossible for the system to deviate far from the harmonic oscillator solutions and explore the entire available phase space. The use of thermostats can

help with the problem, however, it is also exacerbated by the fact that all the harmonic interactions are coupled, leading to a wide variety of time scales associated with the motion of each variable in the Hamiltonian. In order to separate out all these time scales, one must somehow diagonalize this harmonic interaction, i.e. the modes have to be decoupled. There are different approaches to that, as the *normal mode transformation* or the *staging transformation*. In the following the basic ideas of the latter will be described, since it has been used in this work. For detailed information about both transformations, we refer to the work of Tuckerman et al. [50]. The staging transformation received its name because of its link to the staging Monte Carlo method [55].

For each nuclear degree of freedom, a set of variables $\{\boldsymbol{u}_I\}^{(s)}$ is defined by

$$\begin{aligned} \boldsymbol{u}_I^{(1)} &= \boldsymbol{R}_I^{(1)} \ , \\ \boldsymbol{u}_I^{(s)} &= \boldsymbol{R}_I^{(s)} - \boldsymbol{R}_I^{(s)*} \ , \quad s = 2, \ldots, P \ , \end{aligned} \tag{4.22}$$

where

$$\boldsymbol{R}_I^{(s)*} = \frac{(s-1)\boldsymbol{R}_I^{(s+1)} + \boldsymbol{R}_I^{(1)}}{s} \ . \tag{4.23}$$

The inverse of this transformation is given by

$$\begin{aligned} \boldsymbol{R}_I^{(1)} &= \boldsymbol{u}_I^{(1)} \ , \\ \boldsymbol{R}_I^{(s)} &= \boldsymbol{u}_I^{(1)} + \sum_{t=s}^{P} \frac{s-1}{t-1} \boldsymbol{u}_I^{(t)} \ , \quad s = 2, \ldots, P \ . \end{aligned} \tag{4.24}$$

When the new variables are substituted into Eq. (4.20), the resulting expression for the partition function becomes

$$\begin{aligned} Z = &\left[\prod_{I=1}^{N} \mathcal{N}' \int d\boldsymbol{u}_I^{(1)} \cdots d\boldsymbol{u}_I^{(P)} \int d\boldsymbol{P}_I^{(1)} \cdots d\boldsymbol{P}_I^{(P)} \right] \\ &\times \exp\left(-\beta \sum_{s=1}^{P} \left\{ \sum_{I=1}^{N} \left\{ \frac{(P_I^{(s)})^2}{2M_I'^{(s)}} + \frac{1}{2} M_I^{(s)} \omega_P^2 \left(\boldsymbol{u}_I^{(s)} \right)^2 \right\} + \frac{1}{P} U(\{\boldsymbol{R}_I^{(s)}\}) \right\} \right) \ , \end{aligned} \tag{4.25}$$

where the masses $M_I^{(s)}$ replacing the physical masses M_I, referred to as staging

masses, are given by

$$M_I^{(1)} = M_I \ ,$$
$$M_I^{(s)} = \frac{s}{s-1} M_I \ , \quad s = 2, \ldots, P \ . \tag{4.26}$$

The fictitious masses $M_I'^{(s)}$ are assumed to be a constant multiple of the staging masses, i.e. $M_I'^{(s)} = cM_I^{(s)}$. It should be noted, that the $\boldsymbol{R}_I$ in the potential energy U are functions of the new variables $\boldsymbol{u}_I$. With the help of this transformation, the harmonic oscillators are now completely decoupled from each other. Therefore, it is possible to isolate the time scales associated with the different modes and choose the fictitious bead masses such that all modes move on the same time scale. Still, all degrees of freedom have to be coupled to thermostats to assure the desired generation of the corresponding ensemble. Using this method, a much faster convergence of the path integrals is expected, leading to an effective sampling of the whole phase space.

4.3.3 Finite-Discretization Errors

For a practical PI molecular dynamics simulation, the number of beads P has to be set to a finite value. In Sec. 4.3.1 it has been shown, that the effective system, that is subject to the calculation, is a $N \times P$-particle system. This means, that the computational effort increases at least linearly with the number of beads. Since molecular systems of experimental interest in most cases already contain a large number of atoms, P is usually rather small. Typical values are 16 or 32, which have also be used in this work. The error introduced by the truncation of the Trotter formula is a systematic one, but each simulation also suffers from statistical errors due to the incomplete sampling of the phase space. Therefore, it is not possible to estimate the finite-discretization error by just calculating the same quantity for various values of P. Knoll and Marx presented an analytical investigation of this systematic errors, that can give a rough error assessment [56]. Although the model used there is not sufficient for more complicated compounds, it yields a good indication of the errors that can be expected.

The parameter observed in the cited work is the width σ of a particle with respect to its equilibrium position, which corresponds to a "0 Kelvin and no quantum effects" value. On the potential energy surface, this position is given by the point of minimal energy. The width can be compared to the spatial spread that is introduced in Sec. 5.2. It is given by

$$R_I = \sqrt{\frac{1}{P}\sum_{s=1}^{P} |\boldsymbol{R}_I^c - \boldsymbol{R}_I^{(s)}|^2} \,, \tag{4.27}$$

where $\boldsymbol{R}_I^{(s)}$ is the position of the respective atom in bead s, $\boldsymbol{R}_I^c$ is the centroid, i.e. the position averaged over all beads. If the potential is assumed to be harmonic close to the minimum, a formula can be found for the error of the width with respect to P. It is given by

$$\frac{\sigma_\infty - \sigma_P}{\sigma_\infty} \approx \left(\frac{\omega\beta}{4P}\right)^2 \,, \tag{4.28}$$

where σ_P and σ_∞ are the widths with P and infinite beads, respectively, $\beta = 1/k_B T$ and ω is the corresponding vibrational frequency of the observed eigenmode. This gives a very handy estimate, if the mentioned frequency is known. If not the vibrational frequency, but the ground state energy E_0 can be obtained, the estimate reads

$$\frac{\sigma_\infty - \sigma_P}{\sigma_\infty} \approx \left(\frac{E_0\beta}{2P}\right)^2 \,. \tag{4.29}$$

Finally, the authors compare the results from these estimates to benchmark calculations. These have been done for HD^+ and H_3^+, where experimental and very accurate computational values are known. For these benchmarks a good agreement of the formula with the calculated error has been found. Furthermore, for $P = 16$ the relative error is below 10%, rapidly decreasing with increasing P. As mentioned above, the harmonic approximation can hardly be applied to more complicated systems. Still, it gives an estimate for the error and the numbers of beads, that have been chosen in this work, i.e. 16 or 32, seem to be justified, since the statistical error can be expected to be within the same range.

5 Nuclear Quantum Effects in Molecular Systems

5.1 Motivation

In the past decades ab-initio molecular dynamics simulations have become a powerful tool for exploring the structure and properties of matter. The growing capabilities of modern computers open the way for experimentally relevant supramolecular systems. Dynamics simulations can be carried out on a timescale that is needed for motional effects, i.e. temperature dependence of spectroscopic properties. Still, there are certain phenomena that cannot be explored by conventional molecular dynamics simulations, because the underlying physical effects are not included in the computational techniques used. As described in Sec. 2.1.2, the Born-Oppenheimer approximation is usually employed in combination with the assumption that the nuclei can be treated as classical point-particles. These are propagated in the potential that is created by the surrounding electrons, which are represented by their quantum mechanical probability density, based on the Schrödinger equation.

In contrast to this approach, in chemical physics there is a wealth of problems where quantum effects on the nuclei are crucial. Proton tunneling is known to be of importance for phase transitions between various phases of ice especially in the high pressure/low temperature part of the phase diagram. Furthermore, many small clusters and few-atom molecules have low isomerization barriers. In these cases tunneling between different structures might significantly influence their properties.

It has been shown recently, that motional effects can lead to a notable effect on spectroscopic properties [30], such as nuclear quadrupole coupling constants (NQCC). Since the quantum mechanical treatment of particles generally leads to an even broader distribution in space, e.g. due to zero-point vibrations, it can be

expected that there are also significant effects due to the quantum nature of the nuclei. This can be estimated by an inspection of the potential energy surface (PES) of the system, based on an expansion of the PES at the position of the nucleus and consideration of harmonic and anharmonic vibrational contributions [57, 58, 59]. In the cited work, highly correlated methods have been used, in principle leading to a high accuracy. Still, the observables are expanded in a Taylor series up to a certain order. Such a truncation always introduces errors, although they can be kept under control if the system is inspected diligently. The path integral formalism includes quantum effects in a natural way and does not require such an expansion. In turn, it is much more computationally demanding and there are other numerical errors that have to be discussed (see Sec. 4.3.3). This approach enables the straightforward treatment of both motional and quantum effects in an ab-initio framework.

In Chapter 4 the formal description and the usage of path integrals in a molecular dynamics code has been described. The *staging transformation* has been introduced in Sec. 4.3.2. The practical use of path integrals showed, that the equations of motions as derived in Sec. 4.3.1 lead to a very slow equilibration of the simulated systems. The staging transformation improves the convergence significantly. This will be demonstrated with a small test-system.

Subsequently, several systems will be investigated using the path integral formalism. The effect of nuclear quantum effects on both NQCCs and NMR chemical shifts will be explored. It should be noted, that in the theoretical sections, the term *proton* and *deuteron* are used synonymously, since the mass of the nucleus does not influence the result from the calculation of spectroscopic properties. Yet this distinction becomes relevant in the experiment, e.g. protons do not exhibit any quadrupole interactions. This will emphasized again, where necessary. However, for the molecular dynamics simulations, the mass is important and will thus be mentioned in the respective technical details.

5.2 Staging Transformation and Spectroscopic Properties

The effect of the staging transformation on the convergence with respect to structural properties, as the spread of the quantum particles, has already been tested [50]. It is clear that this technique is necessary if one is interested in such parameters. Still, it is not clear if this also holds for spectroscopic properties, as NQCCs or NMR chemical shifts.

NQCCs, which only require the knowledge of the electric field gradients at the position of the nucleus (see Sec. 3.2.1), are ground state properties and can be easily computed during an MD, or even path integral MD (PIMD). The calculation of NMR chemical shifts, instead, involves a lengthy linear response calculation (see Sec. 3.3.2). Therefore, in this section the effect of staging or not staging on the NQCC of a simple model system is examined.

The test system is a single water molecule. It can be considered isolated, because it has been put in a supercell of 5 Å box length. Periodic boundary conditions have been employed, as is common when using the program package CPMD [20]. It is unclear, whether the periodic images affect each other, but since the calculation with and without staging transformation have used the same settings, the periodic boundary conditions will not influence the results. In both cases, the BLYP functional have been applied, in combination with the norm-conserving pseudopotentials of Goedecker and co-workers (GTH) [18]. The wavefunction cutoff was 80 Ry and the Trotter dimension, i.e. number of beads, 8. The MD was carried out in the NVT ensemble, using Nosé-Hoover-thermostats with a characteristic frequency of 2500 cm^{-1} and temperature of 50 K, the time step was 4 a.u. For the hydrogens, the proton mass was used.

The simulation with staging transformation has been run up to 5 ps, the simulation without staging up to 10 ps. The starting geometry was an isolated water molecule in optimized geometry. In the first step the beads have to be initialized, i.e. an initial guess for the distribution of the replica in the space has to be made. This is done using an interpolation formula for a conditional Brownian motion path at 500 K [60].

The centroid of the PIMD is the average position of all representations of a certain atom, i.e. an average over all beads. It is defined by

$$\boldsymbol{R}_I^c = \frac{1}{P}\sum_{s=1}^{P}\boldsymbol{R}_I^{(s)} \ . \tag{5.1}$$

The first property that is looked at for judging the quality of the PIMD is the average distance of the beads from their centroid. This spatial spread is given by

$$R_I = \sqrt{\frac{1}{P}\sum_{s=1}^{P}|\boldsymbol{R}_I^c - \boldsymbol{R}_I^{(s)}|^2} \ . \tag{5.2}$$

The spread R_I for the two hydrogen atoms, denoted by A and B, respectively, obtained from the two simulations is shown in Fig. 5.1. Only the hydrogens are considered here and in the following, because the desired properties will also be calculated only for these atoms. It can be seen that with the staging transformation (lower panel) the spread is basically converged after 2-3 ps, showing only small fluctuations in the subsequent run. Also, the final spread of about 0.35 Å is reached shortly after the beginning, within 1 ps. The run without the transformation (upper panel) does not show this nice convergence behavior. Here, the spread does not increase as fast as in the former case and, additionally, the fluctuations are much larger. Although the slope of the curves indicate that the final value will be close to 0.35 Å as seen before with staging, this is not even reached after 10 ps. Thus, the convergence of the spatial spread, which will be very important for the sampling of spectroscopic properties, is the first sign that staging is necessary for a good PIMD run.

Secondly, the "quantum energy" can be considered. "Quantum energy" in this case is the sum of the Kohn-Sham electronic energy and the energy arising from the harmonic potential between the beads. Its cumulative average is displayed in Fig. 5.2. The instantaneous values have to fluctuate, but the average should rapidly converge. Again, in the staging run it converges after 2 ps, whereas in the non-staging case convergence is not achieved even after 10 ps. It is obvious that equipartitioning is reached much faster if the transformation is applied, leading to a much better sampling of the available phase space. These two quantities, the

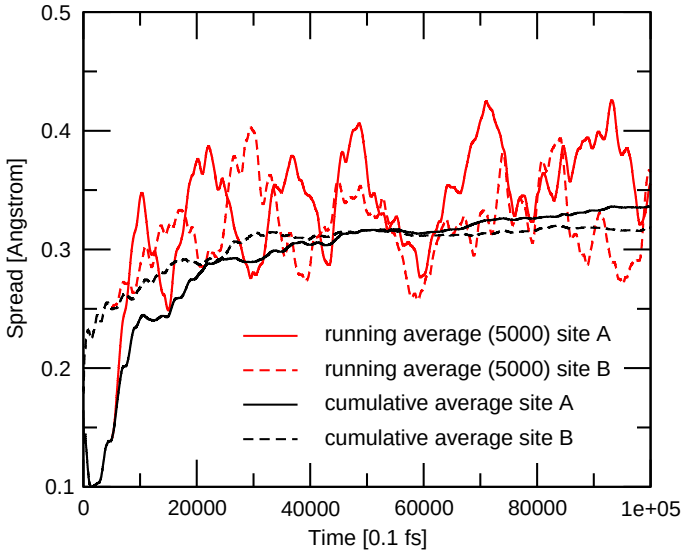

(a) no transformation

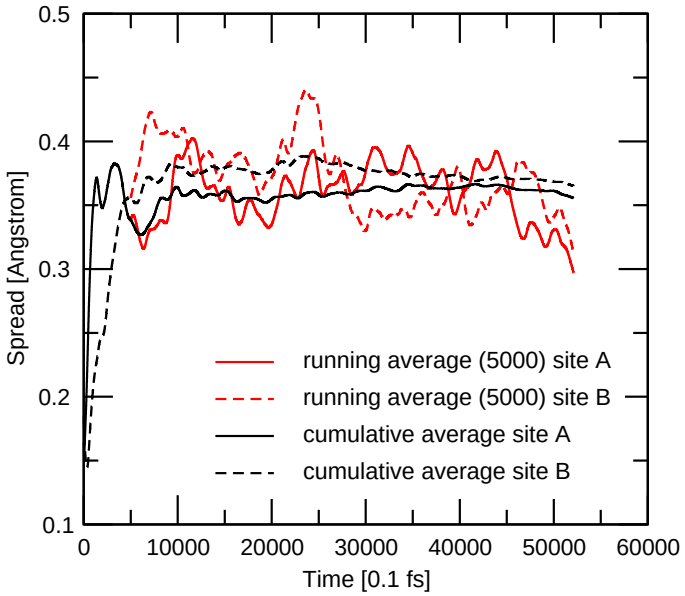

(b) staging transformation

Figure 5.1: Spatial spread of the protons (site A/B) of an isolated water molecule. The red lines are a cumulative average over the last 5000 steps, the black lines average over the whole run.

energy and the spatial spread, indicate that for a nicely converged path integral run the staging transformation is crucial. It can be expected that spectroscopic properties derived from theses simulations, are much more reliable if the staging transformation is used. Additionally, the necessary equilibration prior to the actual production run can be much shorter.

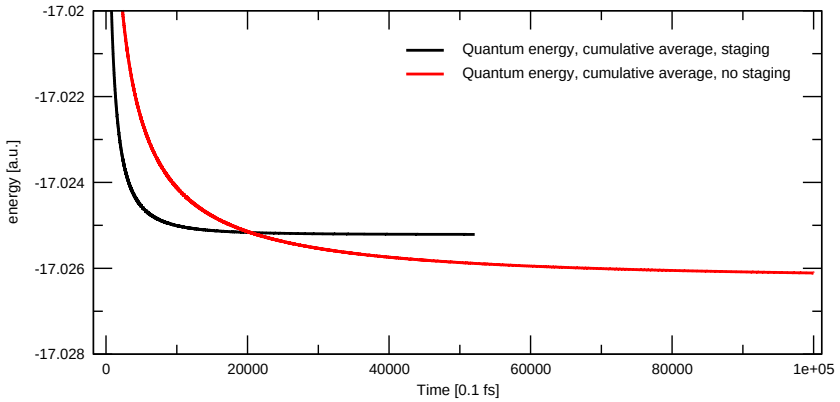

Figure 5.2: Quantum energy (see text) of the water molecule from two different simulations. The red line is the simulation without transformation, the black line represents the calculation with staging transformation.

Finally, the above-mentioned deuteron NQCCs have been calculated during both runs and the results are shown in Fig. 5.3. Both running averages over the last 1000 steps and the cumulative average are shown. It should be noted, that in this case the instantaneous NQCCs have been averaged, whereas in a simulation that is supposed to reproduce the experimental coupling, the electric field gradient tensor has to be averaged. However, only the convergence due to the distribution of the beads is of interest here, and thus the effect of averaging the tensor with respect to the orientation in space was neglected. The fluctuations of the running average is similar in both cases, but the cumulative average again reveals the different behavior of the two systems. With the staging transformation the NQCC for site A and B varies rapidly in the beginning, then it stays close to its final value. After approximately 3 ps the parameters for the two sites are very close to each other, they are only fluctuating around the final result. This can be expected for an isolated water molecule, since only the fast vibrations of the hydrogens affect the NQCC, whereas the orientation in space has not been taken into account, as mentioned above. In the lower right corner of the graph the final averaged values

for the two hydrogens are given, showing that both behave very similarly in the staging-case (167.0 kHz vs. 167.5 kHz), but exhibit larger differences (169.8 kHz vs. 173.4 kHz) without staging, although the non-staging simulation has been run twice as long. Additionally, if the transformation is not applied, the convergence is much slower. Both hydrogens' NQCC stay very close to each other during the entire run, without actually reaching a plateau, indicating equipartitioning is not achieved.

In conclusion, one can say that the usage of the staging transformation is crucial for a fast convergence of the PIMD and absolutely necessary for a decent sampling of the phase space. Although staging has been used throughout this work, other transformations, as mentioned above, could have been employed, most likely yielding similar results. The straightforward approach using the spatial variables of the nuclei is not recommended, since the convergence of all the considered parameters is very slow.

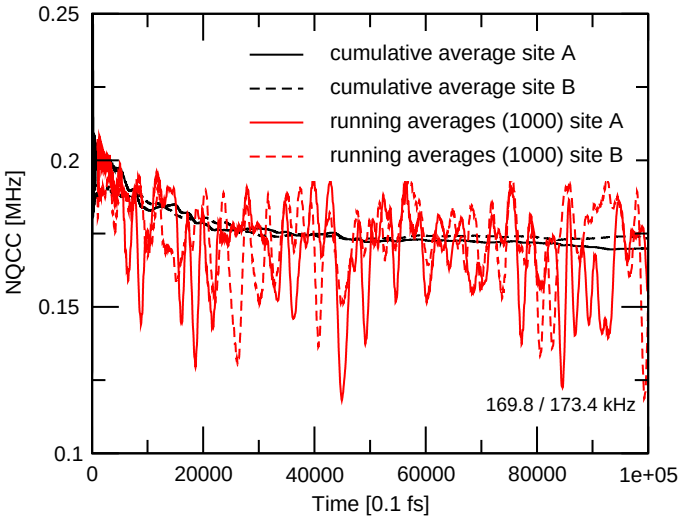

(a) no transformation

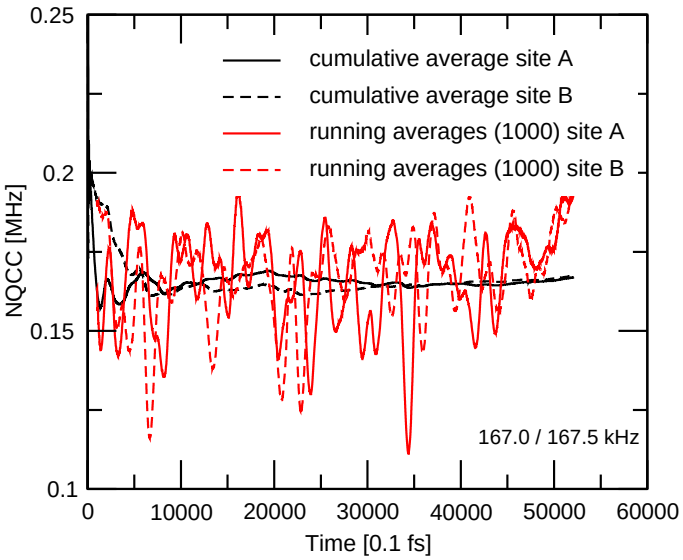

(b) staging transformation

Figure 5.3: Nuclear Quadrupole Coupling Constants in an isolated water molecule. Site A/B are the two different protons. The values given in the lower right corner are the averaged values for the two protons at the end of the simulation.

5.3 Tunneling Effects in Acetylacetone

5.3.1 Introduction

The path integral formalism has been used for various applications, embedded in different frameworks, such as molecular dynamics or Monte Carlo schemes. In many cases, the influence of the quantum nature of the nuclei on structural properties or the dynamics of the system has been investigated [54, 61, 52]. Yet the combination of path integral methods and the calculation of spectroscopic properties is not documented in literature, except for a very approximate scheme [62]. This is probably because both PIMD and linear response calculations, which are often necessary for spectroscopic parameters, are very time consuming. The rapidly growing performance of modern computers have enabled such an approach and in this and the following chapters first results are presented.

The first application will be a rather small system which allows for an efficient sampling within a feasible time frame. Additionally, the desired quantum effects are expected to appear prominently in this case. The chosen system is acetylacetone (ACAC), it is shown in Fig. 5.4. It exists in two tautomeric configurations, the keto and the enol form. Only the enol form is of interest in this study, because it contains a very short, intramolecular hydrogen bond (O-O distance approx. 2.6 Å) that gives rise to proton tunneling. It has been shown by NMR experiments, that the equilibrium is on the side of the enol (81%) [63]. Burdett and Rogers found an NMR chemical shift of 15.6 ppm for the hydrogen bonded proton. This very high value corresponds to the short bond, but might also be due to tunneling. Besides this, an investigation of the infrared spectrum of ACAC has revealed some evidence for tunneling of the protons [64]. Furthermore, the authors reported, that tunneling is not, or almost not, possible if a deuteron is present, resulting in a significant isotope effect.

In the following, the structure and NMR parameters of ACAC are investigated in a series of simulations. In this work, the comparison between the tunneling and non-tunneling system is not made by substituting the proton by a deuteron, but rather by simulating in one case using path integrals, and in another case without any incorporation of nuclear quantum effects. The latter will be referred to as "classical". This term does not mean that classical force fields or similar tech-

niques are used, but rather that the nuclei are treated as classical point particles in the common ab-initio framework. The choice for the two approaches might increase the difference between the protonated and the deuterated systems, but the aim of the project was to show that quantum effects on spectroscopic properties can be calculated at all.

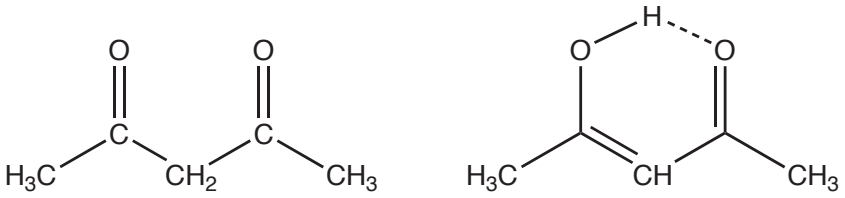

(a) keto form (b) enol form

Figure 5.4: Acetylacetone in its keto and enol form. NMR measurements reveal that the equilibrium is on the side of the enol form ($\sim$ 80%).

5.3.2 Proton Density from a Path Integral Simulation

Two simulations have been performed for the investigation of quantum effects in ACAC. As mentioned in the above section, there is a "classical" run and a second one, using the path integral formalism. Both employed the quantum chemical code CPMD [20]. The exchange-correlation functional was BLYP, norm-conserving pseudopotentials of the Goedecker-type have been applied. The wavefunction cutoff was 100 Ry. This is a bit higher than the usual cutoff, but during the MD, the electric field gradients have been computed, which require a higher cutoff [30]. The PIMD used 16 beads. The MD was carried out in the NVT ensemble, using Nosé-Hoover-thermostats with a characteristic frequency of 2500 cm^{-1} and temperature of 300 K, the time step was 4 a.u., the proton mass has been used for the hydrogen nuclei. The simulation with path integrals has been run up to 5 ps, the classical simulation up to 6 ps. The staging transformation has been employed during the whole run to converge the PIMD simulation. The initial distribution of the beads was generated with a conditional Browian motion path at 500 K [60]. The ACAC molecule was put into a large box of 10x9x7 Å, for simulating an isolated system. Although the crystal structure would have been available, the influence of collective effects, or electrostatic perturbations by neighboring

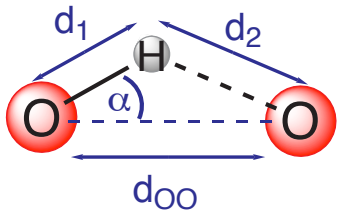

Figure 5.5: Sketch of the parameters α and $\delta = (d_1 - d_2)/d_{OO}$, which are used in the following figures. The drawn atoms are representing the H-bond of the considered molecule.

molecules were excluded by this approach. This was done for exploring the pure effect of the proton tunneling.

Since this is only a very small system, the temperature is fluctuating a lot during the simulation, after 50-100 fs the distribution reached a stationary point and so only the first 500 steps were left out of the following analysis of the structure. Still, it was checked explicitly, that the reported results would not be changed qualitatively if only the end of the run was considered.

Before looking at spectroscopic properties, the structure of the molecule based on the simulations will be investigated. The motional behavior of the proton in the hydrogen bond should be affected by the quantum effects. In the classical case, i.e. without nuclear quantum effects, the proton is restricted to one side of the bond, it cannot tunnel through the energy barrier between the two minima of the potential energy surface. In the quantum case, instead, the proton will change from one side to the other, if tunneling is present. Additionally, in this case we expect a non-zero proton density even at the barrier. Two parameters will be shown in detail, both explained in Fig. 5.5. These are the angle α, representing the deviation of the proton from the straight line between the oxygens, and the parameter δ, measuring the difference between the distances of the proton from the two oxygens, normalized to the oxygen-oxygen distance. This means that we do not expect any proton density at $\delta = 0$ in the classical case. It should be noted here, that the term "proton density" is used for the statistical distribution of the proton over the whole MD, i.e. in each step all corresponding distances are collected and in the end a histogram is made out of these, representing the density of the proton with respect to δ or α. In Fig. 5.6 the relative occurrence of the parameter δ is shown. At first sight, the statistics in the classical case seem

to be much worse, although the total simulation time is similar. This is due to the fact, that each time step of the PIMD run contains 16 representations of the respective proton, indeed leading to much more data. In the classical case, the value $\delta = 0$ does almost not occur, as expected. Still, the probability is not zero. Also, the proton seems to appear in both minima, although only a single molecule has been simulated. This is due to the fact that at 300 K the kinetic energy of the proton is sufficient to occasionally jump over the barrier and go to the other minimum, which can happen in a simulation of such a strong hydrogen bond, since the barrier is not very high. Also, the non-zero value at $\delta = 0$ can be explained by this argument. The energy that is necessary for overcoming the barrier can be estimated by comparing the energy of the optimized geometry and the transition state with a symmetrical hydrogen bond, which yields $\Delta E \approx 0.9$ kcal/mol. This value reflects the fact that the hydrogen bond is very short and thus the barrier relatively low. Still, it should be noted that it is known that activation energies, especially in hydrogen bonds, are in general underestimated in DFT. Using this ΔE, the fraction of hydrogens that are able to jump over the barrier can be estimated from a Boltzmann distribution. It amounts to approximately 5% at 300 K. This means, that even in the classical case, using just classical statistical mechanics, the energy barrier should be crossed from time to time, as it happened during the simulation.

In the quantum case the probability of finding the proton at the barrier is much higher than in the classical case. Fig. 5.6 displays the expected behavior, i.e. tunneling between the two minima with a finite proton density for the symmetrical case.

While the parameter δ reveals a pronounced influence by the quantum nature of the nuclei, the angle α, shown in Fig. 5.7, seems not to be affected significantly. Again, statistics are better in the quantum case, but the maximum and the width of the distribution are almost unchanged. Only the width might be larger in the path integral case, but this can also be due to statistics. In both cases, the maximum appears at α=10°, leading to a structure similar to Fig. 5.4.

The structural parameters show, that the short hydrogen bond leads to tunneling of the proton if the quantum nature of the nuclei are incorporated. This leads to a

very broad distribution of the bond lengths. However, the bending motion of the bonded proton is not affected significantly. In the next sections the consequences for NMR parameters, i.e. the chemical shift and the NQCC, will be presented.

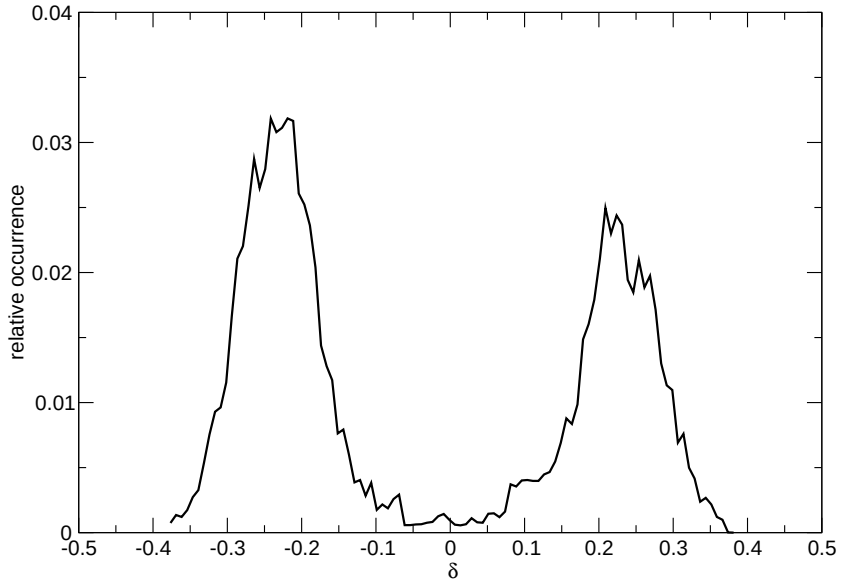

(a) Classic Simulation

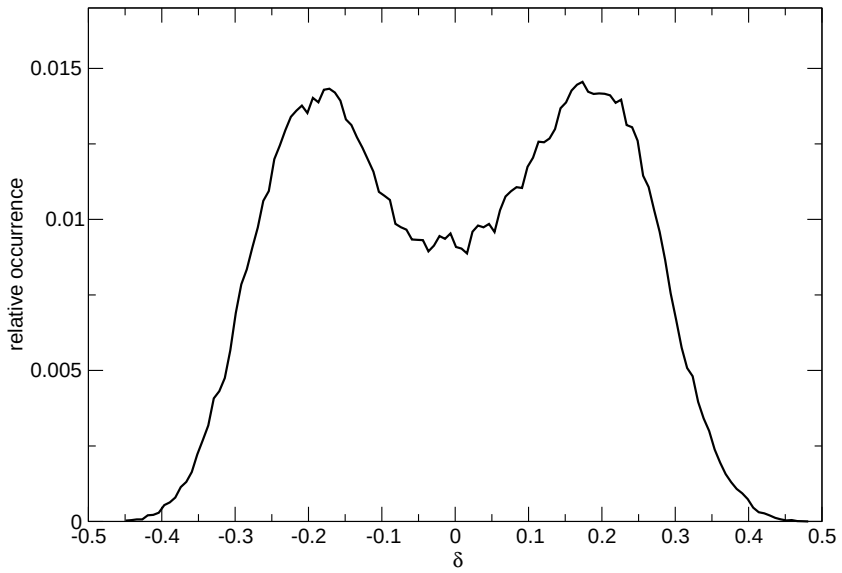

(b) Path Integral Simulation

Figure 5.6: Distribution of the distance parameter δ from a classical (5.6(a)) and a path integral (5.6(b)) simulation. The parameter δ is explained in Fig. 5.5.

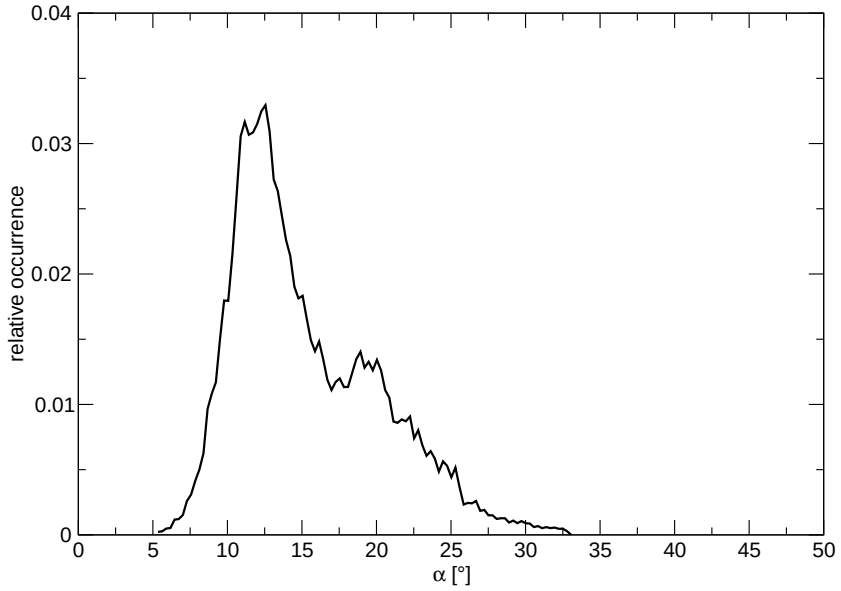

(a) Classic Simulation

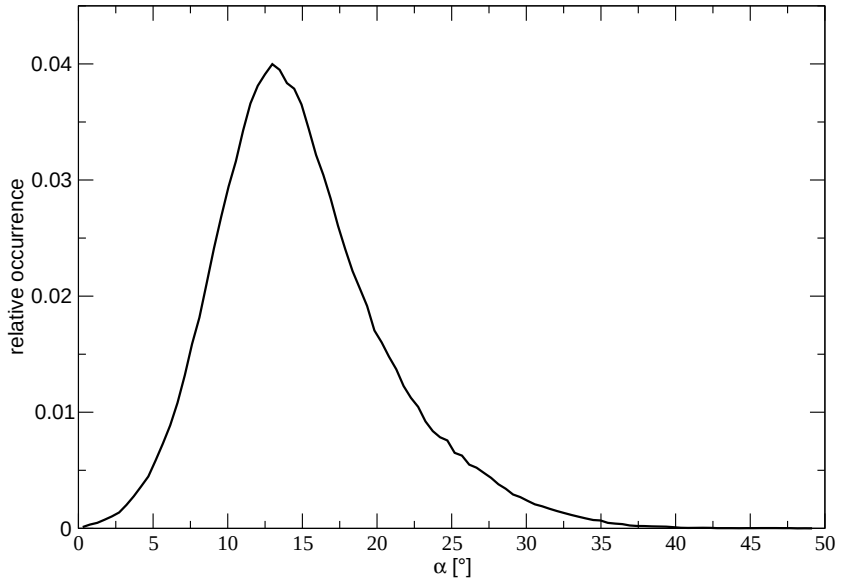

(b) Path Integral Simulation

Figure 5.7: Distribution of the angle α from a classical (5.7(a)) and a path integral (5.7(b)) simulation. The angle α is shown in Fig. 5.5.

5.3.3 Electric Field Gradients: Classic vs. Quantum MD

In the previous section it has been shown that dynamical parameters, as the bond length distribution, are significantly affected by nuclear quantum effects. In this section, the influence on the nuclear quadrupole coupling constant (NQCC) will be explored. The electric field gradient, that is directly proportional to the NQCC, has been calculated as described in Sec. 3.2.1 (or [30]) during the MD runs. As in the case of the test system for the staging transformation, instantaneous NQCCs will be considered, i.e. the tensors are not averaged. Instead, the instantaneous eigenvalues are averaged, which means that rotational effects of the molecule are excluded. As before, this procedure is applied, because only effects due to the quantum nature of the nucleus are taken into account, but not dynamical effects of the whole molecule. The simulation has been done for an isolated molecule, the dynamics of the whole system is not meaningful, since interactions with the environment have been neglected. Thus, the change of the quadruple interaction will be only due to the altered distribution of the structural parameters α and δ (see Fig. 5.5).

In Fig. 5.8 the NQCC for the hydrogen bonded atom is shown, both from the classical and the path integral MD. As stated before, the running average of the instantaneous values is displayed. It can be seen that in both cases the convergence of the parameter is reached after approximately 2.5 ps, the classical run at 100 kHz, the PIMD at 69 kHz. No error is given, because it can hardly be estimated in an analytical way. Convergence can be estimated to be reached within 5 kHz, errors arising from the wavefunction cutoff and systematic errors are considered to be in the same range [65]. First, it can be stated, that there is a significant influence on the NQCC, the difference is about 30%, which, for sure, cannot be considered a minor effect. In general, it can be easily understood that the more symmetric the system, the smaller the resulting electric field gradient is. Therefore, it is not surprising, that in the quantum case the NQCC is smaller, since, as shown before, the distribution of the proton is non-zero in the middle of the hydrogen bond (see Fig. 5.6), or, in the language of Sec. 5.3.2, the relative occurrence of $\delta = 0$ is much higher. This, in turn, results in the average in a higher symmetry, leading to a smaller NQCC.

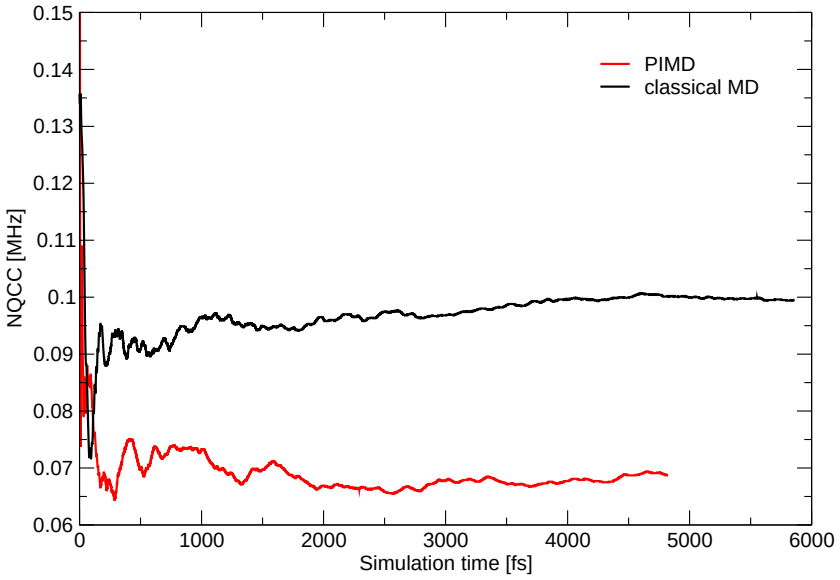

Figure 5.8: Cumulative averages of the NQCC from an MD at 300 K. The black line shows a simulation within the classical approximation, whereas the red line is taken from a path integral simulation.

The asymmetry parameter, η, reveals a different picture. Here, one might be tempted to expect that a more symmetrical system leads to a smaller asymmetry. Fig. 5.9 shows that this is not the case. Instead, the asymmetry is considerably higher in the quantum case, namely 0.38, whereas 0.26 is found in the classical simulation. The reason for this can be understood if one looks at two special configurations. On the one hand, the relaxed structure with the proton in one of the minima, on the other hand the transition state, where the proton is exactly half-way between the oxygens. These structures are shown in Fig. 5.10, together with the respective electric field gradients, i.e. the three normalized eigenvectors. The relaxed geometry (Fig. 5.10(a)) will be referred to as the asymmetrical case, the transition state (Fig. 5.10(b)) as the symmetrical one. The corresponding eigenvalues are (in atomic units):

$$\phi_{33}^{symm} = -0.0342\ , \qquad \phi_{11}^{symm} = \ 0.0304\ , \qquad \phi_{22}^{symm} = \ \ 0.0039\ ,$$

$$\phi_{33}^{asym} = \ \ 0.4356\ , \qquad \phi_{11}^{asym} = -0.2417\ , \qquad \phi_{22}^{asym} = -0.1939\ ,$$

where the convention $|\phi_{33}| \geq |\phi_{11}| \geq |\phi_{22}|$ (see Sec. 3.2.1) has been used. Obviously, the eigenvalues corresponding to the eigenvectors that are perpendicular to

the axis of the hydrogen bond are similar in both cases. They are not affected much by the fact that the molecule is much more symmetrical in the transition state. The eigenvalue of the eigenvector in the direction of the bonding axis is large in the asymmetrical case, actually the largest of all three, but, as mentioned above, very small in the symmetrical case. The asymmetry parameter is mainly defined by the difference between the second smallest and smallest eigenvalue, which leads to almost maximum asymmetry in the symmetrical case, as one of the eigenvalues nearly vanishes.

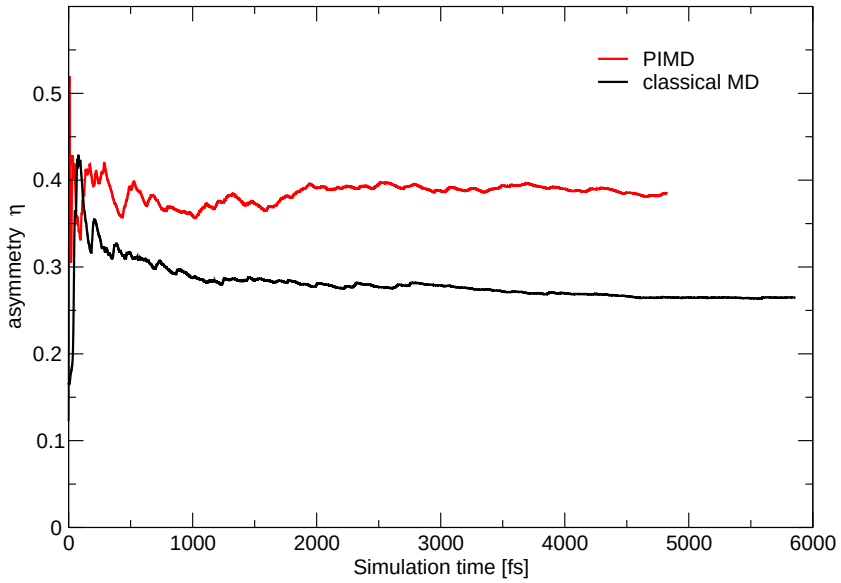

Figure 5.9: Cumulative averages of the asymmetry parameter η from an MD at 300 K. The black line shows a simulation within the classical approximation, whereas the red line is taken from a path integral simulation.

Nuclear quantum effects are important in ACAC for the NQCC, since the "chemically" symmetrical structure, where the hydrogen bonded proton is situated in the middle between the oxygens exhibits a special highly asymmetric electric field gradient tensor. Thus, the averaged NQCC parameters change significantly if this structure is more likely than in the classical case, which happens, if nuclear tunneling is taken into account. Again, it should be emphasized, that the obtained NQCCs cannot be compared to the experiment directly, since in the experimental case an effective, averaged, electric field gradient would be measured, whereas the instantaneous eigenvalues have been used here for averaging. The nuclear quantum effects could be isolated like this. The next step, however, is the investigation

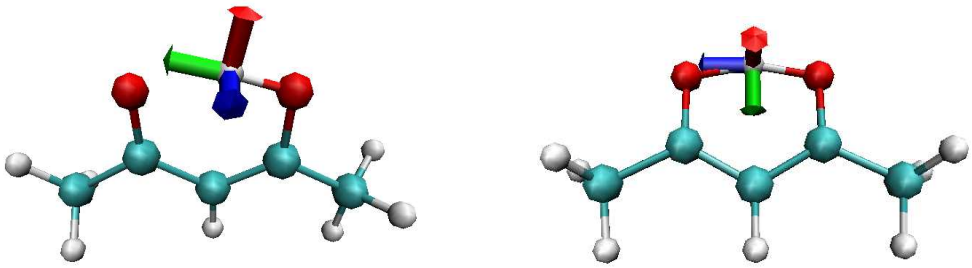

(a) optimized geometry (b) transition state

Figure 5.10: Electric field gradient tensor in the optimized geometry and the transition state of acetylacetone. Colors denote the ordering of the absolute values of the corresponding eigenvalues: |green| ≥ |red| ≥ |blue|.

of crystalline ACAC. In that case, both NQCC and NMR chemical shift are easily accessible in the experiment. From the theoretical point of view, the crystalline system is more difficult, because it involves all kinds of collective and long-ranged effects, that have been excluded here. Thus, ACAC in the solid state is beyond the scope of this work, where the fundamental influence of quantum effects has been aimed for.

5.3.4 NMR: Classical vs. Quantum MD

It has been shown (see previous sections), that the quantum nature of the hydrogen bonded proton in ACAC affects both structure and NQCC parameters. Unfortunately, there has not been experimental evidence for these findings. In this section, the NMR chemical shift in the classical case will be compared to the one from the path integral simulation. In this case, a direct comparison to the experiment is applicable and will be presented. In contrast to the NQCC, the NMR chemical shift is obtainable for both protons and deuterons. Therefore, the isotope effect, i.e. the difference between the protonated and the deuterated system, can be measured in an NMR experiment. While the isotope effects on the NQCC can only be assessed theoretically in the simulation, because the proton does not exhibit a static quadrupole moment, the chemical shift can be measured for both the protonated and the deuterated sample, allowing a direct comparison to the experiment [66].

The NMR chemical shift of ACAC in the enol form has been measured by Burdett

and Rogers in 1964 [63] and the hydrogen bonded proton was found at 15.6 ppm, which is exceptionally high and thus already indicated that some unusual effect might be occuring. Here, measurements that have been done at our institute, especially for this work, will be used for comparing the quantum effects on the chemical shift to the simulations.

The NMR chemical shift cannot be obtained as easily as the NQCC during the MD. Its calculation requires a linear response run and has to be conducted separately (see Sec. 3.3.2). In the classical case, this has been done for 100 snapshots from the MD, in the quantum case for 50, where it should be noted that each snapshot in the path integral case contains 16 beads, resulting in 16 individual calculations. In the quantum case, the first 100 fs of the MD have been excluded, in the classical simulation the first 500 fs. The snapshots were chosen randomly to avoid the overemphasis of certain vibrational modes, which can happen if all frames are equally distant from each other. The wavefunction cutoff was 60 Ry. All NMR calculations have been averaged at the end to obtain the final spectrum.

Fig. 5.11 shows the convergence of the nuclear magnetic shielding of the hydrogen bonded proton with respect to the number of calculated snapshots. In both cases the chemical shift is expected to be converged within 0.3 ppm. This is also the assumed error of this calculation, since again an analytical measure for the error cannot be given. The convergence of the remaining protons has been checked explicitly and exhibits similar curves.

Having assured the convergence, the actual NMR chemical shift spectrum can be calculated from the shieldings. It is shown for both cases in Fig. 5.12. The spectrum contains three peaks corresponding to the three different types of protons in the enol form of ACAC. The methyl groups appear at the lowest value, 2.1 ppm, the remaining olefinic proton has a shift of 4.9 ppm. The hydrogen bonded proton shows up at 15.3 ppm in the classical and at 16.8 ppm in the quantum case, again revealing a pronounced quantum effect. Since the calculations of the chemical shieldings imply a possible additive constant, which cannot be obtained from the simulation, the two spectra have been shifted with respect to each other, so that the non-hydrogen bonded protons appear at the same shift in both cases. These protons are not expected to exhibit a nuclear quantum effect. Still, this has to be

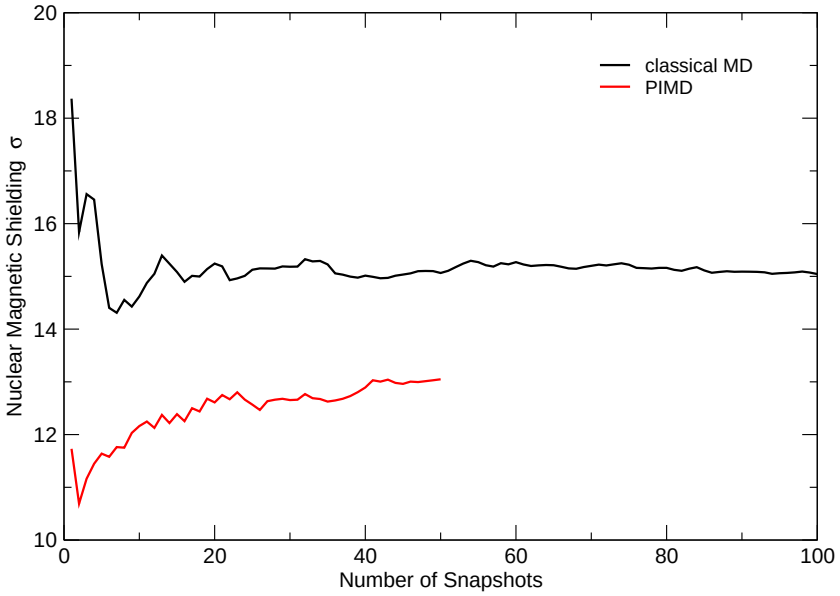

Figure 5.11: Convergence of the nuclear magnetic shielding of the hydrogen bonded proton in ACAC with respect to the number of snapshots. The red spectrum shows the calculation using the path integral formalism, thus including nuclear quantum effects, the black line is the calculation within the classical approximation.

kept in mind and is a possible source of error. The value of special interest, is the shift of the acidic proton between the quantum and classical simulation, which is 1.5 ppm.

The experimental spectrum, that has been acquired in the liquid state, with benzene as solvent, both for protonated and deuterated ACAC is shown in Fig. 5.13 [67]. Technical Details are summarized in Appendix C. Before, the hydrogen bonded species has always been called "proton", because for the calculation it does not make a difference if there is a proton or a deuteron. Now, the proton corresponds to the path integral simulation, whereas the deuteron is expected not to exhibit quantum effects, or only minor effects, due to its higher mass. Matanovic and Doslic have deduced this assumption from the analysis of their IR spectra [64]. Firstly, one can see an additional peak in the experimental spectrum at 3.9 ppm, which is due to the keto form of ACAC, i.e. the methylene group. Further, the peak of the methyl group is split, which arises from the fact that the methyl group in the keto and enol forms appear at different positions, separated by 0.15 ppm. The calculated and experimental spectra have been shifted

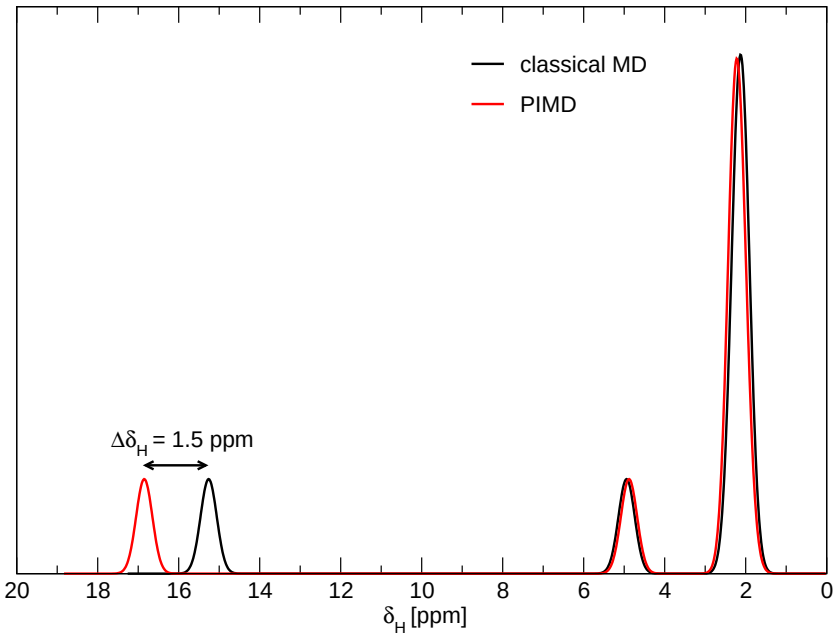

Figure 5.12: Calculated NMR chemical shift spectra for acetylacetone. The red spectrum shows the calculation using the path integral formalism, thus including nuclear quantum effects, the black line is the calculation within the classical approximation. The spectra have been referenced to TMS.

so that the peaks of the methyl groups coincide, so this peak appears to be well reproduced by the simulation, while the peak at 5.9 ppm is a bit off in the calculation. Without this artificially introduced shift, both peaks can be found within approximately 0.5 ppm from the theoretical value, which is the expected accuracy. The proton and the corresponding deuteron peak of the acidic site are shown in the blow-up in Fig. 5.13. The relative shift is 0.7 ppm, and thus, the predicted quantum, or isotope effect, is present even in the experiment.

At first sight, the calculation seems to give a bad estimate, because the shift was calculated as 1.5 ppm, but 0.8 ppm are not much for this kind of response calculation. Actually, this is within the expected error margin. Still, it has been assumed that the deuteron does not exhibit any quantum effect, reflected by the purely classical simulation, which could be too strong of an assumption. A small effect most likely exists, leading to a somewhat higher shift. Also, the overall constant shift that has been applied to the theoretical spectrum might have caused an overestimation of the difference between the two systems.

In conclusion, it has been shown, that the quantum nature of the nuclei affects all investigated properties of the molecule. It leads to a broadening of the distribution of the bond lengths and thus leads to effects on the NMR properties. Although the comparison with the experiment reveals some open questions, the quantum effects in NMR spectra are clearly obtained, showing the abilities of the path integral formalism.

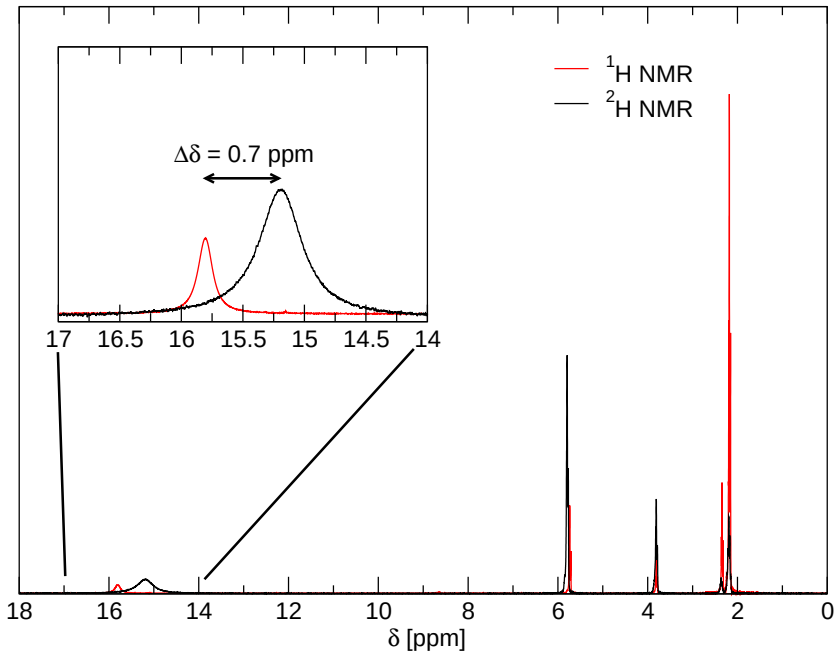

Figure 5.13: Experimental NMR chemical shift spectra [67]. The red line shows the proton spectrum (proton chemical shift), the black one the corresponding measurement for the deuterated sample (deuteron chemical shift). The shift of the acidic site, showing an isotope effect of 0.7 ppm due to proton tunneling can be seen in the blow-up.

5.4 Nuclear quadrupole couplings in benzoic acid

5.4.1 Introduction

The quantum nature of the nuclei can change spectroscopic properties significantly. This has been shown in the previous section. For NMR chemical shifts, this could even be supported by experimental evidence, which has not been done for the NQCCs, because the above examples always treated isolated molecules in the gas phase. The concepts, however, can not only be used in the gas phase, but also, to a certain extent, in the liquid state, where the applicability of this statement crucially depends on the solvent used and its interaction with the molecule being investigated. Still, quadrupole interactions are usually averaged out by isotropic motion in liquids. The situation is different in the solid state, i.e. in crystalline systems. Here, the NQCC can be measured and directly compared to the calculated parameters (see Sec. 3.2.1).

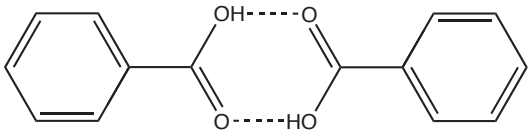

Figure 5.14: Chemical structure of benzoic acid. In the solid state dimers are formed, as shown in the picture. The protons under consideration with respect to NQCCs are the hydrogen bonded ones.

In the following, the quadrupole interaction in benzoic acid and its sensitivity to nuclear quantum effects will be considered. The crystal consists of dimers, as indicated in Fig. 5.14. Recently, the NQCC has been shown to be strongly temperature dependent [30], increasing rather than decreasing with temperature. The corresponding plot is shown in Fig. 5.15. Obviously this effect is not only a minor one, the increase from the optimized geometry to 400 K is about 10%. Still, the experimental value of 115(5) kHz [68] is not reached at the corresponding temperature of 300 K. The increase of the NQCC is due to the motion of the hydrogen bonded deuteron around its average position on the potential energy surface. Thus, a similar effect can be expected from zero point vibrations that have to be taken into account if the quantum nature of the deuteron is treated correctly. Since the path integral method can do this in a natural way, the application of this method could lead to another significant increase towards the experimental

NQCC. So, this work can possibly answer the question if the missing 5-10 kHz are due to quantum effects or rather statistical and systematic errors.

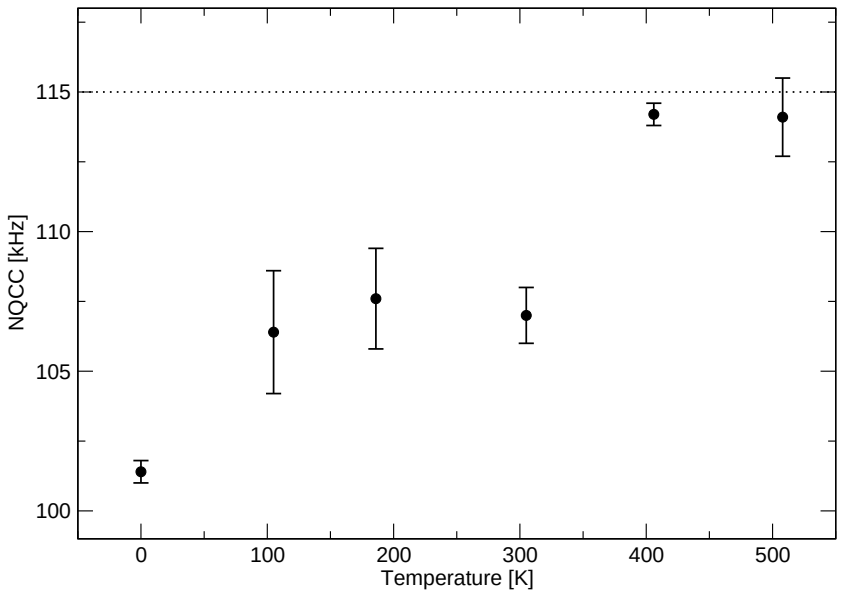

Figure 5.15: Temperature dependence of the NQCC of the hydrogen bonded proton (see Fig. 5.14) of benzoic acid. The values have been extracted from MD simulations at different temperatures, the point at 0 K corresponds to the static structure. The dashed line represents the experimental value at room temperature. The error bars indicate only statistical errors.

Although the O-O distance of the hydrogen bond is about the same as in acetylacetone (ACAC), 2.63 Å the probability for tunneling is much smaller. This is due to the fact, that in benzoic acid the concerted tunneling of two protons is necessary. For ACAC, the tunneling splitting has been estimated to be at least 100 cm^{-1} [64], whereas theoretical calculations carried out by Tautermann et al. [69] yield only $2.2 \cdot 10^{-3}$ cm^{-1} for benzoic acid in the gas phase. The authors state, that for the solid state a splitting of 0.2 cm^{-1} has been found experimentally, but also, that the splitting decreases by approximately three orders of magnitude if the hydrogen bond is deuterated. Since the tunneling amplitude is proportional to the splitting, the effects in benzoic acid can be expected to be much smaller than in ACAC.

5.4.2 Quantum effects on the NQCC

The calculation was performed using a fully periodic description of the crystal with a unit cell, which contained four crystallographically identical molecules of benzoic acid, using the pseudopotential plane wave program package CPMD [20]. The BLYP gradient-corrected exchange-correlation functional was used [12, 13] with pseudopotentials of the Goedecker type [18] and a plane wave cutoff of 100 Ry. The PIMD was run with 16 beads and a time step of 0.1 fs, yielding a total simulation time of 3.75 ps. The initial geometry was taken from a classical, i.e. not path integral, MD of 2 ps and was therefore considered to be equilibrated. The cell parameters have been taken from X-ray data [70, 71]. The staging transformation has been applied to the system and Nosé-Hoover-thermostats with a characteristic frequency of 4000 cm^{-1} and temperature of 300 K have been attached to the degrees of freedom. The hydrogen nuclei have been given the deuteron mass. The initial bead distribution was obtained from a PIMD of 5 ps, that has been performed without staging transformation. After switching to staging, the electric field gradients have been calculated in each step of the run. In Fig. 5.16 the

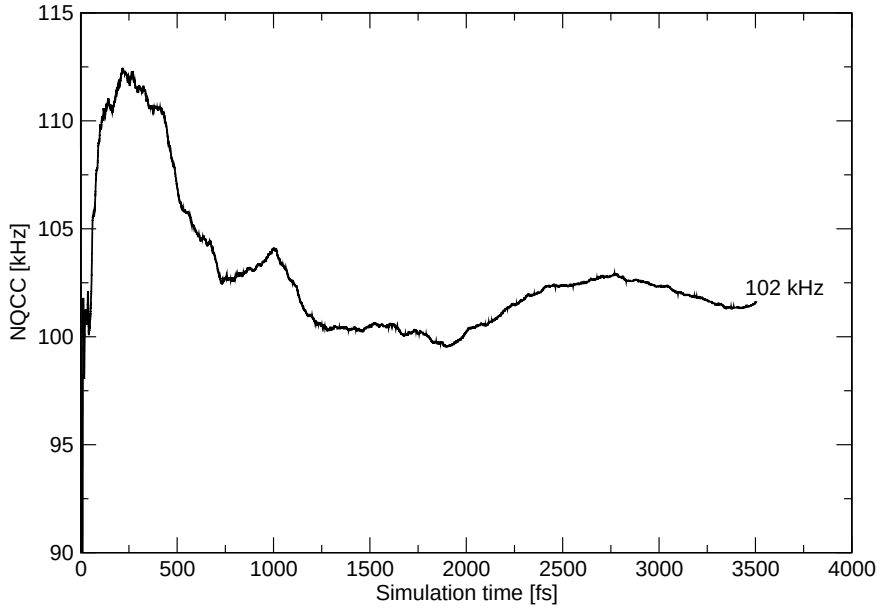

Figure 5.16: Cumulative average of the NQCC of the hydrogen bonded proton (see Fig 5.14) from a path integral simulation at 300 K. At the end of the run the average is 102 kHz, the corresponding value from the simulation within the classical approximation is 107 kHz (see Fig. 5.15).

cumulative average of the NQCC of the hydrogen bonded deuterons is shown. Cumulative average in this case means, that in each step the electric field gradients from all previous steps are averaged and then this effective electric field gradient is diagonalized and the NQCC is obtained (see Sec. 3.2.1). Thus, the curve gives a direct measure for the convergence of the parameter. Although complete convergence is not yet reached, one can estimate that the final value is within 1 kHz from the given 102 kHz by analyzing the variance of the last 1.5 ps of the run. Besides the statistical error, there is another systematic error that is more important. For the calculations shown in Fig. 5.15 a cutoff of 110 Ry has been used, while here, it was set to only 100 Ry. This was done to save time during the computation (the number of plane waves that have to be taken into account is proportional to $E_{cutoff}^{3/2}$ [15]). This leads to a somewhat higher uncertainty on the electric field gradient, the deviation can be up to 5% [65]. In conclusion, one can say that the result of the path integral calculation coincides with the classical result of 107 kHz within the error boundaries.

These findings can be further supported, if one looks at the structural parameters similar to the treatment of ACAC in Sec. 5.3.2. Again, the parameter δ, as explained in Fig. 5.17 is of special interest. If it reveals a significant broadening or a non-zero value at $\delta = 0$, there are important quantum effects, if not, this system is not subject to tunneling or similar phenomena. The latter would also explain the unchanged behavior of the NQCC. Fig. 5.18 displays the bonding parameter δ. The interpretation is obvious: Although there is a minor broadening, the picture remains the same with path integrals. There is no jumping or tunneling happening, the distribution of the deuterons is almost exactly the same as in the classical case.

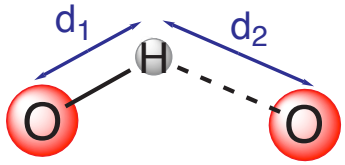

Figure 5.17: Sketch to explain the meaning of the parameter $\delta = d_2 - d_1$.

The final conclusion for this system is, that quantum effects for the NQCC in benzoic acid are not important. As suggested by the small tunneling splitting,

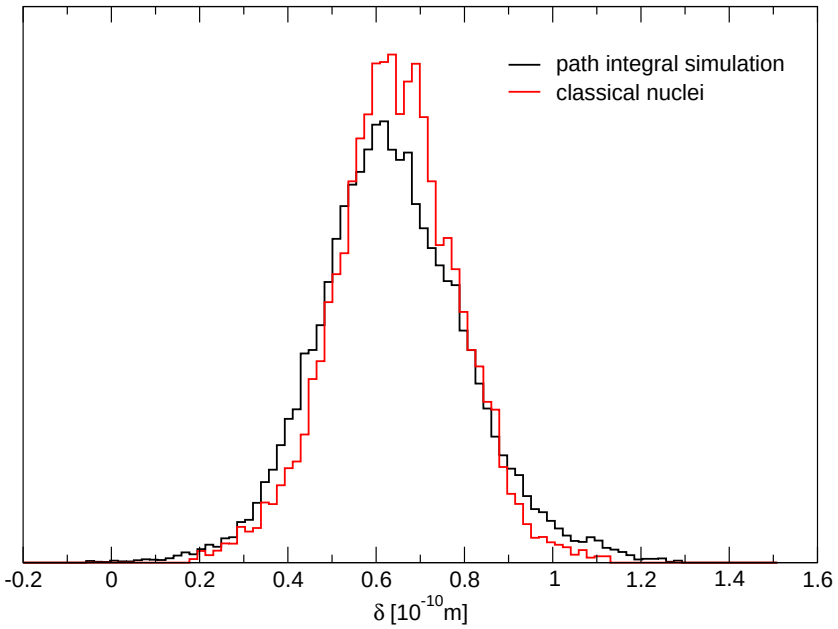

Figure 5.18: The parameter δ (see Fig. 5.17) from a MD simulation with path integrals (black line) and a respective simulation within the classical approximation (red line). No significant changes can be seen, in agreement with the findings for the NQCC (Fig. 5.16).

tunneling is very unlikely. In this simulation it did not occur at all and so the classical picture is preserved, although the length of the hydrogen bond is of the same scale as for ACAC, where tunneling turned out to be quite important.

5.5 Conclusions

In this chapter, nuclear quantum effects on structural and spectroscopic properties have been investigated. These effects are neglected by common MD techniques, based on the Born-Oppenheimer approximation. The nuclei are treated as classical particles that are moving on the potential energy surface created by the electrons. In contrast to this, the path integral formalism naturally includes the quantum nature of the nuclei. The canonical partition function is mapped on a classical "chain of replica" of the considered system with a path integral ansatz. This leads to equations that can be treated by common MD methods, while fully representing the quantum effects in the system. For an efficient sampling of the phase space the staging transformation is crucial in these simulations.

The formalism has been applied to acetylacetone. This molecule is known to exhibit quantum effects, due to its short intramolecular hydrogen bond. Indeed, strong effects on the distribution of the bonded nucleus have been found, the short bond enables tunneling of the proton. This also leads to effects on spectroscopic properties such as the NQCC and NMR chemical shift. For the chemical shift, experimental evidence strongly supports the calculations, although the effect is overestimated by the simulation. This is likely due to the fact that it was assumed, that the deuteron does not tunnel at all, reflected by the fact that it was simulated the classical way, without path integrals. However, all the simulations were performed with an isolated molecule, whereas the experiment was conducted in the liquid state. Since crystalline acetylaceton is available, a treatment in the solid state is possible, both in experiment and theory. This will be part of future work, but could not be done within the framework of this thesis.

Another compound, benzoic acid, has instead been simulated in the solid state. Here, the quantum effects turned out not to be important for the NQCC. Classical and path integral results coincide within the expected error, although the length of the hydrogen bond is comparable to acetylacetone. This reveals that the significance of quantum effects can hardly be estimated, but have to be calculated diligently, for example with the help of the path integral formalism.

The aim of this chapter was the evaluation of the ability of the path integral molecular dynamics method to reproduce nuclear quantum effects on spectro-

scopic properties. It has been shown that the simulations indeed predict these influences on the considered parameters. Still, there are problems with the quantitative agreement with the experiment. On the one hand, this is due to the setup of the systems, which have been kept simple for this test, but on the other hand, the explored structures, as hydrogen bonds, are in general not easy to treat at this level of theory. In conclusion, the path integral formalism was successfully applied to the above-mentioned compounds, revealing the potential for many interesting and important applications.

6 Quadrupole Relaxation in Water

6.1 Introduction

Spectroscopic properties such as NMR chemical shifts or nuclear quadrupole coupling constants (NQCC) can give valuable information about the structure and dynamics of molecular systems. The time scale of an NMR experiment (longer than 10^{-8} s) is large compared to the time scale of microscopic motion, that can be as fast as 10^{-15} s, e.g. vibrational modes. Thus, an accurate description must take this into account and average the desired properties over the whole phase space. A way of achieving this has been shown in the previous chapters, using molecular dynamics (MD) simulations. Furthermore, nuclear quantum effects have also been considered and can yield important contributions to the resulting, effective parameters.

Still, these averaged quantities contain information only about the average structure. A deeper insight into the dynamics and the effects on the spectroscopic parameters is difficult to obtain. While the simulations, in principle, can correlate microscopic, instantaneous coupling parameters with the corresponding structure, this cannot be done in the experiment in a direct way. But there is a more indirect parameter that is sensitive to the time scale and type of dynamics - the longitudinal or spin-lattice relaxation time, usually denoted as T_1 [43]. In a system that allows quadrupole interactions of the involved nuclei, it is basically given by the autocorrelation function of the electric field gradient (EFG). The relaxation due to quadrupole interactions is expected to be the dominating mechanism [42, 43]. The quadrupole relaxation of deuterons and oxygens (^{17}O) of liquid water will be treated here, since it is a simple system, but exhibits complex effects. Moreover, water is probably the most important liquid on earth and will also be considered below (Chapter 7). T_1 has been investigated both experimentally [41, 72, 73, 74]

and theoretically [75, 76, 77, 78] before. The theoretical treatments have always used a limited number of snapshots or an empirical parameterization of the EFG for clusters of water molecules. For example, Hardy et al. calculated dimer contributions to the EFG and fitted these to a parameterized EFG-surface. Afterwards, they summed up these dimer contributions to obtain the full gradient. Although this approximation seems to be accurate, a full consideration of the whole cluster within an ab-initio framework is desirable and presented here.

The EFGs used in this work have been calculated with the GAPW module (see Sec. 2.3.2) of the quantum chemical program package CP2K [21]. This allows for an all-electron treatment of the problem without any pseudopotentials, which enables the calculation of EFGs for all kinds of nuclei. Additionally, standard quantum chemical basis sets are used, which simplifies the comparison of the results to those from other, well tested, programs. Still, the method implies periodic boundary conditions. This, in combination with the parallelization of the CP2K code, opens the way to large-scale applications, as water with 64 molecules in this case, without an approximate treatment of the core electrons of non-hydrogen atoms. The EFGs for both deuterons and oxygens have been computed using a trajectory that had been obtained before from an ab-initio MD simulation of the same system. This allows for the incorporation of both short- and long-ranged contributions and a realistic description of the whole system, without any empirical parameters. Furthermore, both steps can be done on the same level of theory, yielding a consistent picture of the problem.

6.2 EFG in GAPW - Tests and Benchmarks

The calculation of the EFG follows closely the method presented by Blöchl [40] (see also Sec. 3.2.2). Since it has been implemented recently, there have not been any previous tests. Therefore, a couple of test calculations have been conducted to evaluate the accuracy that can be expected. As mentioned before, standard basis sets are used and so the values obtained from standard quantum chemical programs should be reproduced. The tests have been performed using a water dimer in an isolated box. Periodic boundary conditions have not been applied in order to facilitate the computational setup.

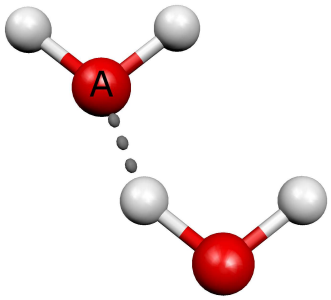

Figure 6.1: Water dimer as used for the test calculations. The benchmark is the largest eigenvalue of the electric field gradient of the atom denoted with A.

In Fig. 6.1 the dimer used for the benchmarks is shown. The actual value considered is the largest eigenvalue of the EFG of the oxygen denoted by the letter 'A'. The reference code is Gaussian [79]. In both codes, the BLYP functional has been employed in combination with various basis sets. For CP2K the water dimer has been put in a 15x15x15 Å box for simulating an isolated system. It has been checked explicitly that the effects arising from the periodic images are negligible.

The results of the calculations are displayed in Fig. 6.2. Since CP2K is using plane waves as auxiliary basis set, the dependence on the density cutoff has been investigated. The results of the reference code are shown as straight lines, since they do not depend on this parameter. It can be seen, that convergence with respect to the cutoff is basically reached at 300 Ry. The basis sets 6-311ppG3f2d and 6-311++G(3df,3pd) are exactly the same set, the former in CP2K-nomenclature, the latter in Gaussian, which consists of a triple-zeta valence basis with diffuse functions and a set of polarization functions (three d-type and one f-type for O, three p-type and 1 d-type for H). The blow-up in Fig. 6.2 shows that the EFG obtained from the two codes coincide within 0.5%. In the following, the basis set 6-31ppG3f2d will be used for saving computational effort. Therefore, the EFG computed with this set is also plotted, indicating that the somewhat smaller basis set has little effect on the EFG. For comparison, some additional results with different sets are also included. It can be seen that the value from CP2K even appears within 3% from the cc-pV5Z set, which can be considered a very large basis.

In conclusion, it has been checked that the ^{17}O EFGs obtained from CP2K agree with those from a well-known reference code. This, of course, also holds for ^{2}H, which is in principle much easier to treat, due to the fact that there are no core electrons. Therefore, the deuteron EFGs can in principle be calculated in a pseudopotential framework as presented recently [30]. The calculation of the EFG in CP2K is similar to the method used in the cited work, since the soft basis functions of hydrogen are completely incorporated in the plane wave part of the GAPW method.

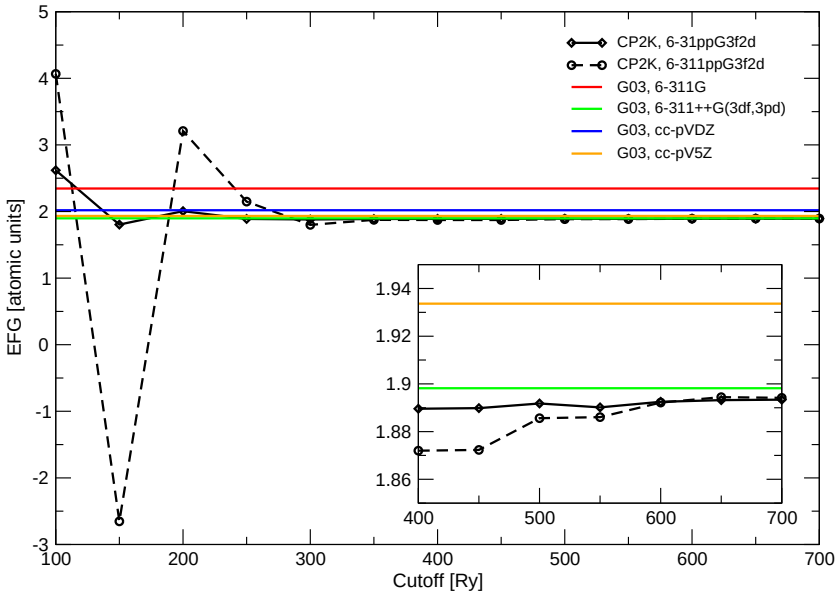

Figure 6.2: Calculated electric field gradient (largest eigenvalue) with various basis sets, plotted against the density cutoff. The straight lines are reference calculations, that don't depend on the cutoff. In the lower right corner a blow-up is shown.

6.3 MD Simulation of Liquid Water

The MD simulation has been performed with the GPW module (see Sec. 2.3.1 and Sec. 7.2.1) of the program package CP2K [21]. The trajectory of the system consisting of 64 molecules of water was computed using Born-Oppenheimer MD, yielding a total simulated time of 35 ps. The BLYP functional has been employed with the norm-conserving pseudopotentials of Goedecker and co-workers (GTH) [18] and a density cutoff of 300 Ry. The Gaussian basis set was a triple-zeta valence basis set augmented with two sets of d-type or p-type polarization functions (TZV2P). This basis set has already been shown to give converged structural and dynamical properties for liquid water at constant volume [80]. A time step of 0.48 fs has been applied and Nosé-Hoover thermostats have been attached to the ions with a temperature of 360 K and a time constant of 2000 cm^{-1}. Although ^{17}O and ^{2}H are the desired nuclei for quadrupole interactions, ^{16}O and ^{1}H masses have been used for the simulation. The reasons will be explained below. The supercell was set to 12.42x12.42x12.42 Å, corresponding to a density of 1 g/cm^3. The initial coordinates have been taken from a previous MD simulation [81] at comparable conditions, but the first 4 ps have not been taken into account for the subsequent calculation of the EFG, allowing for an equilibration of the system.

The temperature is higher than in other simulations of water, which are mostly carried out at 330 K. Furthermore, the standard element masses have been applied instead of the isotope's masses. This has been done for compensating the tendency of DFT to yield overstructured water. The reason is an overestimation of the strength of the hydrogen bonds, caused by the exchange-correlation functionals, leading to a structure that is to stiff and exhibits much less fluctuations. This is a well known issue and has been addressed in many publications [29]. A significant error in the relaxation time and an increased computational effort would be caused by this effect. Both consequences of the deficiency of the DFT description should be avoided by this choice for temperature and masses. Still, the structural properties of the system have to be monitored carefully in order to keep the influences of the mentioned parameters under control. In Fig. 6.3 the evolution of the total energy during the MD simulation is plotted. After 35 ps a relative shift of $3 \cdot 10^{-5}$ is observed, meaning $5 \cdot 10^{-6}$ a.u. per atom per ps.

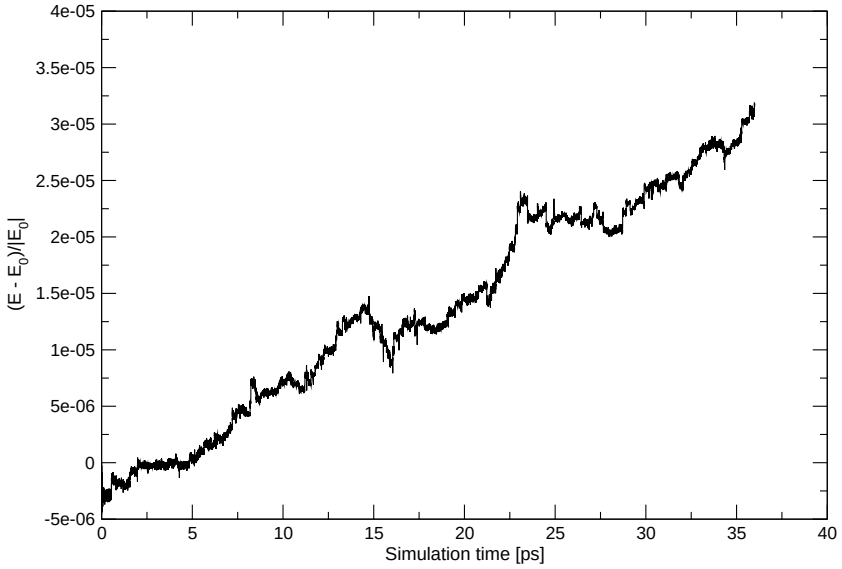

Figure 6.3: Relative change of the conserved quantity during a NVT simulation of water (normalized to the value at $t = 0$).

This can be considered a very good conservation, showing that the computational parameters of the simulation have been chosen properly [24].

Now, the above mentioned structural properties will be investigated. A common gauge of the structural and dynamical parameters are radial distribution functions (RDF). These are measures for the probability of finding another nucleus at distance r from a given one. In the book of Allen and Tildesley an introduction to this topic can be found [27]. Recently, a detailed overview of RDFs in water simulations has been published by Lee and Tuckerman [82]. The most significant parameter is the maximum of the oxygen-oxygen RDF. Most calculations yield numbers between 2.9 and 3.7, which is much larger than the most up to date experimental values, namely, 2.75 from neutron diffraction [83, 84] and 2.8 from x-ray scattering measurements [85, 86]. The cited simulations have been carried out between 300 K and 350 K, using both deuteron and proton masses.

The RDFs computed from this simulation are displayed in Fig. 6.4 and Fig. 6.5 for oxygen-oxygen and oxygen-hydrogen, respectively. It can be seen, that the simulation presented in this work, with the slightly adjusted masses and temperature, yields a maximum of 2.82. This agrees very well with the experimental data at ambient conditions and therefore justifies the choice of parameters. The

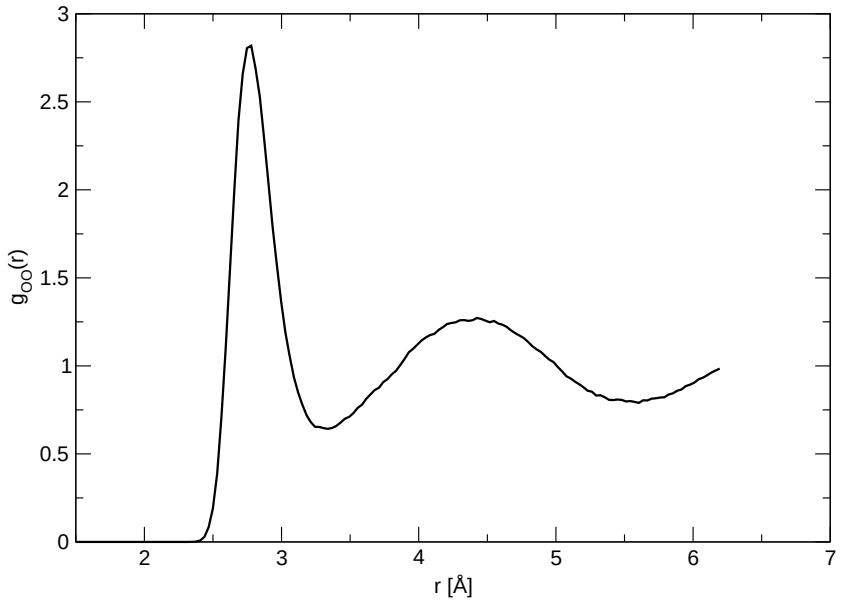

Figure 6.4: Oxygen-oxygen radial distribution function obtained from a molecular dynamics simulation of water. $\rho = 1\mathrm{g/cm}^3, \mathrm{T} = 360K$.

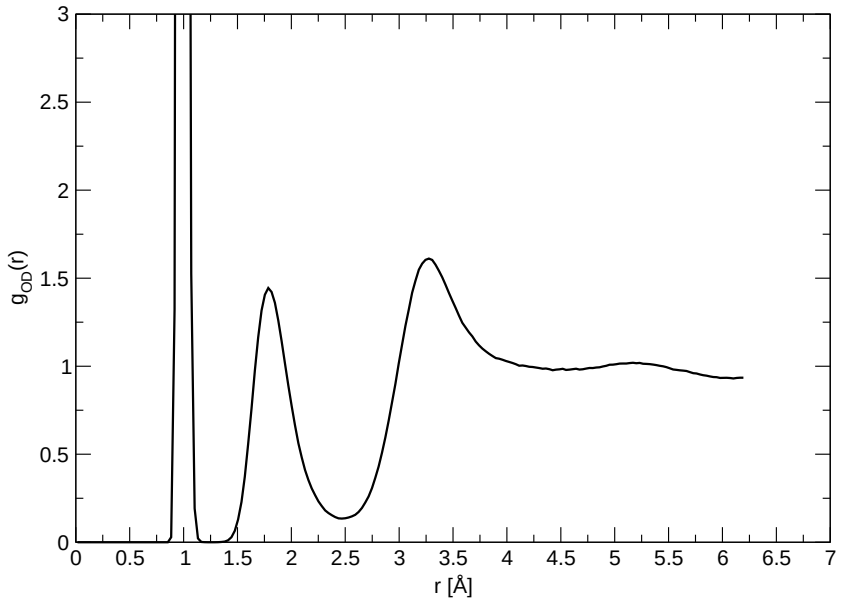

Figure 6.5: Oxygen-hydrogen radial distribution function obtained from a molecular dynamics simulation of water. $\rho = 1\mathrm{g/cm}^3, \mathrm{T} = 360K$.

oxygen-hydrogen RDF is comparable to those from other publications and does not exhibit any unexpected or unusual features. The height of the second peak is 2.42, which agrees well with the findings of Kuo et al. [29]. While the analysis of RDFs in water with respect to all kinds of parameters has been an important issue in the literature during the past years, a more detailed treatment is out of the scope of this work. Here, the RDFs are only used for assuring a reasonable structural behavior of the simulated ensembles. Thus, the MD simulations used in this work provide a good starting point for the evaluation of relaxation times. An adjustment was made to the MD parameters in an attempt to compensate for the known problems of the DFT description. Still, the RDFs only describe the average structure of the system and cannot guarantee that the microscopic dynamics are correct. This, in turn, will be revealed by the autocorrelation of the electric field gradient as needed for the computation of NMR relaxation.

It should be noted that there is another quantity that is often given as a measure for the quality of the description of a water simulation, namely the diffusion constant. Since this parameter can only be calculated with a large error due to statistical problems, it does not give much insight into the dynamical properties of the system. Therefore, the diffusion constant is not presented here, the relaxation time is expected to be a much more appropriate criterion.

6.4 Autocorrelation and Relaxation

The quadrupole relaxation is due to fluctuations of the EFG of the considered nucleus (see Sec. 3.2.3). Thus, the first step is the calculation of the EFGs for a sufficient number of snapshots, taken from the MD simulation described in the previous section. In order to achieve a good sampling of the phase space and to track the time-evolution of the EFG, which is necessary for the needed autocorrelation functions, a calculation has been carried out every two femtoseconds of the MD, starting after 4 ps of equilibration. This results in approximately 15,000 computations, each involving a wave function optimization within the GAPW framework. Each computation took about 3 minutes, technical details of the computers that have been employed can be found in Appendix B. This yielded a total computing time of about 32 days. These calculations have been carried out within a period of three months.

For the calculation of the EFG, the basis set was 6-31ppG3f2d, a triple-zeta valence basis with additional diffuse and polarization functions (three d-type and one f-type for O, three p-type and one d-type for H). The density cutoff for the auxiliary plane wave basis was set to 400 Ry, the BLYP exchange-correlation functional has been used. For the GAPW calculations, no pseudopotentials have been employed, since the full potential had to be incorporated.

In Sec. 3.2.3 the theoretical background of relaxation due to quadrupole interactions is summarized. The relaxation time T_1 is given by

$$\frac{1}{T_1} = \frac{e^2 Q^2 (2I+3)}{40 I^2 (2I-1)\hbar^2} \cdot G_{20}(\omega) \ , \tag{6.1}$$

where e is the elementary charge, Q the quadrupole moment of the considered nucleus (taken from [87]), I its spin and $G_{20}(\omega)$ is defined as

$$G_{20}(\omega) = 4g_{22}(2\omega) + 4g_{2-2}(-2\omega) + g_{21}(\omega) + g_{2-1}(-\omega) \ . \tag{6.2}$$

The frequency ω is the corresponding Larmor-Frequency and the functions $g_{lm}(\omega)$

are the half-sided Fourier transforms of the autocorrelation functions $f_{lm}(t)$:

$$g_{lm}(\omega) = \int_0^\infty f_{lm}(t) e^{i\omega t}\, dt \ , \tag{6.3}$$

and therefore the spectral densities of the considered transition matrix element. The correlation functions $f_{lm}(t)$, in turn, are defined as follows:

$$f_{lm}(t) = (-1)^{l+m} \langle R_{l-m}(0) R_{lm}(-t) \rangle \ . \tag{6.4}$$

The R_{lm} are the elements of the EFG expressed as irreducible tensors (see Sec. 3.2.3), i.e. a linear combination of the EFG in cartesian representation, the brackets $\langle \cdots \rangle$ indicate an average over the whole ensemble. The terms g_{21} and g_{2-1} describe the single quantum contributions to the relaxation, i.e. the change of the magnetic quantum number m by ± 1, while the remaining g_{22} and g_{2-2} are responsible for the double quantum transitions, $\Delta m = \pm 2$. In general, the correlation functions f_{lm} are complex, but in the case of random stationary motions, they are real numbers [42, 43]. In Fig. 6.6 the functions $f_{lm}(t)$ are given for both oxygens and deuterons. First, one can see that the imaginary parts only fluctuate around zero and thus, the approximation of random motion seems to be justified, which was not clear from the beginning for a complex fluid such as water. In experimental publications, the relaxation time T_1^{exp} is often given by

$$\frac{1}{T_1^{exp}} = \frac{6\pi^2 (I+1)(2I+3)}{20 I^2 (2I-1)(I+1)} \frac{\tau_r}{\hbar^2} (eqQ/h)^2_{eff} \ , \tag{6.5}$$

with the *effective quadrupole coupling* $(eqQ/h)_{eff}$. This equations arises, if an exponential decay with a characteristic rotational correlation time τ_r of the autocorrelation functions is assumed [72, 43], i.e.

$$f_{lm}(t) = f_{lm}(0) \cdot e^{-t/\tau_r} \ . \tag{6.6}$$

This assumption, however, is not supported by the autocorrelation functions shown in Fig. 6.6. The functions decay rapidly in the beginning but then exhibit a rather linear dependence on the time. Still, the fluctuations of the functions indicate that the exact functional form depends on the statistics of the simulation

and the actual starting point of the correlation, here $t_0 = 0$. A slightly different t_0 can lead to another form of the curve. This has been tested explicitly, leading to different individual time dependencies, whereas the simple exponential form has not been found, the almost linear decay is always dominant. Other recent theoretical simulations [76] have also found, that the simple exponential decay is not correct, but stated that a multi-exponential ansatz might fit. Indeed, the data from their simulations exhibit a fast initial decay, followed by a slower, but exponential, evolution. In the cited work, an empirically fitted functional for the evaluation of the EFG has been used, which only took dimer contributions into account, possibly leading to the deviations from this work.

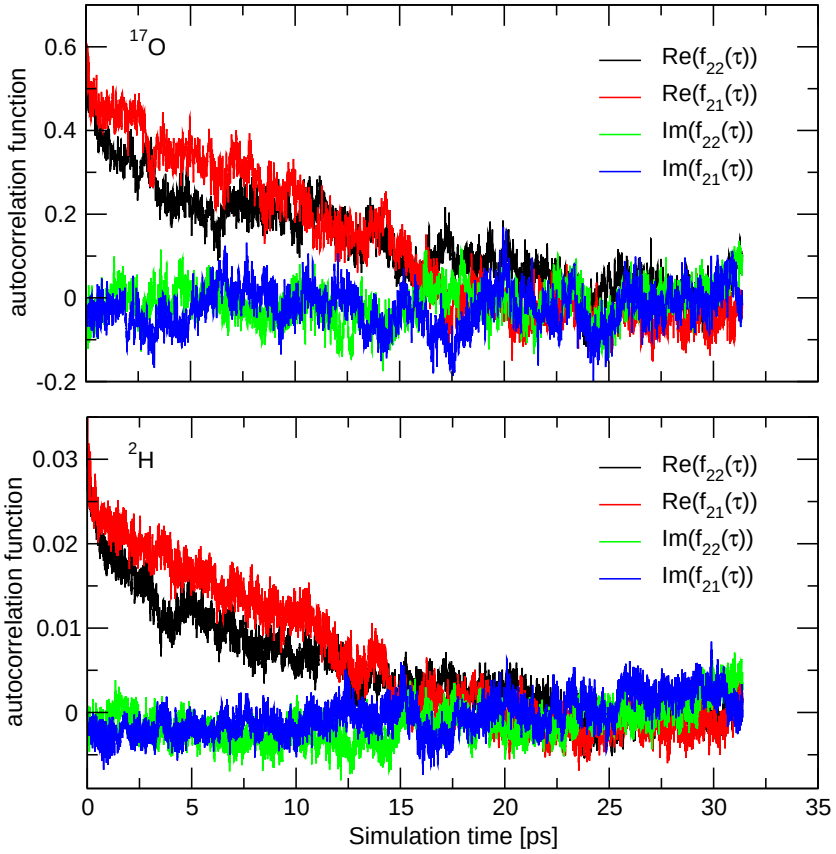

Figure 6.6: Autocorrelation functions f_{22} and f_{21} of the electric field gradient of water. $\rho = 1\mathrm{g/cm}^3$, $\mathrm{T} = 360K$. upper panel: ^{17}O, lower panel: ^{2}H.

Keeping in mind that the individual starting point of the correlation function can influence the form of the curve and thus also the integral, which is needed for the

spectral densities, the error introduced by this uncertainty has to be estimated. In Fig. 6.7 integrals over the function f_{22} are shown, starting at different times of the simulation, i.e. the function

$$g_{22}(t', \omega) = \int_0^{t'} f_{22}(t) e^{i\omega t} \, dt \ . \tag{6.7}$$

Since the f_{lm}'s decay to zero, $g_{lm}(t', \omega)$ converges to a value, yielding the desired $g_{lm}(\omega)$. The error is obtained by fitting the function $g_{lm}(t', \omega)$ with

$$g_{lm}^{fit}(t', \omega) = a \cdot (1 - \exp\{-t'^b/c\}) \ , \tag{6.8}$$

which is shown in the figure as red dashed line. The physical justification for this fit function is given by the above-mentioned assumption that the correlation decays exponentially. The deviation from this is taken into account by the parameter b. The only purpose of this approach is an estimation of the statistical error that has to be expected. This does not necessarily require a physical background of the used fit, but only a good agreement with the data, which is obviously fulfilled. When this procedure is applied to all g_{lm}'s and Eq. 6.1 is used, the following values for the deuteron and oxygen relaxation times are found:

$$T_1^O = 2.3 \pm 0.4 \text{ ms} \ ,$$

$$T_1^D = 0.23 \pm 0.02 \text{ s} \ .$$

The experimental parameters are $T_1^{O,exp} = 6.6$ms and $T_1^{D,exp} = 0.7$s, taken from [72] and [74], respectively. These are values measured at temperatures below 360 K, but as explained in the previous section, the raised temperature has only been used to compensate for the effects of the DFT description. Thus, the effective temperature of the simulation is expected to be comparable to the experimental setup. Still, the calculated relaxation times are shorter than the experimental times by a factor of three, which is a very good agreement if one considers the uncertainty introduced by the effective temperature. In contrast to quantities that are simply averaged over the phase space, the relaxation time depends on the dynamics and thus, an exponential dependence on the temperature has to

be expected. Therefore, the factor of three is only a minor deviation. While the average structure of the liquid, indicated by the RDFs, is well reproduced, the dynamical properties seem to be underestimated. This corresponds to the fact, that DFT produces overstructured water, i.e. there is too less dynamical fluctuation, leading to a shorter relaxation time. Additionally, it is not clear whether the limited size of the simulated system gives rise to correlation effects with the periodic images, again resulting in an increased correlation and shortened T_1. This could be investigated by repeating the whole calculation with fewer molecules, which would lead to larger finite-size effects. Previous theoretical work done by Hardy et al. [76] found a deuteron T_1^D of 1.6 s. Here, an ab-initio approach has been used consistently for the whole simulation, yielding a comparable accuracy.

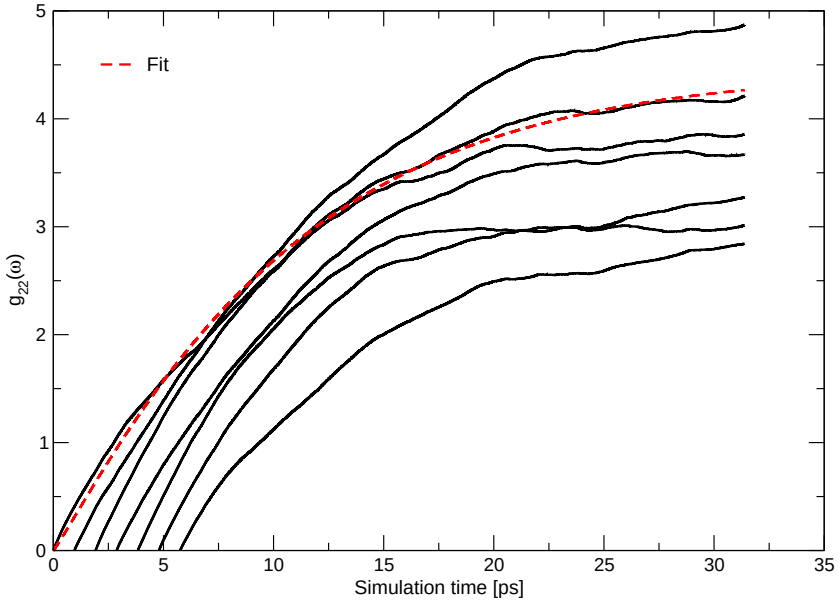

Figure 6.7: Integral over the ^{17}O-autocorrelation function f_{22}. Given are integrals from different starting points, the curve starting at $t = 0$ is fitted by an exponential function, which is plotted in red (see text).

It should be noted, that in the cited work the correlation function

$$f_{efg}(t) = \langle \sum_{ij} V_{ij}(0) V_{ij}(t) \rangle \ , \tag{6.9}$$

with the cartesian EFG tensor elements V_{ij}, has been used. This is also a measure for the autocorrelation of the EFG and leads to comparable results as the usage of

Eq. 6.1, but it is not the correct theoretical result for the relaxation time, causing an additional error in their results. However, an analysis of this work's data with Hardy et al.'s equation revealed only a change in the relaxation time of about 10%.

The equations used for the evaluation of the relaxation time always involve an ensemble average, which naturally appears because only this average can be observed in the experiment. The simulation, on the other hand, gives access to separate data for the individual nuclei. This can be used to explore the origins of the decaying correlation functions. Is it due to collective motion, an effect of the reorientation of the whole cluster, or rather a local phenomenon that mainly involves the dynamic of the respective molecule? This question can be addressed via the autocorrelation functions f_{lm} for the individual nuclei. Theoretical considerations resulting in equations such as Eq. 6.6 usually assume that the most important contribution is the local reorientation of the molecules, and thus, rotational diffusion coefficients are used for the estimation of the rotational correlation time τ_r [42, 43]. Also, studies based on computer simulations have suggested that the EFG is sensitive to local structure rather than to a medium- or long-ranged order [88]. In the following, single nuclei, both oxygen and deuteron, will be investigated with respect to the correlation of the functions f_{lm} with its local structure.

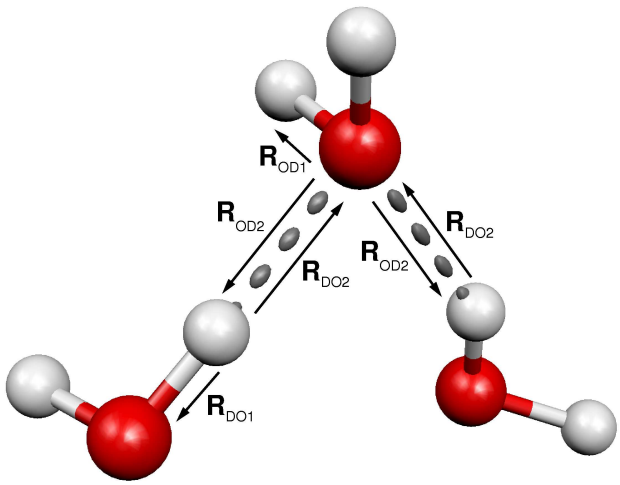

Figure 6.8: Cut-out from a water cluster, explaining the parameters used for the analysis of the data (see text).

In Fig. 6.8 the structural parameters are explained. For the oxygen nucleus, the four closest deuterons are determined and then separated into two groups, first, the two closest ones, corresponding to the covalently bonded deuterons and secondly, the two hydrogen bonded deuterons. For both groups a 6-dimensional vector is built by combining the relative vectors $\boldsymbol{R}_{OD1/2}$, i.e. for the oxygen atom there are the two quantities

$$\boldsymbol{R}_O^1 = (\boldsymbol{R}_{OD1}, \boldsymbol{R}'_{OD1}) \qquad \text{and} \qquad \boldsymbol{R}_O^2 = (\boldsymbol{R}_{OD2}, \boldsymbol{R}'_{OD2}) \ . \tag{6.10}$$

The primed and unprimed vectors refer to the two deuterons belonging to the same group. These vectors are evaluated in each step of the MD simulation and then the autocorrelation is computed, i.e.

$$\langle \boldsymbol{R}_O^i(0) : \boldsymbol{R}_O^i(t) \rangle = \frac{\sum_{j=1}^{6} R_{Oj}^i(0) R_{Oj}^i(t)}{\left(\sum_{j=1}^{6} R_{Oj}^i(0) R_{Oj}^i(0)\right) \left(\sum_{j=1}^{6} R_{Oj}^i(t) R_{Oj}^i(t)\right)} \ , \tag{6.11}$$

which is a generalized scalar product. The same is done for the deuteron, while here the resulting vectors $\boldsymbol{R}_D^1$ and $\boldsymbol{R}_D^2$ are only 3-dimensional, because the two groups only consist of the nearest and second nearest oxygen neighbor, respectively.

The corresponding plots are shown in Fig. 6.9 for the oxygen and in Fig. 6.10 for the deuteron, along with the 1-particle f_{22}. The function f_{22} has been chosen randomly, the others exhibit the same behavior. The comparison of the curves strongly support the assumption that the local structure and its changes mainly contribute to the EFG. It can be seen in Fig. 6.9, that the correlation with the second nearest neighbors is lost within one picosecond, whereas the nearest neighbors stay unchanged, as well as f_{22}. This means, that the hydrogen bonded neighbors are exchanged immediately, but as long as the molecule is not rotated, the field gradient is not affected by this. But when, at approximately 12 ps, the molecule has rotated, the correlation of the EFG is also lost. Still, there is a sharp dip in both f_{22} and the nearest neighbor correlation shortly after the change of the second next neighbors. In the moment, when the hydrogen bonds are broken, the molecule can rotate much easier. This leads to a higher mobility, that is manifested in this dip. New hydrogen bonds are then formed and the molecule is

fixed again. The deuteron in Fig. 6.10 is one of the covalently bonded deuterons of the oxygen discussed above and thus it shows the same behavior. Again, the correlation of the EFG is only lost if the whole molecule rotates and the deuteron loses its hydrogen bond acceptor.

Finally, a parameter that has already been introduced with the experimental equation for the relaxation time, Eq. 6.5, the *effective quadrupole coupling constant* $(eqQ/h)_{eff}$, will be determined from the simulated data. Therefore it is important to understand the way it has been calculated from the experimental data. Eq. 6.5 contains the correlation time τ_r and is based on Eq. 6.6. This means, that the time evolution of the autocorrelation and thus the evolution of the field gradient tensor is incorporated in the exponential factor. Because of this, the procedure of averaging is different from the one described and used in Sec. 5.4.2. This time, the instantaneous tensor is diagonalized and the eigenvalues are averaged over the whole ensemble, instead of averaging the tensor first. The calculated effective couplings and asymmetries η are:

$$(eqQ/h)^{O}_{eff} = 7.9 \pm 0.7\text{MHz} \ , \qquad \eta^{O} = 0.79 \pm 0.15 \ ,$$

$$(eqQ/h)^{D}_{eff} = 229 \pm 60\text{kHz} \ , \qquad \eta^{D} = 0.13 \pm 0.03 \ .$$

These values are very close to the experimentally obtained constants, which are 7.7 MHz for oxygen and 230 kHz for deuterons [41]. This shows again, that the average structure is well reproduced by the simulation, while the dynamical fluctuations are problematic. Although the averaged electric field tensor has not been used here, it is still a meaningful physical quantity. If a nucleus undergoes isotropic motion in a liquid, the resulting quadrupole coupling is zero, because the nuclear quadrupole interaction does not have an isotropic contribution. In turn, if the tensors from the whole simulation are averaged, the result must be zero. Therefore, the NQCC in a liquid is a good indicator for the quality of the simulation. Indeed, the remaining effective couplings found by first averaging the EFG and then finding the eigenvalues are 55 kHz for oxygen and 940 Hz for the deuterons, which means that the tensors are nearly averaged to zero and thus the sampling of the available phase space was sufficient.

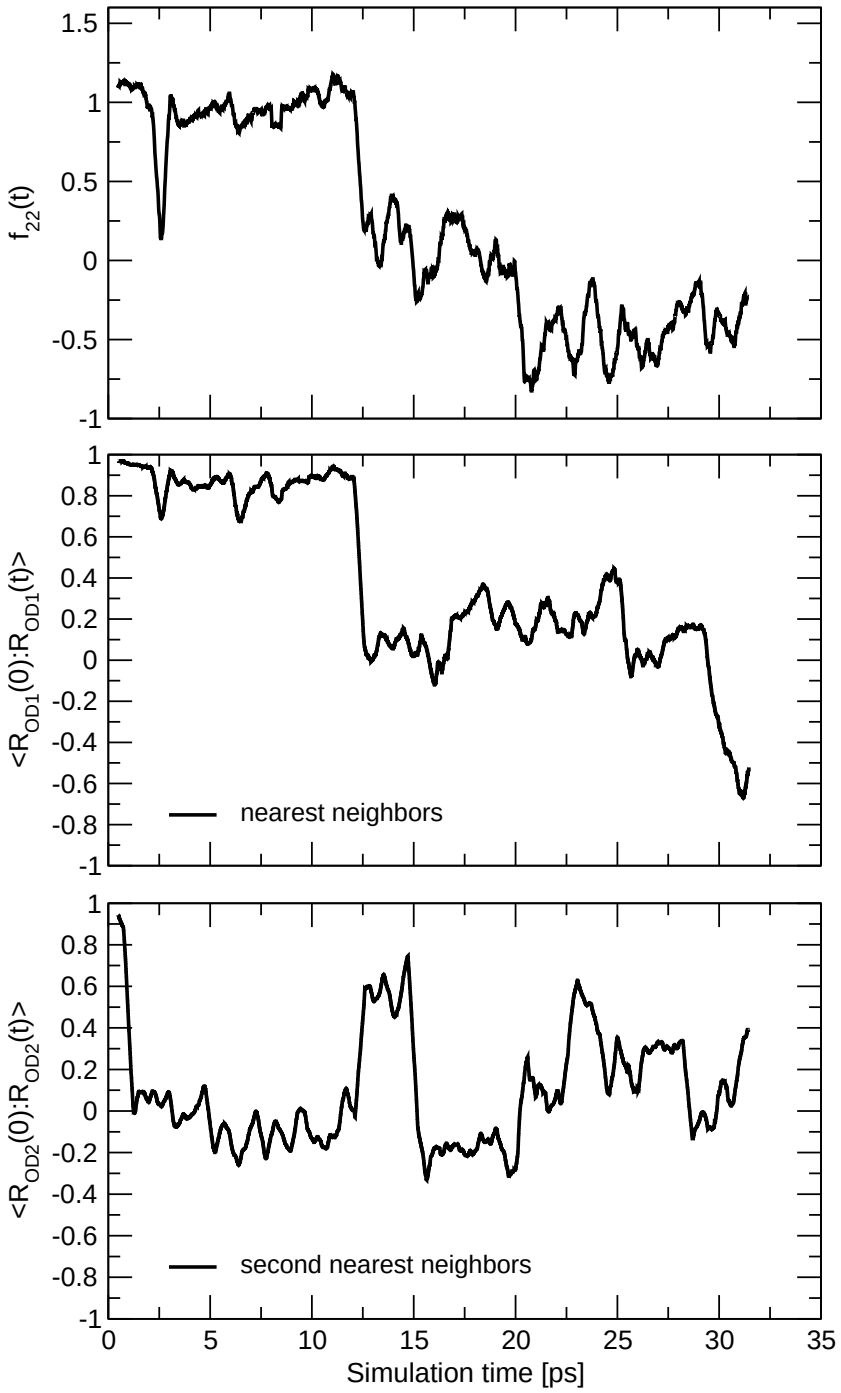

Figure 6.9: First panel: Autocorrelation function f_{22} of the electric field gradient of a single oxygen atom. Second panel: Correlation of the same atom's distance vectors with respect to its nearest deuterons. Third panel: Distance correlation with respect to the second nearest deuterons. For details see text.

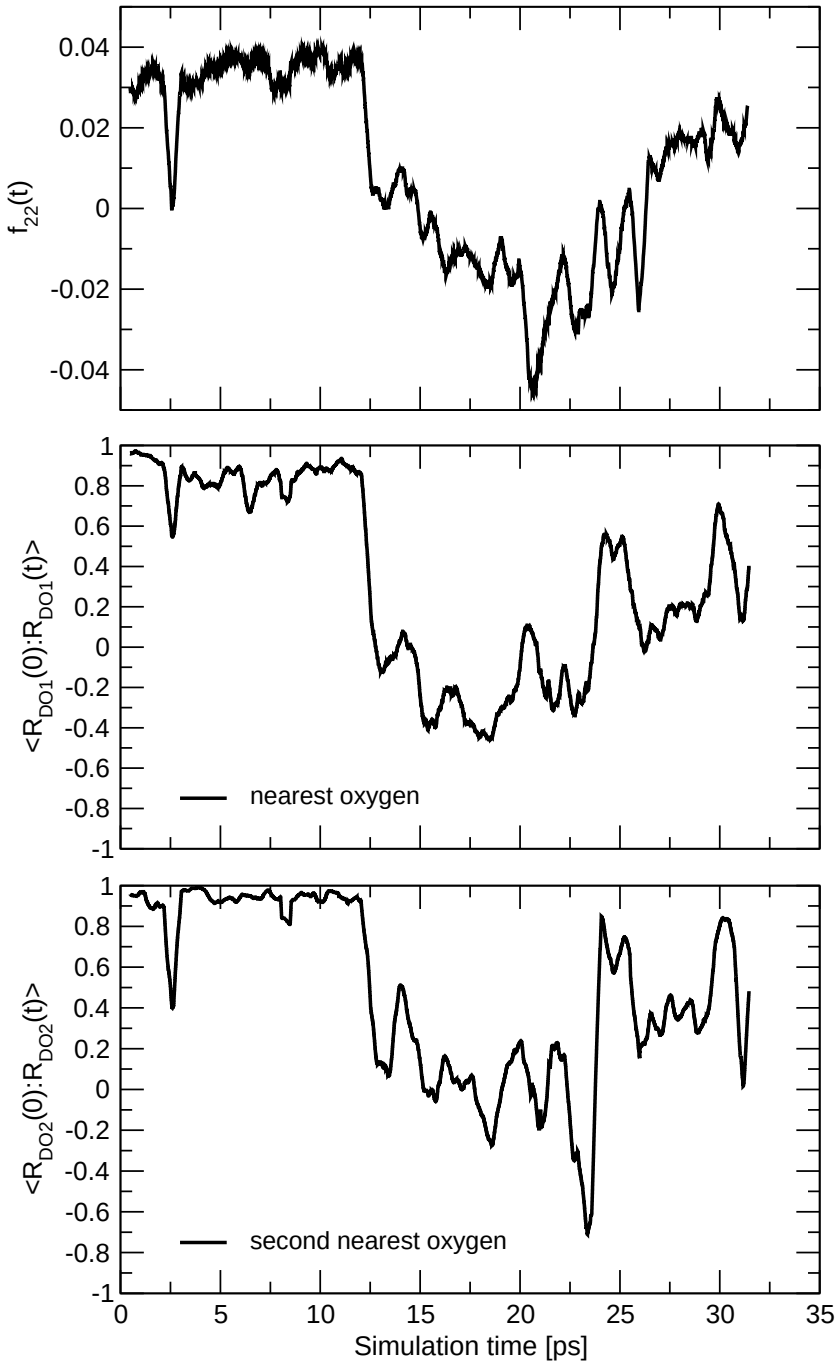

Figure 6.10: First panel: Autocorrelation function f_{22} of the electric field gradient of a single deuteron. Second panel: Correlation of the same atom's distance vector with respect to its nearest oxygen. Third panel: Distance correlation with respect to the second nearest oxygen. For details see text.

6.5 Conclusions

In this chapter, oxygen and deuteron relaxation times have been calculated, using a combined approach of ab-initio MD simulations and subsequent calculations of the EFG. While the calculations of Chapter 5 have been done in order to sample all possible states of a certain ensemble and find the average of a parameter, here, the actual time evolution has been investigated. This question is much more demanding than a simple ensemble average, because the correct expectation value of a quantity can in principle be obtained even if the system visits all states in a completely unphysical order. But if a parameter such as the relaxation time is addressed, which depends on the autocorrelation of a certain observable, the simulation has to resemble the physical time evolution.

During the MD, pseudopotentials have been applied to the oxygens, the EFG has been obtained in an all-electron ab-initio fashion. In the literature [76, 88], the same quantities were calculated using a limited set of representative conformations of a water cluster. Although this approach turned out to be justified to a certain extent, in this work, the full ab-initio electronic structure with periodic boundary conditions has been considered. Thus, for the first time, the MD simulations and the subsequent evaluation of the EFG have been done consistently at the same level of theory.

Compared to the experimental reference, the calculated relaxation times are of the same order of magnitude and differ by a factor of three only. While averaged observables, as effective coupling constants, depend linearly on the structure, correlation times exhibit an exponential dependency on the energetics and are strongly temperature dependent. Thus, small errors in the potential energy surface lead to large deviations in the correlation times. Simulations of liquid water are known to yield overstructured water, i.e. the strength of the hydrogen bonds is overestimated. Therefore, the effective temperature of the hydrogen bonded atoms corresponds only roughly to the temperature set in the simulation. This uncertainty can easily cause the factor of three mentioned above.

The effective quadrupole couplings, however, agree well with the experiment. This means, that the averaged structure has been reproduced well, only the exact dynamics are difficult to obtain from the simulation. Still, the comparison of ex-

periment and simulation allows a direct assessment of the dynamics generated by the computation, which is very difficult otherwise. Regarding the remarkable agreement, both averaged structure and dynamical properties seem to be excellent. Furthermore, the availability of microscopic data for each individual atom in such a simulation enabled the direct correlation of local structure and the EFG of the respective nucleus. This leads to the conclusion, that mainly local dynamics contribute to the autocorrelation functions. This strongly supports the assumption, that has already been introduced in the 1960's [41, 72], that medium- and long-ranged effects can be neglected.

7 Constant Pressure Simulations

7.1 Theoretical Background

7.1.1 Motivation

In a conventional Molecular Dynamics simulation, the total energy E and the total linear momentum $\boldsymbol{P}$ are constants of motion. This implies the usage of the quantum mechanical Hamiltonian

$$\begin{aligned}\mathcal{H} &= \sum_i -\frac{\hbar^2}{2m_e}\nabla_i^2 + \sum_I -\frac{\hbar^2}{2M_I}\nabla_I^2 + \frac{1}{2}\sum_{i\neq j}\frac{e^2}{|\boldsymbol{r}_i - \boldsymbol{r}_j|} + \\ &\quad \frac{1}{2}\sum_{I\neq J}\frac{e^2 Q_I Q_J}{|\boldsymbol{R}_I - \boldsymbol{R}_J|} - \sum_{iI}\frac{e^2 Q_I}{|\boldsymbol{r}_i - \boldsymbol{R}_I|}\ . \end{aligned} \tag{7.1}$$

where electrons are denoted by small (i) and nuclei by capital (I) letters, $\boldsymbol{r}$ and $\boldsymbol{R}$ are position operators of the electrons and nuclei, respectively. In a MD simulation that conserves the number of particles N, the volume of the system and the total energy (given by the above Hamiltonian) E, referred to as NVE simulation, the equations of motion can be derived directly from this Hamiltonian [15].

Most experiments, however, are carried out under conditions of controlled pressure and temperature, thus corresponding to a NPT simulation. This ensemble is generally regarded as the most difficult to generate, due to the requirement that both the kinetic energy and instantaneous pressure must fluctuate according to the respective ensemble distribution function. There are several commonly used algorithms used for the purpose. In Section 7.3.1 the approach used in this work is described.

The main ingredient for NPT simulations is the internal pressure. It has to be

evaluated in each MD step and should therefore require as little computing time as possible. In this work, the analytical and numerical evaluation of the stress tensor (and thus the pressure) in the Gaussian and Plane Wave (GPW) framework (see Section 2.3.1), implemented in the CP2K code [21], has been developed. The following sections describe the theoretical background and the technical details of this calculation.

7.1.2 Basic Thermodynamics

The pressure in a canonical ensemble is given by the basic thermodynamic relation [89, 90]

$$P = -\left(\frac{\partial A(N,V,T)}{\partial V}\right)_{N,T} = kT\left(\frac{\partial \ln Q(N,V,T)}{\partial V}\right)_{N,T} , \tag{7.2}$$

where A is the Helmholtz free energy and Q is the canonical partition function

$$Q(N,V,T) = \frac{1}{N!h^{3N}} \int d\boldsymbol{x} e^{-\beta H(\boldsymbol{x})} . \tag{7.3}$$

The Hamiltonian H in this case is only a function of $\boldsymbol{x}$ and not an operator as in Eq. (7.1), acting on the classical nuclei that move in the effective potential of the electrons. The following relation between A and Q will also be needed:

$$A(N,V,T) = -\frac{1}{\beta} \ln Q(N,V,T) . \tag{7.4}$$

If the integration over the whole phase space in Eq. (7.3) is split into a momentum and a position part, it reads

$$Q(N,V,T) = C_N \int d\boldsymbol{x} e^{-\beta H(\boldsymbol{x})} = C_N \int d^N\boldsymbol{p} \int_V d^N\boldsymbol{r} e^{-\beta H(\boldsymbol{p},\boldsymbol{r})} . \tag{7.5}$$

The volume dependence of the partition function is contained in the limits of integration. For example, if the system is confined within a cubic box of volume $V = L^3$, with L the length of one side, then the range of each integration over r will be from 0 to L. If a change of variables is made to $s_i = r_i/L$, then the range of each s integration will be from 0 to 1. The coordinates s_i are known as *scaled*

coordinates. For containers of a more general shape, a possible transformation is

$$\boldsymbol{s}_i = V^{-1/3}\boldsymbol{r}_i \ . \tag{7.6}$$

In order to ensure that the phase space volume element is preserved, the transformation has to be canonical. This can be achieved by choosing the corresponding transformation of the momentum as

$$\boldsymbol{\pi}_i = V^{1/3}\boldsymbol{p}_i \ . \tag{7.7}$$

Now the transformation is applied to the general Hamiltonian

$$H = \sum_{i=1}^{N} \frac{\boldsymbol{p}_i^2}{2m_i} + U(\boldsymbol{r}_1, \ldots, \boldsymbol{r}_N) \ , \tag{7.8}$$

where U is the potential energy. Then it becomes

$$H = \sum_{i=1}^{N} \frac{V^{-2/3}\boldsymbol{\pi}_i^2}{2m_i} + U(V^{1/3}\boldsymbol{s}_1, \ldots, V^{1/3}\boldsymbol{s}_N) \ , \tag{7.9}$$

and the canonical partition function is

$$Q(N,V,T) = C_N \int d^N\boldsymbol{\pi} \int d^N\boldsymbol{s} \exp\left\{-\beta\left[\sum_{i=1}^{N} \frac{V^{-2/3}\boldsymbol{\pi}_i^2}{2m_i} + U(V^{1/3}\boldsymbol{s}_1, \ldots, V^{1/3}\boldsymbol{s}_N)\right]\right\} .$$

Using the canonical partition function in this form, the pressure can be calculated directly by explicit differentiation with respect to the volume V:

$$\begin{aligned}
P &= kT\frac{1}{Q}\frac{\partial Q}{\partial V} \\
&= \frac{kT}{Q}C_N \int d^N\boldsymbol{\pi} \int d^N\boldsymbol{s} \left[\frac{2}{3}\beta V^{-5/3}\sum_{i=1}^{N}\frac{\boldsymbol{\pi}_i^2}{2m_i} - \frac{\beta}{3}V^{-2/3}\sum_{i=1}^{N}\boldsymbol{s}_i \cdot \frac{\partial U}{\partial(V^{1/3}\boldsymbol{s}_i)}\right] e^{-\beta H} \\
&= \frac{kT}{Q}C_N \int d^N\boldsymbol{p} \int d^N\boldsymbol{r} \left[\frac{\beta}{3V}\sum_{i=1}^{N}\frac{\boldsymbol{p}_i^2}{m_i} - \frac{\beta}{3V}\sum_{i=1}^{N}\boldsymbol{r}_i \cdot \frac{\partial U}{\partial \boldsymbol{r}_i}\right] e^{-\beta H(\boldsymbol{p},\boldsymbol{r})} \\
&= \frac{1}{3V}\left\langle \sum_{i=1}^{N}\left(\frac{\boldsymbol{p}_i^2}{m_i} + \boldsymbol{r}_i \cdot \boldsymbol{F}_i\right)\right\rangle
\end{aligned}$$

$$= \left\langle -\frac{\partial H}{\partial V} \right\rangle \ . \tag{7.10}$$

The brackets $< \ldots >$ denote the ensemble average. The quantity

$$\Pi(\boldsymbol{p}_1, \ldots, \boldsymbol{p}_N, \boldsymbol{r}_1, \ldots, \boldsymbol{r}_N) = \Pi(\boldsymbol{x}) = \frac{1}{3V} \left[\sum_{i=1}^{N} \left(\frac{\boldsymbol{p}_i^2}{m_i} + \boldsymbol{r}_i \cdot \boldsymbol{F}_i \right) \right] \tag{7.11}$$

is called *pressure estimator*. In NPT simulations the pressure estimator has to be calculated in each step and the result is considered the instantaneous pressure of the system. Since the kinetic energy, i.e. the momenta, and the forces on the ions are evaluated anyway, the calculation of the pressure is straightforward and almost without any additional computational cost.

7.1.3 Stress-Tensor

In the last section the pressure has only be considered as an isotropic quantity, i.e. the same force per area is applied all over the whole sample. There are many cases, where the application of force (stress) in certain directions leads to interesting effects (piezoelectric materials). The theoretical description, and also the simulation, of such effects needs a more elaborate quantity than pressure. This quantity is referred to as *stress tensor*. In the following, it will be derived from the ideas presented in the previous section.

The unit cell of a periodically repeated system, as used in this work, is defined by the Bravais lattice vectors $\boldsymbol{a}_1$, $\boldsymbol{a}_2$ and $\boldsymbol{a}_3$. These vectors can be combined into a three by three matrix $\mathbf{h} = [\boldsymbol{a}_1, \boldsymbol{a}_2, \boldsymbol{a}_3]$. The volume V of the cell is then calculated as the determinant of $\mathbf{h}$

$$V = \det \mathbf{h} \ . \tag{7.12}$$

The reciprocal lattice vectors $\boldsymbol{b}_i$ are defined by the relation

$$\boldsymbol{b}_i \cdot \boldsymbol{a}_j = 2\pi\delta_{ij} \ . \tag{7.13}$$

This means that the vectors $\boldsymbol{b}_i$ are related to the matrix $\mathbf{h}$ by

$$[\boldsymbol{b}_1, \boldsymbol{b}_2, \boldsymbol{b}_3] = 2\pi \left(\mathbf{h}^T \right)^{-1} \ . \tag{7.14}$$

Now a transformation of the coordinates, similar to the one applied in Sec. 7.1.2, is introduced:

$$\boldsymbol{r} = \mathbf{h} \cdot \boldsymbol{s} \ , \quad \text{with } s_i \in [0, 1[\ , i = 1, 2, 3 \ . \tag{7.15}$$

Again, the vectors $\boldsymbol{s}$ are scaled coordinates. As in the previous section, the momenta of the particles have to be scaled accordingly, to assure that the transformation is canonical:

$$\boldsymbol{p} = \mathbf{h}^{-1} \cdot \boldsymbol{\pi}. \tag{7.16}$$

In the following, the atomic positions $\boldsymbol{R}_I$ are also expressed in terms of scaled coordinates $\boldsymbol{S}_I = \mathbf{h}^{-1}\boldsymbol{R}_I$, and the atomic momenta $\boldsymbol{P}_I$ in terms of the scaled momenta $\boldsymbol{\pi}_I = \mathbf{h}\boldsymbol{P}_I$. If scaled coordinates are used, the energy depends on the matrix elements $h_{\alpha\beta}$ and the coordinates $\boldsymbol{S}_I$, or the elements $h^{-1}_{\alpha\beta}$ and the momenta $\boldsymbol{\pi}_I$, respectively. In this case, small letters are used for the scaled momenta of the nuclei, in order to avoid confusion with the stress tensor, which will be denoted by a capital Π later on. The transformation is constructed such that a change of volume only affects the matrices, but not the scaled coordinates. Actually, the dependence is the other way around, i.e. the volume is affected by a change of the lattice vectors. The change of one matrix element $h_{\alpha\beta}$ by an infinitesimal $\delta h_{\alpha\beta}$ is given by

$$h_{\alpha\beta} \quad \longrightarrow \quad h_{\alpha\beta} + \delta h_{\alpha\beta} \ . \tag{7.17}$$

The volume can be derived with respect to the matrix element $h_{\alpha\beta}$ by using the relation in Eq. (7.12) and yields (see Appendix A):

$$\frac{\partial V}{\partial h_{\alpha\beta}} = V \left(h^{-1}\right)^T_{\alpha\beta} \ . \tag{7.18}$$

Thus, the change in volume can be written as

$$\delta V = V \left(h^{-1}\right)^T_{\alpha\beta} \cdot \delta h_{\alpha\beta} \ . \tag{7.19}$$

The energy will here be denoted by H in analogy to Eq. (7.10). Its change due to the new volume is given by:

$$\delta H = -P \cdot \delta V = -P \cdot V \left(h^{-1}\right)^T_{\alpha\beta} \cdot \delta h_{\alpha\beta} \ . \tag{7.20}$$

In this equation all quantities are scalar components, i.e. there is no implicit summation, and it can be divided by $\delta h_{\alpha\beta}$ and the result is read as partial derivative (in the infinitesimal limit):

$$\frac{\partial H}{\partial h_{\alpha\beta}} = -P \cdot V \left(h^{-1}\right)^T_{\alpha\beta} \ . \tag{7.21}$$

In the last step, both sides are multiplied with $h_{\alpha\beta}$ and summed over α and β, leading to

$$\begin{aligned} \sum_{\alpha\beta} h_{\alpha\beta} \frac{\partial H}{\partial h_{\alpha\beta}} &= \sum_{\alpha\beta} -P \cdot V \left(h^{-1}\right)^T_{\alpha\beta} \ h_{\alpha\beta} \\ &= \sum_{\beta} -P \cdot V \\ &= -3 \ PV \ . \end{aligned} \tag{7.22}$$

Thus, the pressure P is given by

$$\begin{aligned} P &= -\frac{1}{3V} \sum_{\alpha\beta} h_{\alpha\beta} \frac{\partial H}{\partial h_{\alpha\beta}} \\ &= \mathrm{Tr} \ \mathbf{\Pi} \ , \end{aligned} \tag{7.23}$$

where the *internal stress tensor* $\mathbf{\Pi}$ has been defined by its elements:

$$\Pi_{\alpha\beta} = -\frac{1}{3V} \sum_{\mu} \frac{\partial H}{\partial h_{\alpha\mu}} h^T_{\mu\beta} \ . \tag{7.24}$$

It should be noted that in Eq. (7.20) the isotropic pressure P is used, so, in principle, this derivation only holds for the isotropic case. But this is only for making the stress tensor and its definition plausible. The isotropic pressure can also be derived as a special case, starting with Eq. (7.24). The stress tensor is much more general than the simple idea of isotropic pressure and should therefore be considered the fundamental quantity. Although this definition of the stress tensor and pressure seems to be more complicated than the previous description using the virial, the calculation can be traced back to Eq. (7.11). This will be demonstrated below. The starting point is the potential energy, which is of the

form $U = U(\boldsymbol{R}_1, \ldots, \boldsymbol{R}_N)$, in a system consisting of N atoms. The derivatives with respect to the matrix elements $h_{\alpha\beta}$ can easily be taken using Eq. (7.15):

$$\begin{aligned}
\Pi^{pot}_{\alpha\beta} &= -\frac{1}{3V} \sum_{\mu} \frac{\partial U(\mathbf{h}\boldsymbol{S}_1, \ldots, \mathbf{h}\boldsymbol{S}_N)}{\partial h_{\alpha\mu}} h^T_{\mu\beta} \\
&= -\frac{1}{3V} \sum_{\mu} \sum_{I} \sum_{\nu=1}^{3} \frac{\partial U}{\partial R_{I\nu}} \frac{\partial R_{I\nu}}{\partial h_{\alpha\mu}} \; h^T_{\mu\beta} \\
&= -\frac{1}{3V} \sum_{\mu} \sum_{I} \sum_{\nu=1}^{3} \left(-F_{I\nu} \; \delta_{\alpha\nu} S_{I\mu} \; h^T_{\mu\beta} \right) \\
&= \frac{1}{3V} \sum_{I} F_{I\alpha} \; R_{I\beta}
\end{aligned} \tag{7.25}$$

where the relation

$$\begin{aligned}
\frac{\partial R_{I\nu}}{\partial h_{\alpha\mu}} &= \frac{\partial}{\partial h_{\alpha\mu}} \sum_{\epsilon} h_{\nu\epsilon} S_{I\epsilon} \\
&= \delta_{\alpha\nu} S_{I\mu}
\end{aligned} \tag{7.26}$$

has been used. The result is similar to Eq. (7.11), but it is still more general than the simple scalar isotropic pressure. The kinetic part of the stress tensor is slightly more complicated, because it involves the derivatives of the inverse matrix $\mathbf{h}^{-1}$ with respect to the elements of $\mathbf{h}$. These are given by

$$\frac{\partial h^{-1}_{ij}}{\partial h_{\alpha\mu}} = -h^{-1}_{i\alpha} h^{-1}_{\mu j} \; . \tag{7.27}$$

The complete derivation of this relation is shown in Appendix A. The kinetic energy can be written as

$$\begin{aligned}
E^{kin} &= \sum_{I} \frac{\boldsymbol{P}_I^2}{2M_I} \\
&= \sum_{I} \frac{1}{2M_I} \sum_{i} \left(\sum_{j} h^{-1}_{ij} \pi_{Ij} \right) \left(\sum_{k} h^{-1}_{ik} \pi_{Ik} \right) \\
&= \sum_{I} \frac{1}{2M_I} \sum_{ijk} h^{-1}_{ij} \pi_{Ij} h^{-1}_{ik} \pi_{Ik} \; .
\end{aligned} \tag{7.28}$$

With the help of Eq. (7.27) the derivative within the stress tensor can be evaluated:

$$\begin{aligned}\frac{\partial E^{kin}}{\partial h_{\alpha\mu}} &= \frac{\partial}{\partial h_{\alpha\mu}} \sum_I \frac{1}{2M_I} \sum_{ijk} h_{ij}^{-1} \pi_{Ij} h_{ik}^{-1} \pi_{Ik} \\ &= \sum_I \frac{1}{M_I} \sum_{ijk} \frac{\partial h_{ij}^{-1}}{\partial h_{\alpha\mu}} \pi_{Ij} h_{ik}^{-1} \pi_{Ik} \\ &= \sum_I \frac{1}{M_I} \sum_{ijk} \left(-h_{i\alpha}^{-1} h_{\mu j}^{-1}\right) \pi_{Ij} h_{ik}^{-1} \pi_{Ik} \\ &= -\sum_I \frac{1}{M_I} \sum_i h_{i\alpha}^{-1} P_{I\mu} P_{Ii} \end{aligned} \tag{7.29}$$

This result can be substituted into the definition of the stress tensor, Eq. (7.24), leading to

$$\begin{aligned}\Pi_{\alpha\beta}^{kin} &= -\frac{1}{3V} \sum_\mu \frac{\partial E^{kin}}{\partial h_{\alpha\mu}} h_{\mu\beta}^T \\ &= \frac{1}{3V} \sum_I \frac{1}{M_I} \sum_{\mu i} h_{i\alpha}^{-1} P_{I\mu} P_{Ii} h_{\mu\beta}^T \ . \end{aligned} \tag{7.30}$$

This equation still involves the elements of the transformation matrix and does not resemble the result that is known from the isotropic case in Eq. (7.11). But if the trace of the tensor is calculated, the elements $h_{i\alpha}^{-1}$ and $h_{\mu\beta}^T$ cancel and the expected relation is found.

In this section it has been seen, that a more general definition of the pressure can be found, using the stress tensor, that allows for non-isotropic applications of stress. Still, in the next sections the isotropic formulation of the previous section will be used for the sake of simplicity. All following statements can easily be extended to the more general framework of stress by using the relations presented in this section.

7.1.4 Pressure and Periodic Boundary Conditions

As described in the previous Sections 7.1.2 and 7.1.3, the pressure is given as the ensemble average of the *pressure estimator* Π:

$$P = \langle \Pi(\boldsymbol{x}) \rangle \ , \tag{7.31}$$

where Π contains a sum over $\boldsymbol{r}_i \cdot \boldsymbol{F}_i$. The explicit occurrence of the absolute Cartesian coordinate r is a problem in periodic systems as treated in this work. The coordinate r is simply not well defined in an infinitely repeated system. This means that the virial, $\sum_i \boldsymbol{r}_i \cdot \boldsymbol{F}_i$, has to be rewritten in a form appropriate for periodic boundary conditions. This can be accomplished by assuming that the force F_i is obtained as a sum of contributions F_{ij}, which are the forces on particle i due to particle j. This assumption will be shown to be useful later on. Then, the classical virial becomes

$$\begin{aligned}
\sum_{i=1}^{N} \boldsymbol{r}_i \cdot \boldsymbol{F}_i &= \sum_{i=1}^{N} \boldsymbol{r}_i \cdot \sum_{j \neq i} \boldsymbol{F_{ij}} \\
&= \frac{1}{2} \left[\sum_i \boldsymbol{r}_i \cdot \sum_{j \neq i} \boldsymbol{F}_{ij} + \sum_j \boldsymbol{r}_j \cdot \sum_{i \neq j} \boldsymbol{F}_{ji} \right] \\
&= \frac{1}{2} \left[\sum_i \boldsymbol{r}_i \cdot \sum_{j \neq i} \boldsymbol{F}_{ij} - \sum_j \boldsymbol{r}_j \cdot \sum_{i \neq j} \boldsymbol{F}_{ij} \right] \\
&= \frac{1}{2} \sum_{i,j,i \neq j} (\boldsymbol{r}_i - \boldsymbol{r}_j) \cdot \boldsymbol{F}_{ij} = \frac{1}{2} \sum_{i,j,i \neq j} \boldsymbol{r}_{ij} \cdot \boldsymbol{F}_{ij} \ ,
\end{aligned} \tag{7.32}$$

where $\boldsymbol{r}_{ij}$ is a relative coordinate and thus well defined even in periodic systems. It has to be computed consistently with the boundary conditions, i.e. the relative coordinate is defined with respect to the closest periodic images of the particles i and j.

7.2 Stress Tensor in the GPW framework

7.2.1 Forces in GPW

In the previous sections (7.1.2 and 7.1.4) it has been demonstrated, that for the computation of an instantaneous pressure during an MD simulation the *pressure estimator* Eq. (7.11) has to be evaluated. The momenta of the nuclei can be readily used since they are needed for the kinetic energy, so only the virial part $\sum_i \boldsymbol{r}_i \cdot \boldsymbol{F}_i$ is left to be calculated. This term contains the positions of the particles (or rather relative coordinates since Eq. (7.32) is used) and the forces.

In the following, the details of the pressure calculation in the computer code CP2K [21], precisely the DFT module called QUICKSTEP are described. QUICKSTEP is an implementation of the *gaussian and plane wave* (GPW) method [23, 24]. For an introduction to GPW also see Sec. 2.3.1.

The Kohn-Sham DFT energy within the GPW framework is defined as

$$\begin{aligned} E[n] &= E_T[n] + E_V[n] + E_H[n] + E_{xc}[n] + E_{II} \\ &= \sum_{\mu,\nu} P^{\mu\nu} \langle \phi_\mu(\boldsymbol{r}) | -\frac{1}{2}\nabla^2 | \phi_\nu(\boldsymbol{r}) \rangle \\ &\quad + \sum_{\mu,\nu} P^{\mu\nu} \langle \phi_\mu(\boldsymbol{r}) | V_{loc}^{PP}(r) | \phi_\nu(\boldsymbol{r}) \rangle \\ &\quad + \sum_{\mu,\nu} P^{\mu\nu} \langle \phi_\mu(\boldsymbol{r}) | V_{nl}^{PP}(\boldsymbol{r},\boldsymbol{r}') | \phi_\nu(\boldsymbol{r}') \rangle \\ &\quad + 2\pi\Omega \sum_{\boldsymbol{G}} \frac{\tilde{n}^*(\boldsymbol{G})\tilde{n}(\boldsymbol{G})}{\boldsymbol{G}^2} + \int e_{xc}(\boldsymbol{r}) d\boldsymbol{r} \\ &\quad + \frac{1}{2} \sum_{I \neq J} \frac{Z_I Z_J}{|\boldsymbol{R}_I - \boldsymbol{R}_J|} \,, \end{aligned} \tag{7.33}$$

where $E_T[n]$ is the electronic kinetic energy, $E_V[n]$ is the electronic interaction with the ionic cores, $E_H[n]$ is the electronic Hartree energy, $E_{xc}[n]$ is the exchange-correlation energy and E_{II} is the interaction energy of the ionic cores with charges Z_A and positions $\boldsymbol{R}_A$. Ω is the volume of the unit cell and $\boldsymbol{G}$ are reciprocal lattice vectors. The interaction of the electrons with the ionic cores is described by a pseudo-potential (see Sec. 2.2.1), containing a local $V_{loc}^{PP}(r)$ and a non-local part $V_{nl}^{PP}(\boldsymbol{r},\boldsymbol{r}')$. The electronic density n can be represented both by atom centered,

contracted Gaussian functions

$$n(\boldsymbol{r}) = \sum_{\mu,\nu} P^{\mu\nu} \phi_\mu(\boldsymbol{r}) \phi_\nu(\boldsymbol{r}) \tag{7.34}$$

where $P^{\mu\nu}$ is a density matrix element, or by plane waves

$$\tilde{n}(\boldsymbol{r}) = \frac{1}{\Omega} \sum_{\boldsymbol{G}} \tilde{n}(\boldsymbol{G}) \exp\left(i\boldsymbol{G} \cdot \boldsymbol{r}\right) . \tag{7.35}$$

The expansion coefficients are such that $\tilde{n}(\boldsymbol{r})$ is equal to $n(\boldsymbol{r})$. The force acting upon an ion I can be computed by taking the derivative with respect to the atomic position:

$$\boldsymbol{F}_I = -\nabla_I E . \tag{7.36}$$

All parts of Eq. (7.33) except $E_H[n]$ and $E_{xc}[n]$ can be calculated analytically, since the representation of Eq. (7.34) is used. Only the Hartree and the exchange-correlation terms are treated by a numerical integration on a grid using the plane wave expansion of Eq. (7.35). For the computation of the forces this does not imply any additional problems since only the derivative with respect to the atomic positions is needed. The pressure, in contrary to the forces, is affected by this and so the grid-dependent terms will be more complicated (see Sec. 7.2.3). The forces, however, are evaluated as follows. The derivatives of the density independent terms are given by

$$\begin{aligned} \nabla_I E^{ind} = & \sum_{J \neq I} \frac{\boldsymbol{R}_J - \boldsymbol{R}_I}{|\boldsymbol{R}_J - \boldsymbol{R}_I|^2} \\ & \times \left\{ \frac{Z_I Z_J}{|\boldsymbol{R}_I - \boldsymbol{R}_J|} \operatorname{erfc}\left[\frac{|\boldsymbol{R}_I - \boldsymbol{R}_J|}{\sqrt{R_I^{c\,2} + R_J^{c\,2}}} \right] \right. \\ & \left. + \frac{2}{\sqrt{\pi}} \frac{Z_I Z_J}{\sqrt{R_I^{c\,2} + R_J^{c\,2}}} \exp\left[-\frac{|\boldsymbol{R}_I - \boldsymbol{R}_J|^2}{R_I^{c\,2} + R_J^{c\,2}} \right] \right\} . \end{aligned} \tag{7.37}$$

The different terms arise from the fact that the Ewald sum method [27] is used, as it is commonly implemented in plane wave electronic structure codes. The long range part of all electrostatic interactions is treated in Fourier space, whereas the short range part is treated in real space. This separation is conveniently achieved

for the ionic cores if a Gaussian charge distribution with a width R_I^c is introduced for each nucleus. This leads to the corresponding potential

$$V_I^{core}(\boldsymbol{r}) = -\frac{Z_I}{|\boldsymbol{r}-\boldsymbol{R}_I|}\ \mathrm{erfc}\left[\frac{|\boldsymbol{r}-\boldsymbol{R}_I|}{R_I^c}\right]\ . \tag{7.38}$$

As described in Sec. 2.2.1 the local part of the pseudopotential can be split into a short-ranged $V_{loc}^{SR}(r)$ and a long-ranged part $V_{loc}^{LR}(r)$. The long-ranged part is included in Eq. (7.37) (for details see [24]), so only the short-ranged term has to be treated in the density-dependent part of the forces, which depends directly on the density matrix $P_{\mu\nu}$. The density matrix itself also depends on the atomic positions, but the terms including $\nabla_I P^{\mu\nu}$ can be evaluated when making use of the orthogonality constraints on the wavefunction. This will be described later. First, the forces due to the density-dependent part of the energy in Eq. (7.33) can be written down. For simplicity, E^{core} and $H_{\mu\nu}^{core}$ are defined as the energy and the matrix elements due to the electronic kinetic energy, the short-ranged part of the pseudopotential and the non-local pseudopotential, leading to

$$\begin{aligned}
\nabla_I E^{core} &= \sum_{\mu\nu} \left(\nabla_I P^{\mu\nu}\right) H_{\mu\nu}^{core} + \sum_{\mu\nu} P^{\mu\nu} \left(\nabla_I H_{\mu\nu}^{core}\right) \\
&= \sum_{\mu\nu} \left(\nabla_I P^{\mu\nu}\right) H_{\mu\nu}^{core} \\
&\quad + \sum_{\mu\nu} P^{\mu\nu} \big[2\langle \nabla_I \phi_\mu(\boldsymbol{r})| - \frac{1}{2}\nabla^2 |\phi_\nu(\boldsymbol{r})\rangle \\
&\quad + 2\langle \nabla_I \phi_\mu(\boldsymbol{r})|V_{loc}^{SR}(r)|\phi_\nu(\boldsymbol{r})\rangle \\
&\quad + 2\langle \nabla_I \phi_\mu(\boldsymbol{r})|V_{nl}^{PP}(\boldsymbol{r},\boldsymbol{r}')|\phi_\nu(\boldsymbol{r}')\rangle \\
&\quad + \langle \phi_\mu(\boldsymbol{r})|\nabla_I V_{loc}^{SR}(r)|\phi_\nu(\boldsymbol{r})\rangle \\
&\quad + 2\langle \phi_\mu(\boldsymbol{r})|\nabla_I V_{nl}^{PP}(\boldsymbol{r},\boldsymbol{r}')|\phi_\nu(\boldsymbol{r}')\rangle\big]\ .
\end{aligned} \tag{7.39}$$

The remaining terms $E_H[n]$ and $E_{xc}[n]$ are computed on a real space grid, using the total Hartree potential $v^H(\boldsymbol{r})$, arising from both electronic and nuclear charges (see Sec. 2.3.1) and the exchange-correlation potential $v_{xc}(\boldsymbol{r})$. The total density is defined as

$$n_{tot}(\boldsymbol{r}) = n(\boldsymbol{r}) + n_c(\boldsymbol{r})\ , \tag{7.40}$$

with the core density $n_c(\boldsymbol{r})$. The total potential is given by

$$v_{tot}(\boldsymbol{r}) = v_H(\boldsymbol{r}) + v_{xc}(\boldsymbol{r}) \ . \tag{7.41}$$

Note that $v_{xc}(\boldsymbol{r})$ is only a good quantity in the context of a calculation of forces or pressure. The exchange-correlation potential is defined as

$$v_{xc}(\boldsymbol{r}) = \frac{\partial e_{xc}(n(\boldsymbol{r}))}{\partial n} \ , \tag{7.42}$$

where e_{xc} is the kernel which yields the exchange-correlation energy, if integrated over the whole space (see Eq. (2.56)). This is only valid for LDA functionals, in the case of GGA functionals, the above formula has to be extended accordingly. Since e_{xc} is in general not a linear functional of the density, the energy E_{xc} cannot be computed as integral over the density and the potential, i.e

$$E_{xc} \neq \int d\boldsymbol{r} \ v_{xc}(\boldsymbol{r}) n(\boldsymbol{r}) \ . \tag{7.43}$$

The force due to $E_H[n]$ and $E_{xc}[n]$, however can be obtained from

$$\begin{aligned} \nabla_I E_H[n_{tot}] + \nabla_I E_{xc}[n] & \\ &= \sum_{\mu\nu} \left(\nabla_I P^{\mu\nu}\right) V^{tot}_{\mu\nu} \\ &\quad + 2 \sum_{\mu\nu} P^{\mu\nu} \int d\boldsymbol{r} \ \left(\nabla_I \phi_\mu(\boldsymbol{r})\right) v_{tot}(\boldsymbol{r}) \phi_\nu(\boldsymbol{r}) \\ &\quad + \int d\boldsymbol{r} \ \left(\nabla_I n_c(\boldsymbol{r})\right) v_H(\boldsymbol{r}) \ , \end{aligned} \tag{7.44}$$

where $V^{tot}_{\mu\nu}$ is the matrix element due to Hartree and exchange-correlation energy. In the last step, the derivative of the density matrix $\nabla_I P^{\mu\nu}$ can be evaluated using the orthogonality constraint of the wavefunction. This calculation yields

$$\sum_{\mu\nu} \left(\nabla_I P^{\mu\nu}\right) \left(H^{core}_{\mu\nu} + V^{tot}_{\mu\nu}\right) = -2 \sum_{\mu\nu} W^{\mu\nu} \langle \nabla_I \phi_\mu(\boldsymbol{r}) | \phi_\nu(\boldsymbol{r}) \rangle \ . \tag{7.45}$$

Here, the *energy weighted density matrix* $W^{\mu\nu}$ has been introduced as

$$W^{\mu\nu} = \sum_{i}^{occ} \varepsilon_i P_i^{\mu\nu} \ , \tag{7.46}$$

with the density matrix of the ith orbital and its energy ε_i [24]. The sum is over all occupied orbitals. The contribution actually arises from the orthogonality constraint and is only present if the orbitals depend on the atomic positions. It has originally been derived by Pulay [91].

7.2.2 Grid Independent Terms of the Stress Tensor

In the previous section the computation of the forces in QUICKSTEP has been described. All contributions besides the forces due to the Hartree energy $E_H[n]$ and the exchange-correlation energy $E_{xc}[n]$ are calculated analytically (see Eq.(7.39)) and therefore do not depend on a grid. This simplifies the computation significantly, since the only parameters that have to be considered are the atomic positions $\boldsymbol{R}_I$. Thus, their contribution to the pressure can be evaluated using the virial as derived in Eq. (7.25). In Sec. 7.1.4 it has been stated that the use of absolute positions is ill-defined in a system with periodic boundary conditions, but also the solution using relative coordinates has been introduced in Eq. (7.32). Here, it has been assumed that all contributions are two-body forces, i.e. only involve two atoms at a time. This holds for all terms besides the ones that are due to the pseudopotential. These are of the form

$$\boldsymbol{F}_J^{PP} = \langle \phi_\mu^I(\boldsymbol{r}) | \nabla_J V^J(r) | \phi_\nu^K(\boldsymbol{r}) \rangle \tag{7.47}$$

where $\phi_\mu^I(\boldsymbol{r})$, $V^J(r)$ and $\phi_\nu^K(\boldsymbol{r})$ are located on the atoms I, J and K, respectively. These forces depend on the positions of three atoms. Still, the contribution to the virial can be evaluated similar to Eq. (7.32). If only three atoms, denoted by A, B and C, are considered, the virial is given by

$$\Pi_{ABC}^{vir} = \boldsymbol{F}_A \cdot \boldsymbol{R}_A + \boldsymbol{F}_B \cdot \boldsymbol{R}_B + \boldsymbol{F}_C \cdot \boldsymbol{R}_C \ . \tag{7.48}$$

Since these three atoms form a closed system (at least with respect to the force that they apply to each other), the following can be written

$$\boldsymbol{F}_A + \boldsymbol{F}_B + \boldsymbol{F}_C = \boldsymbol{0} \ , \tag{7.49}$$

or

$$\boldsymbol{F}_A = -\boldsymbol{F}_B - \boldsymbol{F}_C \ . \tag{7.50}$$

If $\boldsymbol{F}_A$ in Eq. (7.48) is replaced using the last relation, the result reads

$$\begin{aligned} \Pi^{vir}_{ABC} &= (-\boldsymbol{F}_B - \boldsymbol{F}_C) \cdot \boldsymbol{R}_A + \boldsymbol{F}_B \cdot \boldsymbol{R}_B + \boldsymbol{F}_C \cdot \boldsymbol{R}_C \\ &= \boldsymbol{F}_B \cdot (\boldsymbol{R}_B - \boldsymbol{R}_A) + \boldsymbol{F}_C \cdot (\boldsymbol{R}_C - \boldsymbol{R}_A) \end{aligned} \tag{7.51}$$

which is of the desired form. Thus, the computation of the grid-independent parts of the virial does not require any additional calculation, because the forces are available and only some summations have to be added.

7.2.3 Grid Dependent Terms of the Stress Tensor

The Hartree energy $E_H[n]$ and the exchange-correlation energy $E_{xc}[n]$ are calculated on a grid, i.e. all quantities are first collocated on a spatial grid and then integrated. This affects the evaluation of the stress tensor in Eq. (7.24), because the transformation of Eq. (7.15) is applied to both atomic coordinates $\boldsymbol{R}_I$ and integrated spatial variables $\boldsymbol{r}$. The necessary terms are derived, following the work of Corso and Resta [92]. They used a completely analytical description, which is not always adequate. The derivation can also be done using sums over grids, which reflects the way, the actual calculation is done. This has been shown by Balbás et al. [93]. Still, this direction will not be followed here, since the derivation becomes quite involved and the basic ideas are not transparent. Therefore, analytical expressions are used, but at some points, results from the calculation on the grid have to be resorted to. Furthermore, in the following, the stress tensor contribution of the exchange-correlation energy will be derived, the Hartree energy can be treated the same way.

The exchange-correlation energy is calculated by

$$E_{xc}[n] = \int d\boldsymbol{r}\ e_{xc}(n, \nabla n)\ . \tag{7.52}$$

The kernel e_{xc} in general depends on the density and the gradient of the density (*gradient corrected functionals*). In this general case, the potential v_{xc} is no longer defined by Eq. (7.42), but the more general formula (see [6])

$$v_{xc}(\boldsymbol{r}) = \frac{\partial e_{xc}}{\partial n} - \frac{\partial}{\partial r_\gamma}\frac{\partial e_{xc}}{\partial(\partial_\gamma n)}\ , \tag{7.53}$$

where $\partial_\gamma n$ is the γth component of the gradient of n. The sum over repeated cartesian components is implicitly understood in the following. First, the contribution that is due to the scaling of the integrated volume treated:

$$\begin{aligned}
\frac{\partial}{\partial h_{\alpha\mu}} E_{xc}[n] &= \frac{\partial}{\partial h_{\alpha\mu}} \int d\boldsymbol{r}\ e_{xc}(n, \nabla n) \\
&= \frac{\partial}{\partial h_{\alpha\mu}} V \int d\boldsymbol{s}\ e_{xc}(n, \nabla n) \\
&= \frac{\partial V}{\partial h_{\alpha\mu}} \int d\boldsymbol{s}\ e_{xc}(n, \nabla n) + V \int d\boldsymbol{s} \frac{\partial}{\partial h_{\alpha\mu}} e_{xc}(n, \nabla n) \\
&= V h^{-1}_{\mu\alpha} \int d\boldsymbol{s}\ e_{xc}(n, \nabla n) + \int d\boldsymbol{r} \frac{\partial}{\partial h_{\alpha\mu}} e_{xc}(n, \nabla n)\ .
\end{aligned} \tag{7.54}$$

The first term is the desired volume term which yields, using Eq. (7.24):

$$\begin{aligned}
-3V\ \Pi^{xc,I}_{\alpha\beta} &= V \sum_\mu h^{-1}_{\mu\alpha} h^T_{\mu\beta} \int d\boldsymbol{s}\ e_{xc}(n, \nabla n) \\
&= \delta_{\alpha\beta} E_{xc}[n]\ .
\end{aligned} \tag{7.55}$$

This result will be added at the end of this derivation and in the following, the rest of the derivative of E_{xc} will be treated as if the volume was independent of $h_{\alpha\mu}$. Now, the derivative of the exchange-correlation kernel will be taken, for which the afore-mentioned functional derivative of the exchange correlation energy is used:

$$-3V\ \Pi^{xc,II}_{\alpha\beta} = \sum_\mu \int d\boldsymbol{r}\ v_{xc}(\boldsymbol{r}) \frac{\partial n}{\partial h_{\alpha\mu}} h^T_{\mu\beta}$$

$$
\begin{aligned}
&= \sum_{\mu} \int d\boldsymbol{r} \left(\frac{\partial e_{xc}}{\partial n} - \frac{\partial}{\partial r_\gamma} \frac{\partial e_{xc}}{\partial(\partial_\gamma n)} \right) \frac{\partial n}{\partial h_{\alpha\mu}} h^T_{\mu\beta} \\
&= \sum_{\mu} \int d\boldsymbol{r} \, \frac{\partial e_{xc}}{\partial n} \frac{\partial n}{\partial h_{\alpha\mu}} h^T_{\mu\beta} - \sum_{\mu} \int d\boldsymbol{r} \, \frac{\partial}{\partial r_\gamma} \frac{\partial e_{xc}}{\partial(\partial_\gamma n)} \frac{\partial n}{\partial h_{\alpha\mu}} h^T_{\mu\beta} \\
&= \qquad\qquad \Pi^{IIa}_{\alpha\beta} \qquad + \qquad\qquad \Pi^{IIb}_{\alpha\beta} \; . \qquad (7.56)
\end{aligned}
$$

The first term $\Pi^{IIa}_{\alpha\beta}$ is left unchanged for now, and the second part $\Pi^{IIb}_{\alpha\beta}$ can be further simplified by using the fact that this integration is actually done on a grid. The gradient of n is approximated numerically based on the values of n on the grid, i.e.

$$
(\partial_\gamma n)_i = \sum_{j=1}^{M} B^\gamma_{ij} n_j \; , \qquad (7.57)
$$

where the sum is over all points of the grid and the coefficients are independent of $\boldsymbol{r}$ [93]. The quantities with indices i and j are the respective values of n and its gradient at point i or j. This means, that the gradient is no longer explicitly dependent on r_γ, only indirectly via n. However, this dependency is already included in the term $\Pi^{IIa}_{\alpha\beta}$. Thus, the second term of Eq. (7.56) can be integrated by parts and the derivative is evaluated as follows:

$$
\begin{aligned}
-3V \; \Pi^{xc,IIb}_{\alpha\beta} &= -\sum_{\mu} \int d\boldsymbol{r} \, \frac{\partial}{\partial r_\gamma} \frac{\partial e_{xc}}{\partial(\partial_\gamma n)} \frac{\partial n}{\partial h_{\alpha\mu}} h^T_{\mu\beta} \\
&= \sum_{\mu} \int d\boldsymbol{r} \, \frac{\partial e_{xc}}{\partial(\partial_\gamma n)} \frac{\partial}{\partial r_\gamma} \frac{\partial n}{\partial h_{\alpha\mu}} h^T_{\mu\beta} \\
&= \int d\boldsymbol{r} \, \frac{\partial e_{xc}}{\partial(\partial_\gamma n)} \frac{\partial n}{\partial r_\alpha} \frac{\partial r_\beta}{\partial r_\gamma} \\
&= \int d\boldsymbol{r} \, \frac{\partial e_{xc}}{\partial(\partial_\gamma n)} \frac{\partial n}{\partial r_\alpha} \delta_{\gamma\beta} \\
&= \int d\boldsymbol{r} \, \frac{\partial e_{xc}}{\partial(\partial_\beta n)} \frac{\partial n}{\partial r_\alpha} \; , \qquad (7.58)
\end{aligned}
$$

where

$$
\sum_{\mu} \frac{\partial n}{\partial h_{\alpha\mu}} h^T_{\mu\beta} = \sum_{\mu} \frac{\partial n}{\partial r_\nu} \frac{\partial r_\nu}{\partial h_{\alpha\mu}} h^T_{\mu\beta}
$$

$$= \sum_{\mu} \frac{\partial n}{\partial r_\nu} \delta_{\nu\alpha} s_\mu h^T_{\mu\beta}$$
$$= \frac{\partial n}{\partial r_\alpha} r_\beta \tag{7.59}$$

has been used. Finally, the term $\Pi^{IIa}_{\alpha\beta}$ will be examined once again. The density n is composed of Gaussian functions

$$n(\boldsymbol{r}) = \sum_{\mu,\nu} P^{\mu\nu} \phi_\mu(\boldsymbol{r}) \phi_\nu(\boldsymbol{r}) \ , \tag{7.60}$$

as described in Eq. (7.34). Since these gaussians are centered at the atomic sites, the actual dependence is of the form

$$\phi_\mu(\boldsymbol{r}) \text{ “} = \text{” } \phi_\mu((\boldsymbol{r} - \boldsymbol{R}_I)^2) \ . \tag{7.61}$$

This means, that the derivative with respect to $h_{\alpha\beta}$ is given by

$$\frac{\partial}{\partial h_{\alpha\mu}} \phi_\nu((\boldsymbol{r} - \boldsymbol{R}_I)^2) = \frac{\partial \phi_\nu}{\partial R_{I\gamma}} \frac{\partial R_{I\gamma}}{\partial h_{\alpha\mu}} + \frac{\partial \phi_\nu}{\partial r_\gamma} \frac{\partial r_\gamma}{\partial h_{\alpha\mu}}$$
$$= (S_{I\mu} - s_\mu) \nabla_{I\alpha} \phi_\nu \tag{7.62}$$

where the symmetry of the derivative has been used. The gradient is a derivative with respect to the atomic coordinates $R_{I\alpha}$, as denoted by the index I. Putting this into Eq. (7.56), the additional term is found as

$$-3V \ \Pi^{xc,IIa}_{\alpha\beta} = \sum_{\mu} \int d\boldsymbol{r} \ \frac{\partial e_{xc}}{\partial n} \frac{\partial n}{\partial h_{\alpha\mu}} h^T_{\mu\beta}$$
$$= 2 \ \sum_{\nu\gamma} P^{\nu\gamma} \int d\boldsymbol{r} \tilde{v}_{xc}(\boldsymbol{r}) \phi_\nu(R_{I\beta} - r_\beta) \nabla_{I\alpha} \phi_\gamma$$
$$+ \sum_{\mu} \sum_{\nu\gamma} \frac{\partial P^{\nu\gamma}}{\partial h_{\alpha\mu}} \int d\boldsymbol{r} \tilde{v}_{xc}(\boldsymbol{r}) \phi_\nu(\boldsymbol{r}) \phi_\gamma(\boldsymbol{r}) \ . \tag{7.63}$$

Again, the fact that the integration on the grid imposes some new rules on the basic quantities has been used. Here, the potential has been denoted as $\tilde{v}_{xc}$. This means that the potential on the grid is employed, which is independent of the gradient, since the gradient of the density is now a function of the density

itself. So, the potential is always given as the derivative of e_{xc} with respect to n. Actually, this is the same potential as used in the calculation of the forces in Eq. (7.44). The second part of the last equation, the derivative of the density matrix can be traced back to a derivative with respect to the atomic coordinates via the chain rule and can thus be treated as described in Sec. 7.2.1. It is, again, a term of the form $\boldsymbol{F} \cdot \boldsymbol{R}_I$.

In conclusion, the additional contributions to the stress tensor due to the exchange-correlation energy that need to be implemented are:

$$\Pi^{xc}_{\alpha\beta} = -\frac{1}{3V}\delta_{\alpha\beta}E_{xc}[n] - \frac{2}{3V}\sum_{\nu\gamma} P^{\nu\gamma} \int d\boldsymbol{r}\tilde{v}_{xc}(\boldsymbol{r})\phi_\nu(R_{I\beta} - r_\beta)\nabla_{I\alpha}\phi_\gamma \\ - \frac{1}{3V}\int d\boldsymbol{r}\ \frac{\partial e_{xc}}{\partial(\partial_\beta n)}\frac{\partial n}{\partial r_\alpha}\ . \tag{7.64}$$

As stated before, the treatment of the Hartree energy is analogous to the exchange-correlation energy. Since the Hartree energy does not involve the gradient of the density, the last term of Eq. (7.64) does not appear. Instead, there is an additional contribution due to the dependency of the kernel on the spatial variables. This can easily be seen if the Hartree energy is written as follows:

$$E_H[n] = \frac{1}{2}\int d\boldsymbol{r}\int d\boldsymbol{r}'\ \frac{n(\boldsymbol{r})n(\boldsymbol{r}')}{|\boldsymbol{r}-\boldsymbol{r}'|}\ . \tag{7.65}$$

It should be noted. that in this case the density n is total density, i.e. the sum of the ionic and electronic contributions. When taking the derivative with respect to $h_{\alpha\mu}$, the kernel $1/|\boldsymbol{r}-\boldsymbol{r}'|$ has to be considered explicitly, as it will give an additional term:

$$\frac{\partial}{\partial h_{\alpha\mu}}\frac{1}{|\boldsymbol{r}-\boldsymbol{r}'|} = \frac{(r_\alpha - r'_\alpha)}{|\boldsymbol{r}-\boldsymbol{r}'|^3}(s'_\mu - s_\mu)\ . \tag{7.66}$$

Putting all parts together, the Hartree contribution to the stress tensor is:

$$\Pi^{H}_{\alpha\beta} = -\frac{1}{3V}\delta_{\alpha\beta}E_H[n] - \frac{2}{3V}\sum_{\nu\gamma} P^{\nu\gamma} \int d\boldsymbol{r}\tilde{v}_H(\boldsymbol{r})\phi_\nu(R_{I\beta} - r_\beta)\nabla_{I\alpha}\phi_\gamma \\ - \frac{1}{6V}\int d\boldsymbol{r}\int d\boldsymbol{r}'\ n(\boldsymbol{r})n(\boldsymbol{r}')\frac{(r_\alpha - r'_\alpha)(r'_\beta - r_\beta)}{|\boldsymbol{r}-\boldsymbol{r}'|}\ . \tag{7.67}$$

Since the potentials v_{xc} and v_H are summed up in QUICKSTEP, yielding a total

potential $v_{tot}(\boldsymbol{r})$, most of the terms for exchange-correlation and Hartree stress can be evaluated in one step. Only the terms due the gradient correction of the exchange-correlation functional and the derivative of the kernel of the Hartree energy are calculated separately.

7.2.4 Test of the Implementation

The stress tensor in its analytical form, as described in the Sections 7.2.2 and 7.2.3, has been implemented in the quantum chemical program CP2K [21], using the routines of the DFT-module QUICKSTEP [24]. For testing purposes, a numerical version of the stress tensor has been implemented additionally. The procedure of the numerical calculation is based on Eq. (7.24), where the derivative of the total energy with respect to the elements $h_{\alpha\beta}$ is obtained via finite differences. This means that for each $h_{\alpha\beta}$ two optimizations of the wavefunction have to be performed, one for a slightly larger and a second one for a smaller $h_{\alpha\beta}$. The differential $dh_{\alpha\beta}$ is typically about 0.001, but the derivative is not sensitive to moderate changes in this value. This also reveals, why molecular dynamics simulations using only numerical stress are not feasible. The procedure would require 19 optimizations per step instead of only one, which, of course, is not desirable.

Both small test-systems (one molecule H_2) and a larger water system, consisting of 64 molecules, taken from a simulation at ambient conditions, have been tested. BLYP was used as exchange-correlation functional and the gaussian basis set was a double-zeta valence basis set with with one set of polarization functions (DZVP). The deviation between the numerical and the analytical stress should not depend on the system itself (only if the energy profile is bad-behaved, what is not expected for these systems) or the basis set, but rather on the accuracy of the wavefunction optimization. This means that the numerical procedure imposes errors on the result rather than the analytical solution, because it depends on the optimization procedure after infinitesimal changes of the system. If the parameters of the calculation are chosen close to typical standard values for a MD simulation (e.g. accuracy of the energy about 10^{-12}), the relative error of the stress (numerical vs. analytical) is about 10^{-6}, which shows that the described implementation yields the correct result.

7.3 Simulation of Liquid Water at Ambient Conditions

7.3.1 Prelude: The NPT Integrator

In the previous sections the calculation of the internal pressure in a given system has been described, including both theoretical and technical details of the implementation. When carrying out an NPT molecular dynamics simulation, i.e. a simulation at constant number of particles N, constant external pressure and constant temperature, a crucial point is the choice of the numerical scheme for integrating the equations of motion. Actually, in an ensemble different from the microcanonical one (NVE), even the equations of motions are not clear. They have to be chosen very carefully, making sure that the desired ensemble is reproduced. The most commonly used algorithms for generating sophisticated ensembles (as NPT or NVT) are based on the *extended-phase-space* approach, in which new, unphysical dynamic variables are introduced in order to maintain the desired conditions (see also Sec. 2.4.4). A famous example are the Nosé-Hoover thermostats that control the kinetic energy fluctuations in a canonical ensemble [94, 95].

Among the various dynamical schemes that have been proposed for generating the NPT ensemble, this work will focus on the algorithm of Martyna, Tobias and Klein (MTK), which has been shown to correctly reproduce the isothermal-isobaric ensemble. Furthermore, the NPT-integrator that is used in CP2K is based on their equations [96]. Since the development and implementation of the integrator has not been part of this work, only the fundamental papers will be summarized and the basic facts will be presented, closely following the work of Tuckerman et al. [97]. The equations of motion of MTK are:

$$
\begin{aligned}
\dot{\boldsymbol{r}}_i &= \frac{\boldsymbol{p}_i}{m_i} + \frac{p_\epsilon}{W}\boldsymbol{r}_i \\
\dot{\boldsymbol{p}}_i &= \boldsymbol{F}_i - \left(1 + \frac{1}{N}\right)\frac{p_\epsilon}{W}\boldsymbol{p}_i - \frac{p_{\eta_1}}{Q_1}\boldsymbol{p}_i \\
\dot{V} &= \frac{dV}{W}p_\epsilon \\
\dot{p}_\epsilon &= 3V(P_{int} - P) + \frac{1}{N}\sum_{i=1}^{N}\frac{\boldsymbol{p}_i^2}{m_i} - \frac{p_{\xi_1}}{Q_1'}p_\epsilon
\end{aligned}
$$

$$
\begin{aligned}
\dot{\eta}_k &= \frac{p_{\eta_k}}{Q_k} \qquad k = 1, \ldots, M \\
\dot{p}_{\eta_k} &= G_k - \frac{p_{\eta_{k+1}}}{Q_{k+1}} p_{\eta_k} \\
\dot{p}_{\eta_M} &= G_M \\
\dot{\xi}_k &= \frac{p_{\xi_k}}{Q'_k} \qquad k = 1, \ldots, M \\
\dot{p}_{\xi_k} &= G'_k - \frac{p_{\xi_{k+1}}}{Q'_{k+1}} p_{\xi_k} \\
\dot{p}_{\xi_M} &= G'_M \ . \qquad (7.68)
\end{aligned}
$$

Here, $\boldsymbol{r}_i$ and $\boldsymbol{p}_i$ are the positions and momenta of the particles, m_i their masses, $\boldsymbol{F}_i$ the corresponding forces. N is the number of particles, d the dimension of the problem (in our case $d = 3$) and V is the volume of the supercell. P is the external pressure and P_{int} the internal pressure, given by Eq. (7.23). Besides the variables corresponding to the particles, there are several unphysical variables, which are the above-mentioned thermostats and the barostat, i.e. artificial particles that couple to the physical system and provide the desired fluctuations of the kinetic energy and internal pressure, as wanted in the isothermal-isobaric ensemble. The thermostats are denoted with η and ξ, where the former couple to the particles and the latter to the barostats. p_ξ and p_η are the respective conjugated momenta. In both cases, chains of thermostats of length M are used. The barostat, that is driven by the difference between the internal and external pressure is the variable p_ϵ. Furthermore, there is an equation for the change of the volume $\dot{V}$, which adapts the cell according to the external pressure. The parameters Q, Q' and W are mass-like parameters, that can be identified with the masses of the unphysical particles and have to be justified in a way that ensures optimal coupling of the thermostats/barostat to the physical system. Finally, the G_k and G'_k are the forces acting on the fictitious variables. They are defined by

$$
\begin{aligned}
G_1 &= \sum_{i=1}^{N} \frac{\boldsymbol{p}_i^2}{m_i} - 3NkT \\
G_k &= \frac{p_{\eta_{k-1}}^2}{Q_{k-1}} \\
G'_1 &= \frac{p_\epsilon^2}{W} - kT
\end{aligned}
$$

$$G'_k = \frac{p^2_{\xi_{k-1}}}{Q'_{k-1}} - kT \ , \tag{7.69}$$

where T is the temperature of the heat-bath. These equations are shown to reproduce the isothermal-isobaric ensemble. They have the conserved quantity

$$H' = H(\boldsymbol{p},\boldsymbol{r}) + \frac{p^2_\epsilon}{2W} + \sum_{k=1}^{M}\left(\frac{p^2_{\eta_k}}{2Q_k} + \frac{p^2_{\xi_k}}{2Q'_k}\right) + 3NkT\eta_1 + kT\sum_{k=2}^{M}\eta_k + kT\sum_{k=1}^{M}\xi_k \ , \tag{7.70}$$

where $H(\boldsymbol{p},\boldsymbol{r})$ is of the typical form

$$H(\boldsymbol{p},\boldsymbol{r}) = \sum_{i=1}^{N}\frac{\boldsymbol{p}_i^2}{2m_i} + U(\boldsymbol{r}_1,\ldots,\boldsymbol{r}_N) \ . \tag{7.71}$$

Note that H' is not a Hamiltonian and Eq. (7.68) cannot be derived from it. The equations of motion have to be integrated numerically in a molecular dynamics simulation. A measure for the quality of the used integration scheme is the conservation of the quantity H'. There are two prerequisites for a good integrator: its time-reversibility and the fact that it is norm-preserving. In contrast to the widespread approach of deriving the integration scheme via a taylor expansion of the position variables, the new approach presented by Tuckerman et al., which is based on the Liouville-operator, provides both properties. This integrator has been implemented in CP2K and is expected to allow for a stable and accurate integration of the MTK equations of motions. Details and tests of the formalism can be seen in [97].

7.3.2 Introduction

Water is the most prevalent liquid on Earth, covering about 70 % of its surface. Water also comprises about 60 % of the mass of an adult human. Consequently, many reactions important to life occur in aqueous solution, and to understand these processes, one must understand how water affects them. Compared to most other liquids, water shows many unique thermophysical properties (e.g., temperature of maximum density at ambient pressure). These are related to its tetrahedral structure and its ability to act as donor and acceptor for two hydrogen bonds.

This causes many difficulties to the understanding of water's properties and thus, it has become a very important field of molecular dynamics simulations. Beginning with the first particle-based simulations of water using pairwise empirical potentials [98], much effort has been devoted to the development of sophisticated empirical water models (e.g. see [99, 100]). Still, these empirical models struggle to provide an accurate description of the complex properties of water, since they cannot reproduce its electronic properties correctly. Therefore, ab-initio methods have been used during the last decade to shed light on water's physical and chemical properties [101, 102].

The first of these simulations used 32 molecules in the microcanonical ensemble and was run for $\approx$ 3.5 ps [101]. Today, simulations are carried out using 64 or 128 molecules and are extended to more than 10 ps. But still all of these simulations are limited to either microcanonical or canonical ensembles. Using the newly implemented analytical pressure calculation in CP2K a molecular dynamics simulation in the isobaric-isothermal ensemble will be presented in this work. Recently, a paper investigating the influence of different exchange-correlation functionals, density cutoff and even the method of generating the grids, used for numerical integrations, on the resulting density of water at ambient pressure has been published [103]. In this case, a Monte Carlo approach has been used, molecular dynamics techniques are used here.

7.3.3 Technical Details

The first-principles simulations have been performed with the program CP2K [21], a code for Born-Oppenheimer molecular dynamics, in contrary to CPMD [20], which employs the Car-Parrinello scheme. As mentioned before (see Sec. 2.3.1 or Sec. 7.2.1), the DFT module, called QUICKSTEP, is using a combined Gaussian and plane waves basis set. The integration of the equations of motion has been done as described in Sec. 7.3.1.

Seven different molecular dynamics simulations of 64 water molecules have been conducted, yielding trajectories between 12 and 22 ps. Four runs have used the BLYP functional, the remaining three the PBE functional (see Sec. 2.1.6). In all cases, the norm-conserving pseudopotentials of Goedecker and co-workers (GTH)

[18] have been applied, the Gaussian basis set was a triple-zeta valence basis set augmented with two sets of d-type or p-type polarization functions (TZV2P). This basis set has been shown to give converged structural and dynamical properties for liquid water at constant volume [80]. The effect of the density cutoff has also been investigated, but only for BLYP. Therefore, two calculations have been conducted. One of them with a cutoff of 280 Ry, the second with 600 Ry. In this context, the method to generate of the grids used for the numerical integration of the exchange-correlation and the Hartree potential (see Sec. 7.2.1) is important. Since the volume of the supercell is changed in every step of the simulation, the grids have to be regenerated in each step. In principle, to methods are possible. First, the number of grid points can be kept constant, leading to a different cutoff in each step (i.e. the density of the points is variable). Second, the density of the points can be kept constant, yielding a constant cutoff. Both approaches have been used here. If the former one is employed, the grid is generated on a reference cell with constant size and then rescaled to the instantaneous cell size. In this case, a larger or smaller reference cell, compared to the expected simulation cell can be used. This will be called LARGE-REF or SMALL-REF, respectively. The method without reference cell is called NO-REF. For the testing the effect of the cutoff, the LARGE-REF method has been chosen. According to the work of McGrath et al. [103], a density of 0.8 g/cm^3 is expected, corresponding to a cubic cell of length 13.4 Å. The LARGE-REF and SMALL-REF are using reference cells that yield a density of 0.76 and 0.93 g/cm^3, respectively. The used cutoffs are 600 Ry and 750 Ry, which have been chosen to yield a cutoff of 700 Ry at 0.8 g/cm^3. The NO-REF simulations have been carried out with a cutoff of 600 Ry. The first simulation has been started from a geometry with density 1 g/cm^3, arbitrary points from this trajectory have been used as starting geometry for the other runs. This is not expected to have any influence on the results, since the simulations are run until they are equilibrated, anyway.

For the dynamics simulation, the time step was 0.48 fs. Nosé-Hoover-thermostats have been applied to the dynamical variables (including the barostat). The temperature has been set to 330 K and the time constant to 16.68 fs (corresponding to 2000 cm^{-1}). The external pressure was 1 bar and the time constant of the barostat 300 fs.

7.3.4 Results

The first runs have been made for exploring the effect of the density cutoff on the results. Although a density cutoff of 280 Ry is usually considered sufficient for converged energy and forces, a recently published work of McGrath and others [103] reveals, that for isobaric simulations a higher cutoff can be necessary. There, Monte-Carlo techniques have been used and it is not clear if their arguments still hold for a molecular dynamics simulation. Therefore, two LARGE-REF simulations with a density cutoff of 280 Ry and 600 Ry, respectively, have been conducted. In the cited paper, a cutoff of 1200 Ry has been used. Still, in this work 600 Ry has been used, because this is already a very high cutoff, which is commonly not used in a MD simulation and the gain in accuracy with 1200 Ry is expected to be much smaller than the higher computational cost. One MD-step takes 13s for 280 Ry, but 27s for 600 Ry, using 64 processors. In Fig. 7.1 the conserved quantity from Eq. 7.70 is shown for both runs.

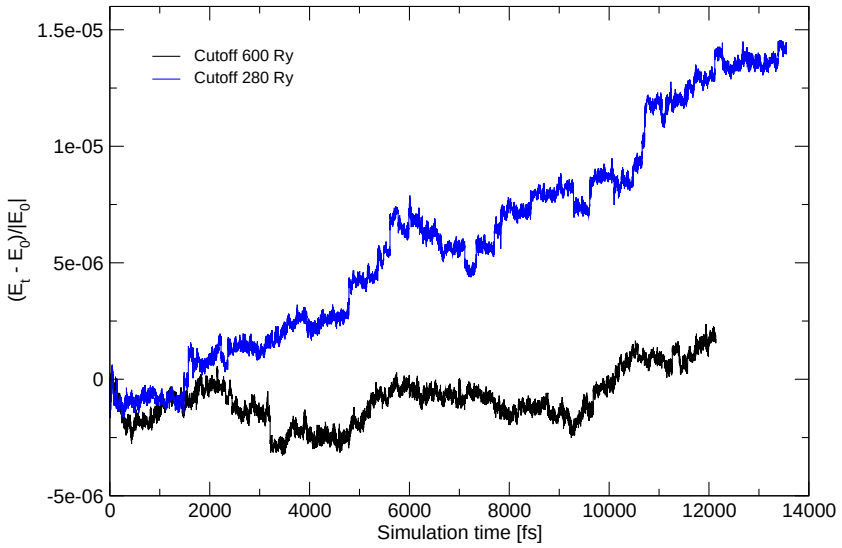

Figure 7.1: Relative change of the conserved quantity during a Born-Oppenheimer NPT simulation of water (normalized to the value at $t = 0$). The blue line is taken from a MD using a density cutoff of 280 Rydberg, the black line was computed at 600 Rydberg. In both cases a large reference cell has been used.

As expected, it can be seen that the conservation is much better for the high cutoff. But it should be noted that even for 280 Ry the conservation is quite good. The observed relative drift of $1.5 \cdot 10^{-5}$ after 14 ps is corresponding to

approximately $5 \cdot 10^{-6}$ a.u. per atom per ps. Even a MD run in the much simpler NVE-ensemble is not expected to give a significantly better conservation [24]. In conclusion, the conserved quantity does not justify the very high cutoff of 600 Ry, although, however, this run yields an excellent conservation. In the above-cited work, the run with a low cutoff resulted in an incorrect density of the simulated water, so this parameter will be explored, too. It can be seen in Fig. 7.2. The density seems to be significantly influenced by the density cutoff, although it is not clear if only the convergence with respect to the volume of the supercell is slower with the low cutoff or if the system really tends to a higher density. Even after 12-14 ps the curves are not yet completely converged, the 280 Ry run seems to show a movement towards smaller densities at the end, but this can also be due to statistics. Since McGrath et al. find a density between 0.78 and 0.8 g/cm^3, it seems reasonable that the high cutoff of 600 Ry is necessary for reliable results. Still, it is not clear why the cutoff should have this influence on a property as the density, since this is mainly driven by the barostat. The only parameters that are depending on the cutoff and used by the barostat, are the forces, which, in general, are considered to be converged even at 280 Ry. Although this questions is very interesting, it will not be discussed further here. In order to avoid problems related to this issue, in the following all simulations will be done at a very high cutoff, i.e. approximately 600 Ry. The approximate value is given here, because, as explained in Sec. 7.3.3, the cutoff is not constant when using the reference-cell method.

Water simulations using an ab-initio approach are known to yield overstructured water [29]. This is an inherent problem of the description using DFT, especially due to the exchange-correlation functionals. As already seen in Fig. 7.2, the density tends to values about 0.8 g/cm^3, which obviously smaller than the experimental value at ambient conditions. After exploring the effect of the density cutoff, six long MD runs have been started. Three of them use BLYP, the others PBE. For both cases the three methods LARGE-REF, SMALL-REF and NO-REF are used. This should reveal the effect of the exchange-correlation functionals on the density. As reported in [29], simulations of water using PBE result in a even more structured liquid than BLYP. More structured in this context means, that the hydrogen bonds between the molecules are stronger and thus, the liquid is

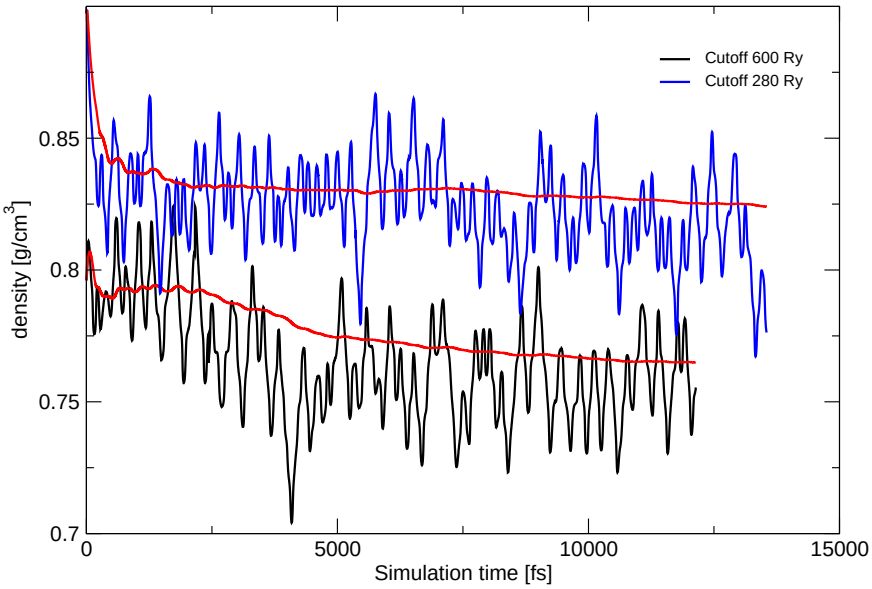

Figure 7.2: Calculated density during a NPT simulation of water. The blue line is taken from a MD using a density cutoff of 280 Rydberg, the black line was computed at 600 Rydberg. In both cases a large reference cell has been used. The red lines show the cumulative average.

more ice-like, leading to a lower density. So, the density calculated using PBE is expected to be even below 0.8 g/cm^3.

Before looking at macroscopic and measurable properties, the quality of the MD runs by means of the conserved quantity should be investigated. The evolution of the conserved quantity during the simulations are shown in Fig. 7.3. The BLYP-NO-REF run exhibits are long-term drift of about $1 \cdot 10^{-5}$ a.u. per atom per ps. This is, as explained above, still reasonable. Still, the other runs do not show such a drift, or at least a very small one, in the range of $2 \cdot 10^{-6}$ per atom per ps, which is an excellent value. Interestingly, the PBE simulations in general have a smaller drift than the BLYP runs, which again reveals the influence of the used functional on the simulation. In the BLYP case, the LARGE-REF shows the best conservation. SMALL-REF exhibits lots of small steps in the conserved quantity. This is usually expected for NO-REF, since with constant cutoff, the number of grid points changes, which leads to sudden jumps in the energy. The reason, why this happened only in the SMALL-REF run is not clear, but it does not cause a non-reversible drift.

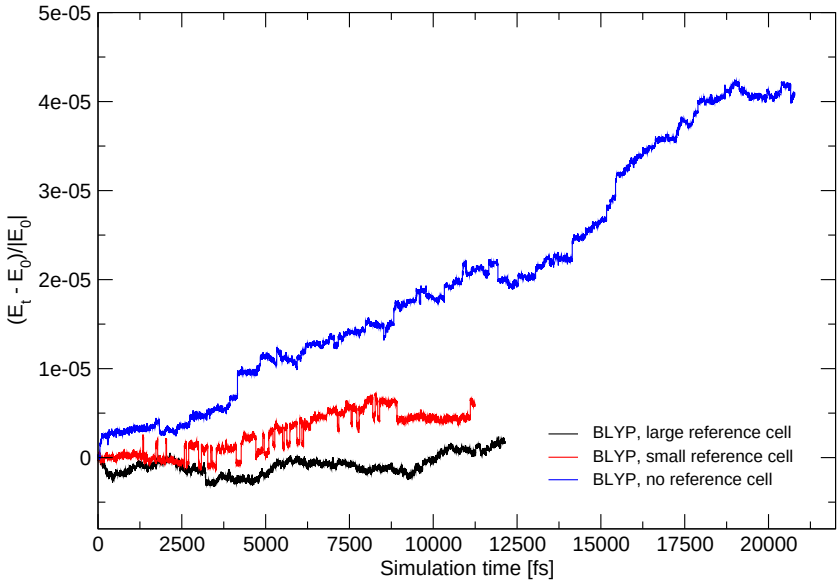

(a) BLYP

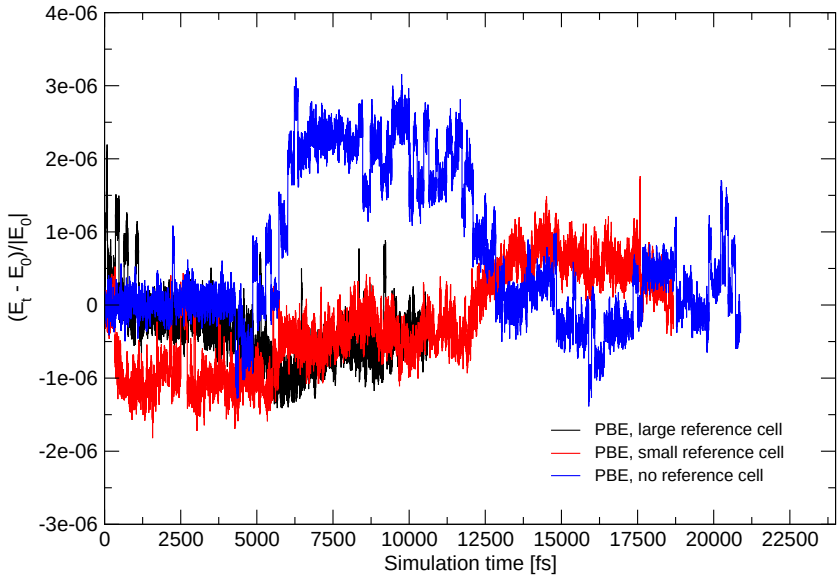

(b) PBE

Figure 7.3: Relative change of the conserved quantity during a Born-Oppenheimer NPT simulation of water (normalized to the value at $t = 0$).

The internal pressure has been computed during the simulation as described in the previous sections. First of all, because it is needed for the NPT integration scheme (see Eq. (7.68)), but of course the instantaneous pressure also contains information about the system. In Fig. 7.4 and Fig. 7.5 the evolution of the internal pressure is shown. Although the external pressure is 1 bar, the fluctuations of the internal pressure reach a maximum of approximately 10 kbar. This seems to be very unlikely, but the definition of the pressure has to kept in mind. It is given by the pressure estimator of Eq. (7.11). Actually, the average of this quantity over the whole phase space yields the pressure, but here, only the instantaneous value of the estimator is taken. The average of the instantaneous pressure values is also given in Fig. 7.4 and Fig. 7.5, as well as the standard deviation. The averages, which are about 100 bar, are close to 1 bar, if the small number of particles is considered, which is 192, and the statistical error resulting from this. Additionally, these are not equilibrated runs, but simulations starting from an arbitrary density. This means, that even during the equilibration, which comprises almost the whole run, the instantaneous pressure fluctuates around the external constraint. Looking at the standard deviations, it can be seen, that the fluctuations in the BLYP simulations are about 3 kbar, whereas the the PBE functional yields 3.5 kbar. Also, the averages in the BLYP case seem to be a bit closer to 1 bar, but this might be due to statistics.

From the pressure alone it can hardly be judged whether BLYP or PBE gives better results for water at ambient conditions. The critical quantity is the density that the system reaches after equilibration. Fig. 7.6 depicts the density simulated in the BLYP runs, both instantaneous values and cumulative averages are shown. Obviously the equilibration of the system takes a long time, at least 10 ps are necessary. SMALL-REF yields the slowest convergence, even after 12 ps there are still large fluctuations. LARGE-REF and NO-REF give similar results. The reason for this behavior, though, is not clear. Fig. 7.7 contains the same information, taken from the PBE simulations. Again, 10 ps are needed for equilibration and SMALL-REF gives the largest fluctuations. Still, the reason is not obvious, since LARGE-REF and SMALL-REF are constructed to result in comparable grids for similar cell sizes. Finally, in Fig. 7.8, the densities from the different cell-construction methods and the two functionals are summarized. Although very

long trajectories, i.e. at least 12 ps, have been calculated, the volume cannot be considered converged completely. A final length of 20 ps for each run should be the aim, which could not be accomplished in this work. Still, the grid construction is not expected to affect the equilibrated density significantly. All three methods agree within 5-10%. The BLYP average is

$$\rho_{BLYP} = 0.76 \pm 0.03 \mathrm{g/cm^3} \ ,$$

whereas PBE yields

$$\rho_{PBE} = 0.87 \pm 0.01 \mathrm{g/cm^3} \ .$$

This means that the density from a simulation using the PBE exchange-correlation functional is significantly closer to the experimental density of 1 g/cm^3. The values are close to the findings of simulations using Monte-Carlo techniques (BLYP: [103], PBE: [104]). These results are surprising, since one can consider PBE the better functional for simulating water from the point of the NPT simulations, whereas NVT simulations have shown that PBE is even more overstructured than BLYP [29]. Recently, a paper has been published by Lee and Tuckerman, that uses a discrete variable representation (DVR) basis set to expand the Kohn-Sham orbitals [82]. This allows for carrying out simulations very near the complete basis set limit. They find, that the radial distribution function is significantly less overstructured than in comparable simulations using plane waves or Gaussian functions. In contradiction to that, it has been reported [104], that a BLYP simulation with an even higher cutoff leads to a worse density. This is a serious issue that has to be investigated in future work.

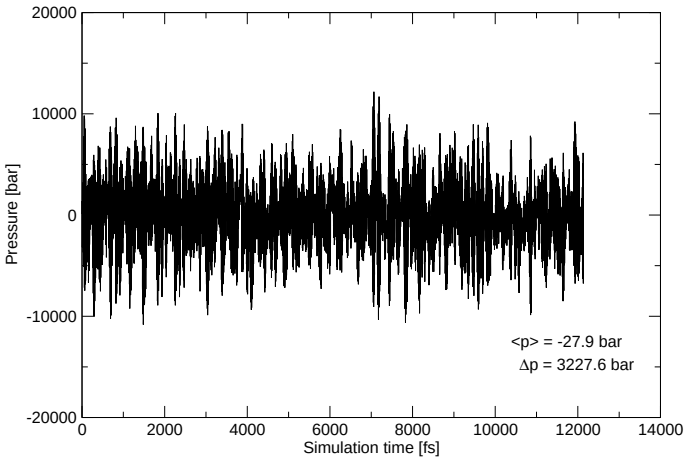

(a) large reference cell

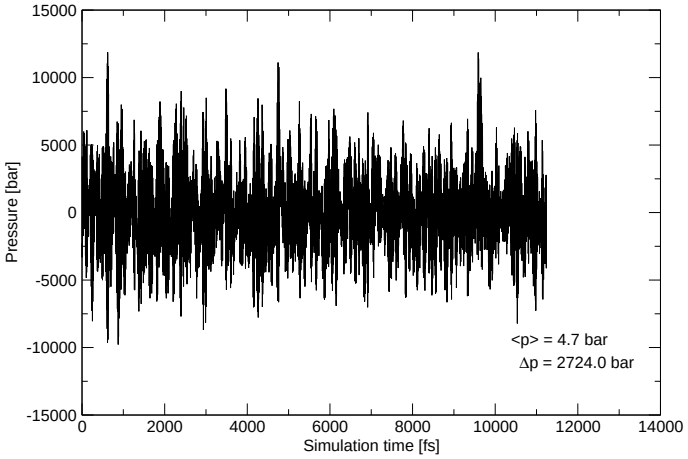

(b) small reference cell

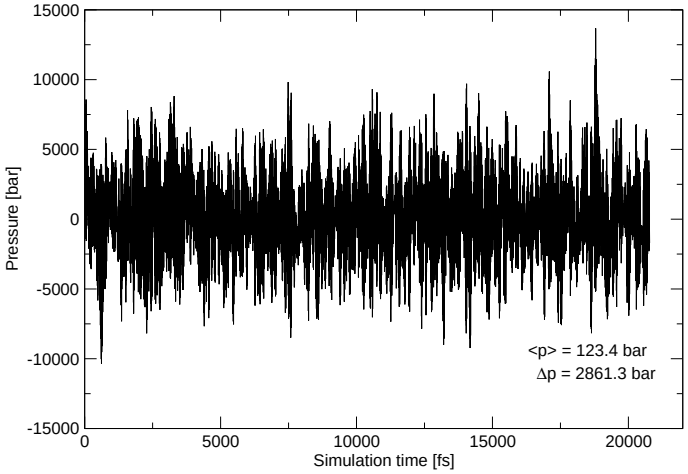

(c) no reference cell

Figure 7.4: Instantaneous pressure during a Born-Oppenheimer NPT simulation of water using the BLYP functional. Simulations with a large, small and without reference cell have been performed. Both the average ($< p >$) and the standard deviation (Δp) are given.

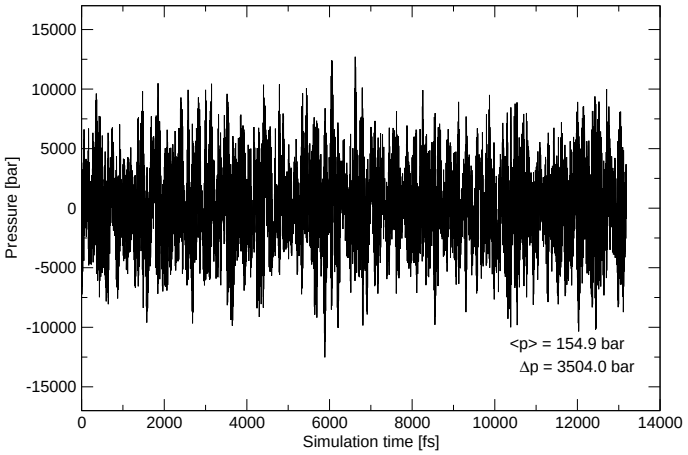

(a) large reference cell

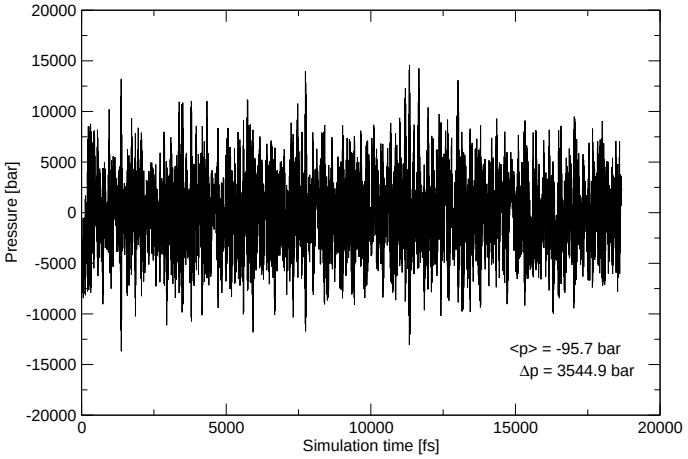

(b) small reference cell

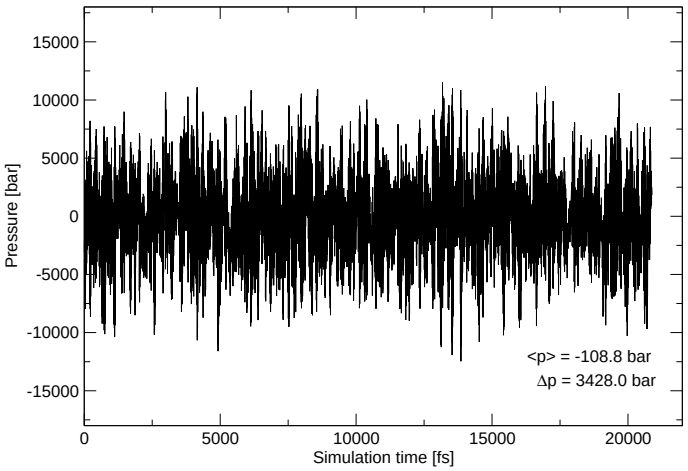

(c) no reference cell

Figure 7.5: Instantaneous pressure during a Born-Oppenheimer NPT simulation of water using the PBE functional. Simulations with a large, small and without reference cell have been performed. Both the average ($< p >$) and the standard deviation (Δp) are given.

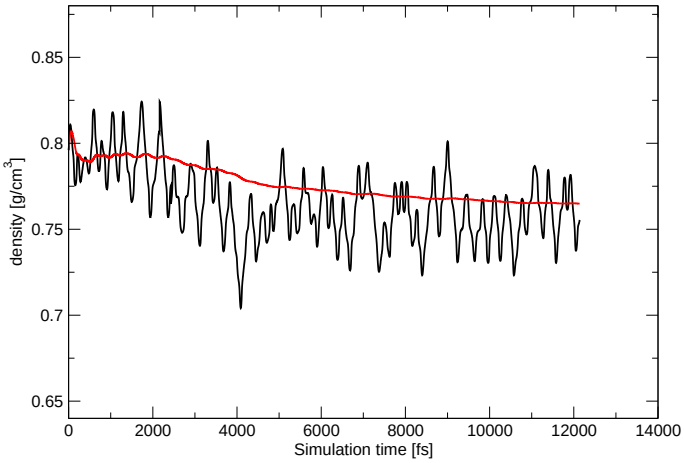

(a) large reference cell

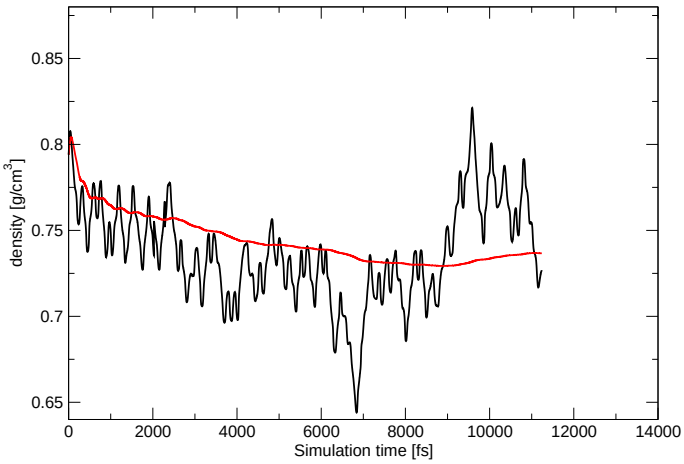

(b) small reference cell

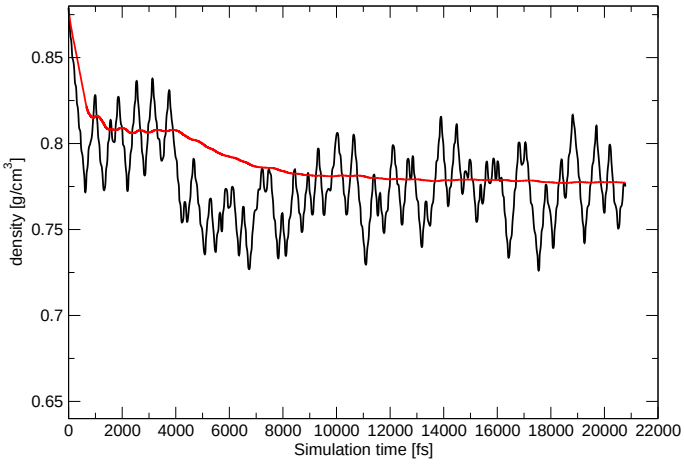

(c) no reference cell

Figure 7.6: Instantaneous density during a Born-Oppenheimer NPT simulation of water using the BLYP functional. Simulations with a large, small and without reference cell have been performed. The red line shows the cumulative average.

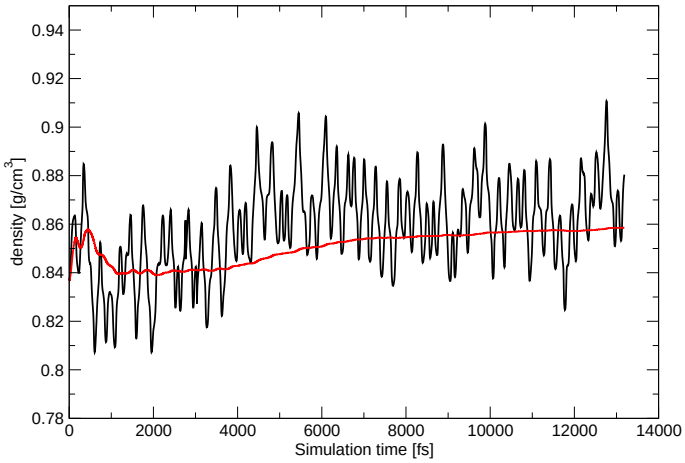

(a) large reference cell

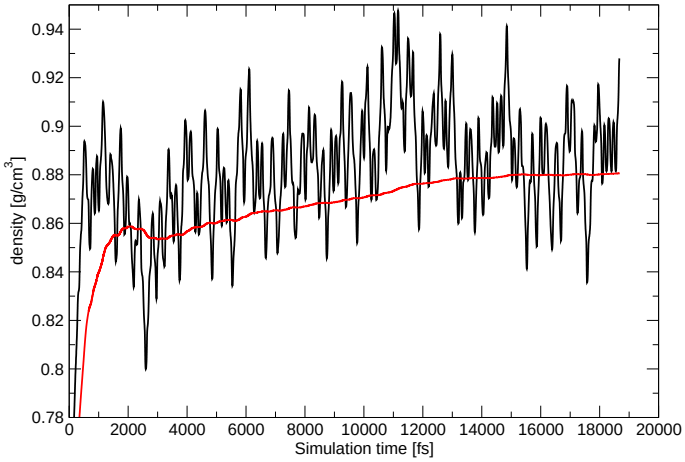

(b) small reference cell

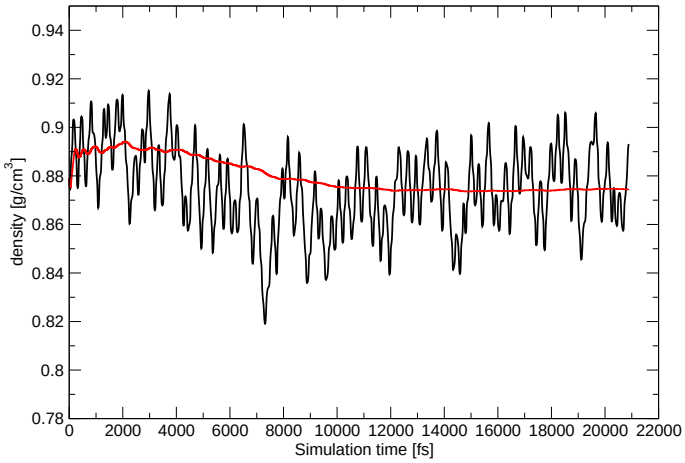

(c) no reference cell

Figure 7.7: Instantaneous density during a Born-Oppenheimer NPT simulation of water using the PBE functional. Simulations with a large, small and without reference cell have been performed. The red line shows the cumulative average.

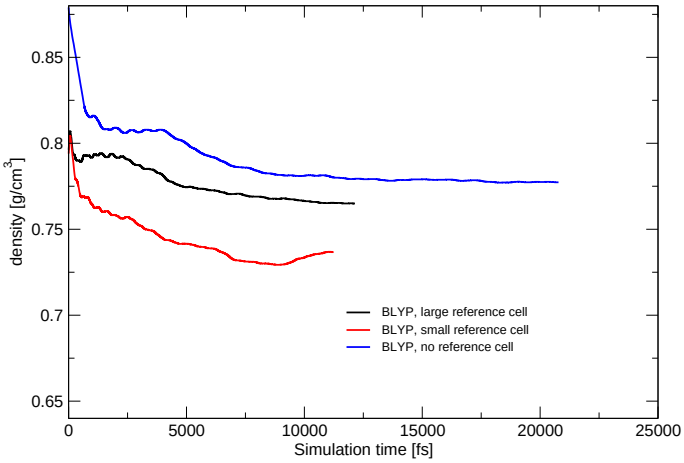

(a) BLYP

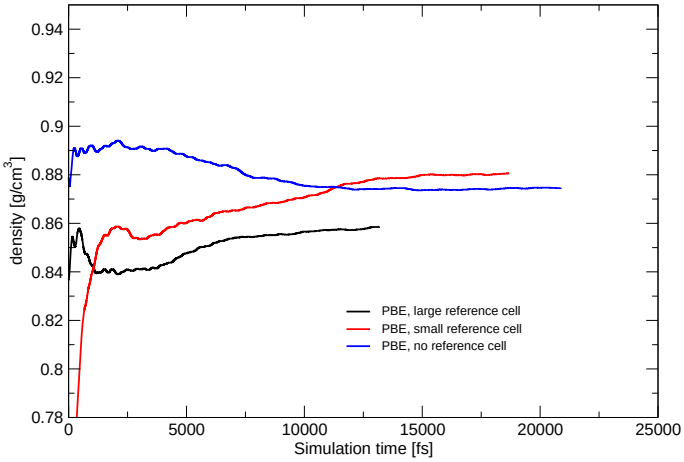

(b) PBE

Figure 7.8: Cumulative average of the density of water from a NPT simulation using BLYP (Fig. 7.8(a)) and PBE (Fig. 7.8(b)).

7.4 Conclusions

In this chapter, the theoretical and technical details of a pressure calculation within the GPW framework have been presented, as implemented in CP2K. Numerical tests have shown that the analytical formulae, that have been derived before, yield correct results and can be used in a molecular dynamics simulation in the isobaric-isothermal ensemble.

Finally, extended simulations on liquid water at ambient conditions have been performed. The performance of the CP2K package for the first time enabled such long runs on a relatively large system, containing 64 molecules. Within this study, the effect of the density cutoff, different schemes for setting up the simulation cell and two different exchange-correlation functionals on macroscopic properties, such as the density of the liquid, have been explored. It turned out that a very high density cutoff is necessary for equilibrating the cell volume with respect to the external pressure, whereas the method, how to set up the instantaneous cell, did not show a significant influence. The most important point is, that the functionals, BLYP and PBE, resulted in much different densities. PBE, in this case, seems to be the functional that can produce results closer to the experiment, whereas it has been shown to be worse for other ensembles. This contradiction should be investigated further in future work.

Additionally, the general formulation of the stress tensor, as presented here, enable simulations using non-isotropic pressure. This means that stress can be applied in certain directions. The possibility can be used for the exploration of non-isotropic effects, as known from piezoelectric materials.

8 Summary and Outlook

The aim of molecular dynamics simulations is the realistic description of physical systems. This was also the central theme of this work, where especially NMR parameters have been considered. Such quantities are generally more demanding to obtain than pure energetics and dynamics, because additional manipulations, such as linear response calculations, are necessary. Still, this effort pays off when comparing the results to experiment. The accessibility of experimental data enables the direct assessment of the simulation, and likewise, the calculation helps with the interpretation of measured spectra.

Often, only equilibrium values of spectroscopic parameters are evaluated. For this purpose the structure of the system is optimized and subsequently, the respective quantities are computed. Although this approach turns out to be justified in many cases, for a simulation to give a complete depiction of the physical situation the statistical fluctuations of the considered ensemble have to be incorporated. This can be achieved by a combination of molecular dynamics and property calculations, which is the route that was followed in this work. Furthermore, not only the distribution due to thermal fluctuations have been investigated, but also nuclear quantum effects, which are commonly neglected in similar approaches.

Statistical fluctuations such as motion at finite temperature and nuclear quantum effects are especially pronounced in hydrogen-bonded systems. Hydrogen bonds are known to be crucial for the structure of many chemical and biological systems. Furthermore, hydrogen-bonded protons can easily be exchanged with deuterons, making isotope effects accessible to the experiment. In this work, both intramolecular hydrogen bonds (as in acetylacetone, Sec. 5.3), and intermolecular bonds (in benzoic acid, Sec. 5.4) have been treated. A large part of this work has been devoted to the structure and dynamics of water, a system with a very complex behavior, mainly due to its hydrogen bond network.

Using a path integral ansatz, that allows the rigorous treatment of nuclear quantum effects, the influence of the quantum nature of the nuclei on NMR parameters has been explored. It has been shown that the experimental isotope effect on the NMR chemical shift of the hydrogen bonded atom in acetylacetone can be reproduced. It is due to tunneling of the respective proton, which is suppressed for the deuteron, because of the higher mass. Similarly, the NQCC is subject to quantum effects. While the electric field gradient (EFG) a proton would experience if it had an electric quadrupole moment is reduced by 30% compared to that seen by the deuteron, the asymmetry parameter is raised by tunneling. The reasons could be attributed to the transition state, where the proton is "chemically" in a symmetric position with respect to hydrogen bond acceptor and donator, with a rather asymmetric EFG. This symmetric configuration is not accessible if tunneling is not possible, resulting in the significant differences in the NMR parameters. In the simulation, an isolated molecule has been considered for facilitating the computation. Therefore, the findings concerning the NQCC cannot be compared directly to experiment. In the next step, the same procedure will be applied to crystalline acetylacetone, enabling the comparison of both chemical shift and NQCC to experimental data.

In addition, the deuteron NQCC of benzoic acid has been studied. Recently, it has been shown that it exhibits a pronounced temperature dependence. Therefore, nuclear quantum effects were expected to be important, too. The hydrogen bond length is comparable to the bond length in acetylacetone, where large effects due to tunneling could be found. It turned out that this is not the case for benzoic acid, where the EFG is unchanged. A possible reason is that in benzoic acid a simultaneous tunneling of two protons is necessary, which is much more unlikely.

In the second part of the work the quadrupole relaxation in water has been calculated. This, again, was possible by combining a molecular dynamics simulation with property calculations, here of EFGs. In a framework using periodic boundary conditions, often pseudopotentials are employed for reducing the computational effort. Unfortunately, the calculation of spectroscopic properties as the NMR chemical shift or EFGs suffers severely from this. In this work the GAPW method has been used, which enables the calculation of all-electron wave functions even in a periodic framework without a significantly higher computa-

tional cost. The EFGs have been computed for both oxygens and deuterons along an extended trajectory, yielding relaxation times via the autocorrelation function of this parameter. The comparison with experimental data revealed a remarkable agreement. This shows that molecular dynamics simulations not only give a statistical sampling of the available phase space, but also resemble the physical time evolution, which is necessary for the autocorrelation functions. Furthermore, an analysis of the microscopic dynamics revealed, that the relaxation is almost exclusively influenced by local effects. The correlation of the EFG corresponds to the local orientation of the respective molecule, while long-ranged effects of the cluster do not contribute. Thus, not only a computational description of the relaxation process via quadrupole interactions has been achieved, using a consistent level of theory for the whole simulation, also the accuracy of the GAPW method was shown. In addition, the comparison of calculated relaxation times to experimental values enable the assessment of the explicit dynamics yielded by the simulation, instead of only the average structure. The agreement of experiment and computation shows that both the time evolution and the EFGs in GAPW are of a very good quality. The GAPW scheme therefore opens the way for the calculation of NMR chemical shifts for heavier atoms, that are usually treated with pseudopotentials, which was problematic before.

The above-mentioned GAPW calculations have been conducted with the quantum chemical code CP2K. It combines the advantages of various techniques, e.g. mixed basis sets, resulting in a very fast, but still accurate code. While the above simulations have been carried out in a canonical ensemble, i.e. the number of particles, volume and temperature are kept constant, the experimental situation is often described by a given pressure rather than a fixed volume. A dynamics scheme resembling this setup relies on the computation of the internal pressure of the system. This has been implemented into the CP2K code. The simultaneous usage of plane waves and Gaussians as a basis is often favorable, but the implementation of new features is complicated by the fact that both real space and reciprocal space contributions have to be considered. Finally, a successful computational scheme was found and constant pressure simulations of water have been carried out using the new routines. Simulations of water at ambient conditions had been done before with a Monte Carlo scheme, but the results shown here are the first

extended constant pressure molecular dynamics simulations of water. In contrast to the simulation in Chapter 6, here the volume of the simulated cell was not fixed, but equilibrated to the externally applied pressure. Within this study the effect of the density cutoff, technical details of the grid construction and two different exchange-correlation functionals, PBE and BLYP, on the calculated density has been investigated. It turned out that the choice of the exchange-correlation function is crucial for the quality of the results. Both functionals yielded overstructured water, as expected, but PBE performed significantly better.

In conclusion, this work has shown that state-of-the-art quantum chemical methods can yield valuable and accurate information about molecular systems. Even complex quantities, such as nuclear quantum effects or relaxation in liquids can be modeled appropriately. Thus, both statistical averages and the actual time evolution are accessible with the help of modern computational schemes, based on a first-principles approach without empirical parameters. In the future, the combined application of different techniques, such as constant pressure simulations and property calculations, will lead to computational descriptions that are very close to the experimental setup, resulting in new insights and interpretations of data, bridging the gap between theory and experiment.

A Derivation of the Stress Tensor

In this section conventions and symbols as introduced in Sec. 7.1.3 are used. Atomic positions are transformed from absolute coordinates to scaled coordinates according to

$$\boldsymbol{R}_I = \mathbf{h} \cdot \boldsymbol{S}_I \ , \quad \text{with } S_{Ii} \in [0,1[\ , i = 1,2,3 \ . \tag{A.1}$$

The matrix $\mathbf{h}$ is again composed of the three lattice vectors:

$$\mathbf{h} = [\boldsymbol{a}_1, \boldsymbol{a}_2, \boldsymbol{a}_3] \ . \tag{A.2}$$

This means that the volume of the unit cell can be calculated as

$$V = \det \mathbf{h} \ . \tag{A.3}$$

Since the derivatives of the volume with respect to the elements of $\mathbf{h}$ are needed, an alternative representation of the determinant will be used, given by

$$V = \det \mathbf{h} = \exp\left\{\mathrm{Tr} \ln \mathbf{h}\right\} \ . \tag{A.4}$$

The matrix $\mathbf{h}$ is diagonalizable, because it is composed of three vectors that are linearly independent of each other. Then a matrix $\mathbf{D}$ can be found with

$$\mathbf{h}' = \mathbf{D}^{-1} \mathbf{h} \mathbf{D} \tag{A.5}$$

and $\mathbf{h}'$ is the respective diagonal matrix. The logarithm of a matrix as used in Eq. (A.4) is defined as

$$\ln \mathbf{h} = \mathbf{D} \left(\ln \mathbf{h}'\right) \mathbf{D}^{-1} \ . \tag{A.6}$$

In this equation $\ln \mathbf{h}'$ is the matrix $\mathbf{h}'$ where each diagonal element has been replaced by its logarithm. Additionally, it should be noted that the trace of a

matrix is similarity invariant, i.e. $\mathrm{Tr}\,(\mathbf{h}) = \mathrm{Tr}\,(\mathbf{D}^{-1}\mathbf{h}\mathbf{D})$. Using these relations, the derivative of the volume with respect to a matrix element $h_{\alpha\beta}$ can be calculated:

$$\begin{aligned}
\frac{\partial V}{\partial h_{\alpha\beta}} &= \frac{\partial \det\mathbf{h}}{\partial h_{\alpha\beta}} = \frac{\partial}{\partial h_{\alpha\beta}} \exp\left\{\mathrm{Tr}\ln\mathbf{h}\right\} \\
&= V\frac{\partial}{\partial h_{\alpha\beta}}\left(\mathrm{Tr}\mathbf{D}\ln\mathbf{h}'\mathbf{D}^{-1}\right) \\
&= V\frac{\partial}{\partial h_{\alpha\beta}}\left(\sum_i \ln h'_{ii}\right) \\
&= V\sum_i \frac{1}{h'_{ii}}\frac{\partial h_{ii}}{\partial h_{\alpha\beta}} \\
&= V\sum_i D_{\beta i}\left(h'^{-1}\right)_{ii} D^{-1}_{i\alpha} \\
&= V\left(h^{-1}\right)_{\beta\alpha} \\
&= V\left(h^{-1}\right)^T_{\alpha\beta} \ .
\end{aligned} \tag{A.7}$$

In the fifth line the relation

$$h'_{ii} = \sum_{jk} D^{-1}_{ij} h_{jk} D_{ki} \tag{A.8}$$

has been employed. Besides the derivatives of the volume, the derivative of an element of the inverse matrix $\mathbf{h}^{-1}$ with respect to an $h_{\alpha\mu}$ is needed. This can be found by starting with the obvious relation

$$\sum_\nu h^{-1}_{i\nu} h_{\nu\delta} = \delta_{i\delta} \ . \tag{A.9}$$

The derivative with respect to $h_{\alpha\mu}$ yields zero on the right side.

$$\begin{aligned}
\frac{\partial}{\partial h_{\alpha\mu}}\sum_\nu h^{-1}_{i\nu} h_{\nu\delta} = 0 &= \sum_\nu \frac{\partial h^{-1}_{i\nu}}{\partial h_{\alpha\mu}} h_{\nu\delta} + \sum_\nu h^{-1}_{i\nu}\delta_{\alpha\nu}\delta_{\mu\delta} \\
&= \sum_\nu \frac{\partial h^{-1}_{i\nu}}{\partial h_{\alpha\mu}} h_{\nu\delta} + h^{-1}_{i\alpha}\delta_{\mu\delta}
\end{aligned} \tag{A.10}$$

If both sides are multiplied with $h^{-1}_{\delta j}$ and summed over δ, the previous equation reads

$$\sum_{\nu\delta} \frac{\partial h^{-1}_{i\nu}}{\partial h_{\alpha\mu}} h_{\nu\delta} h^{-1}_{\delta j} = -\sum_{\delta} h^{-1}_{i\alpha} \delta_{\mu\delta} h^{-1}_{\delta j}$$

$$\frac{\partial h^{-1}_{ij}}{\partial h_{\alpha\mu}} = -h^{-1}_{i\alpha} h^{-1}_{\mu j} \ , \tag{A.11}$$

which is the desired relation.

B Technical Details: Simulations

The simulations presented in Chapters 5 and 6 have been run on the following two clusters, which are located at the Max Planck Insitute for Polymer Research in Mainz. Typically, a run consisted of 32 parallel processes.

The first one is a 16-node double-processor single-core Opteron cluster (32 processors) with MyriNet PCI-D (cable) high-speed low-latency interconnect. The single-core Opteron machines are running at 2.2 GHz and have 2 GB of RAM per node.

The second cluster has 16 nodes with double-processor dual-core Opterons (64 processors) using a MyriNet PCI-X (optical) high-speed low-latency interconnect. The Opterons are running at 2.4 GHz and have 2 GB of RAM per node.

The simulations presented in Chapter 7 have been performed on computers located at the Lawrence Livermore National Laboratory. The following clusters have been used, with typically 64 parallel processes.

ATLAS is a cluster consisting of 1152 nodes. Each node has 8 AMD dual-core Socket F Opterons, running at 2.4 GHz, and 16 GB of RAM. The cluster communicates via an Infiniband interconnect, yielding a system peak performance of 44.24 TFLOPS.

THUNDER has 1024 nodes with 4 processors per node. The processor type is Intel Itanium2 Madison Tiger4, running at 1.4 GHz. There are 8 GB of RAM per node and a Quadrics switch interconnect is used for communication. The system peak performance is 22.9 TFLOPS.

C Technical Details: NMR Measurements

The NMR experiments were carried out with 8mg of protonated Acetylaetone, purchased from Aldrich (Nr.: 123-54-6) and used withour further purification and deuterated Acetylacetone, synthesized from the protonated sample following the method described in reference [105]. The data was collected on a Bruker DRX spectrometer with a 16,4 T magnet operating at Larmor frequencies of 700,13 MHz (for ^{1}H) and 107,61 MHz (for ^{2}H) . The AvanceII console, also manufactured by Bruker, was responsible for pulse generation, data acquisition and data digitizing. A double resonance NMR probe was used that supports rotors with an outer diameter of 2,5 mm and a sample volume of approximately 10 μl. Since anisotropic interactions do not play a role in liquid media the sample rotation was set to the relatively low spinning frequency of 5 kHz and helped in that way averaging out sample inhomogeneities and magnetic susceptibility effects. In both the ^{1}H and ^{2}H one pulse experiments $\frac{\pi}{2}$-pulses with a length of 2.5 μs and an excitation profile covering 100 kHz of spectral width were applied to the spinning sample. 64 scans were performed and a four step phase cycling was applied to cancel out resonance offsets and effects of pulse imperfections. The sample was kept at ambient temperature of 300 K while keeping the bearing gas temperature constant using Bruker's BVT-1000 temperature control unit.

Referencing of the ^{1}H-NMR-Signal was conducted by first measuring the resonance frequency of water ω_{H_2O} and comparing this to $\omega_{ref} = 4.8$ ppm [106]. From the difference of those values a *shift reference* $\Delta\omega(^1H) = \omega_{ref} - \omega_{H_2O}$ arised that was used to shift the axis of the recorded spectra.

Referencing of the ^{2}H-NMR-Signal was conducted by first measuring the resonance frequency of deuterium oxide ω_{D_2O} and comparing this to $\omega_{ref} = 4.8$ ppm. The shift reference for the corresponding ^{2}H-NMR spectra could be determined following $\Delta\omega(^2H) = \omega_{ref} - \omega_{D_2O}$. The ^{2}H shift reference was cross checked with

a sample of deuterated solid Dimethylsulfone (ν_R = 20 kHz, rotor synchronized acquisition) whose ^{2}H resonance frequency appeared at 3.15 ppm.

D Atomic units

In this work, as in the respective literature, *atomic units* instead of the Gaussian or SI-system are used, leading to a significant simplification of many equations. This is achieved by a transformation of the variables, so that the charge and mass of the electron, as well as $\hbar$ do not appear explicitly anymore. In the following, the applied procedure is summarized briefly.

If the well-known SI system of units is used, the Schrödinger equation for the hydrogen atom is given by

$$\left[-\frac{\hbar^2}{2m_e}\nabla^2 - \frac{e^2}{4\pi\varepsilon_0 r}\right]\phi = E\phi \ , \tag{D.1}$$

where m_e is the electron mass, e the electron charge and ε_0 is the permittivity of free space. Now, the coordinate system is transformed, i.e. $x, y, z \to \lambda x', \lambda y', \lambda z'$. The derivative with respect to the position is changed to

$$\nabla = \left(\frac{\partial}{\partial x}, \frac{\partial}{\partial y}, \frac{\partial}{\partial z}\right) = \frac{1}{\lambda}\left(\frac{\partial}{\partial x'}, \frac{\partial}{\partial y'}, \frac{\partial}{\partial z'}\right) = \frac{1}{\lambda}\nabla' \ . \tag{D.2}$$

The distance r is also scaled by the factor λ (let the nucleus be situated at $\boldsymbol{R}_N = (0,0,0)$):

$$r = \sqrt{x^2 + y^2 + z^2} = \lambda\sqrt{x'^2 + y'^2 + z'^2} \ . \tag{D.3}$$

Thus, the Schrödinger equation in the transformed system reads:

$$\left[-\frac{\hbar^2}{2m_e\lambda^2}\nabla'^2 - \frac{e^2}{4\pi\varepsilon_0\lambda r'}\right]\phi' = E\phi' \ . \tag{D.4}$$

In the next step, the factors attached to the operators of the kinetic and potential energy, are eliminated. Therefore, these prefactors are equated and an appropriate

Physical quantity	Conversion factor X	Value of X
Length	a_0	5.2918×10^{-11} m
Mass	m_e	9.1095×10^{-31} kg
Charge	e	1.6022×10^{-19} C
Energy	$\mathcal{E}_a$	4.3598×10^{-18} J
Angular momentum	$\hbar$	1.0546×10^{-34} Js
Electric field gradient	$\mathcal{E}_a e^{-1} a_0^{-2}$	9.7185×10^{21} Vm^{-2}

Table D.1: Conversion factors between SI- and atomic units for some physical quantities.

λ is tried to be found:

$$\frac{\hbar^2}{m_e \lambda^2} = \frac{e^2}{4\pi\varepsilon_0 \lambda} \equiv \mathcal{E}_a \ . \tag{D.5}$$

Solving Eq. (D.5) for λ yields:

$$\lambda = \frac{4\pi\varepsilon_0 \hbar^2}{m_e e^2} = a_0 \ . \tag{D.6}$$

Thus, λ is the Bohr constant a_0, which is the appropriate length scale in atomic units, the unit itself is simply called *bohr*. Substituting Eq. (D.5) into Eq. (D.4), the Schrödinger equation reads:

$$\mathcal{E}_a \left[-\frac{1}{2}\nabla'^2 - \frac{1}{r'} \right] = E\phi' \ . \tag{D.7}$$

The known form of the Schrödinger equation can be obtained, if the energy is scaled by $\mathcal{E}_a$. This means, that the energy is also given in a new unit, called *hartree*.

$$\left(-\frac{1}{2}\nabla'^2 - \frac{1}{r'} \right) = E'\phi' \ . \tag{D.8}$$

The exact conversion factor can be calculated, if the ground state of the hydrogen atom is considered. This yields an energy of -0.5 hartree, corresponding to the well-known -13.6 eV. Using this as starting point, one can easily evaluate the conversion factors for all desired quantities. Table D.1 shows some examples. The value of a quantity in the SI system, Q, can thus be found by multiplying the value in atomic units Q' by the respective conversion factor X:

$$Q \ = \ XQ' \ . \tag{D.9}$$

E Abbreviations

a.u.	atomic units
BLYP	Becke Lee Yang Parr
BO	Born Oppenheimer
CPMD	Car Parrinello Molecular Dynamics
DFT	Density Functional Theory
EFG	Electric Field Gradient
GAPW	Gaussian and Augmented Plane Waves
GGA	Generalized Gradient Approximation
GIAO	Gauge Including Atomic Orbitals
GPW	Gaussian and Plane Waves
GTH	Goedecker Teter Hutter
HF	Hartree Fock
IGLO	Individual Gauges for Localized Orbitals
KS	Kohn Sham
LDA	Local Density Approximation
MD	Molecular Dynamics
NICS	Nuclear Independent Chemical Shift
NMR	Nuclear Magnetic Resonance
NQCC	Nuclear Quadrupole Coupling Constant
PBE	Perdew Burke Ernzerhof
PIMD	Path Integral Molecular Dynamics
ppm	parts per million
Ry	Rydberg
xc	Exchange Correlation

Bibliography

[1] R. Car and M. Parrinello, Phys. Rev. Lett. **55**, 2471 (1985).

[2] I. N. Levine, *Quantum Chemistry*, Prentice-Hall Inc., New Jersey (USA), 2000.

[3] M. Born and H. Kun, *Dynamical Theory of Crystal Lattices*, Oxford University Press, Walton Street, Oxford, 1954.

[4] A. Messiah, *Quantum Mechanics: Vol 1*, Dover Publications Inc., 2000.

[5] P. Hohenberg and W. Kohn, Phys. Rev. **136**, B864 (1964).

[6] R. G. Parr and W. Yang, *Density functional theory of atoms and molecules*, Oxford Science Publications, 1989.

[7] W. Kohn and L. J. Sham, Phys. Rev. **140**, A1133 (1965).

[8] J. P. Perdew and M. Levy, Phys. Rev. B **56**, 16021 (1997).

[9] D. M. Ceperley and B. J. Alder, Phys. Rev. Lett. **45**, 566 (1980).

[10] S. H. Vosko, L. Wilk, and M. Nusair, Can. J. Phys. **58**, 1200 (1980).

[11] B. Y. Tong and L. J. Sham, Phys. Rev. **144**, 1 (1966).

[12] A. D. Becke, Phys. Rev. A **38**, 3098 (1988).

[13] C. Lee, W. Yang, and R. G. Parr, Phys. Rev. B **37**, 785 (1988).

[14] J. Tao and J. P. Perdew, Phys. Rev. Lett. **91**, 146401 (2003).

[15] D. Marx and J. Hutter, Ab-initio molecular dynamics: Theory and implementation, in *Modern Methods and Algorithms in Quantum Chemistry*, volume 1 of *NIC Series*, pages 301–449, Forschungzentrum Juelich, 2000.

[16] W. C. Topp and J. J. Hopfield, Phys. Rev. B **7**, 1295 (1973).

[17] M. Fuchs and M. Scheffler, Computer Physics Communications **119**, 67 (1999).

[18] S. Goedecker, M. Teter, and J. Hutter, Phys. Rev. B **54**, 1703 (1996).

[19] E. E. Pickett, Comput. Phys. Reports **9**, 115 (1989).

[20] J. Hutter et al., Computer code CPMD, version 3.12, 1990-2005, Copyright IBM Corp. and MPI-FKF Stuttgart, `http://www.cpmd.org`.

[21] J. Hutter, Computer code CP2K, 2000-2007, `http://cp2k.berlios.de`.

[22] N. W. Ashcroft, *Solid state physics*, Saunders, Philadelphia, 1976.

[23] G. Lippert, J. Hutter, and M. Parrinello, Mol. Phys. **92**, 477 (1997).

[24] J. VandeVondele et al., Computer Physics Communications **167**, 103 (2005).

[25] G. Lippert, J. Hutter, and M. Parrinello, Theor. Chem. Acc. **103**, 124 (1999).

[26] M. Krack and M. Parrinello, Phys. Chem. Chem. Phys. **2**, 2105 (2000).

[27] M. Allen and D. Tildesley, *Computer Simulations of Liquids*, Clarendon Press Oxford, 1987.

[28] P. Tagney, J. Chem. Phys. **124**, 044111 (2006).

[29] I.-F. W. Kuo et al., J. Phys. Chem. B **108**, 12990 (2004).

[30] J. Schmidt and D. Sebastiani, J. Chem. Phys. **123**, 074501 (2005).

[31] H. C. Anderson, J. Chem. Phys. **72**, 2384 (1980).

[32] S. Nosé, J. Chem. Phys. **81**, 511 (1984).

[33] W. G. Hoover, Phys. Rev. A **31**, 1695 (1985).

[34] G. J. Martyna, M. L. Klein, and M. E. Tuckerman, J. Chem. Phys. **97**, 2635 (1992).

[35] W. Kutzelnigg, Theochem-J Mol Struc **202**, 11 (1989).

[36] C. P. Slichter, *Principles of Magnetic Resonance*, Springer Verlag Berlin Heidelberg, 1990.

[37] J. D. Jackson, *Classical electrodynamics*, J. Wiley and sons, New York, 1962.

[38] K. Gottfried and T.-M. Yan, *Quantum Mechanics: Fundamentals*, Springer Verlag, 2004.

[39] K. Schmidt-Rohr and H. W. Spiess, *Multidimensional Solid-State NMR and Polymers.*, Academic Press, Inc., 1994.

[40] H. M. Petrilli, P. E. Blöchl, P. Blaha, and K. Schwarz, Phys. Rev. B **57**, 14690 (1998).

[41] H. W. Spiess, B. B. Garrett, R. K. Sheline, and S. W. Rabideau, J. Chem. Phys. **51**, 1201 (1969).

[42] H. W. Spiess, *NMR - Basic Principles and Progress, Dynamic NMR Spectroscopy*, 15, 55, Springer Verlag, 1978.

[43] A. Abragam, *Principles of Nuclear Magnetism*, Oxford University Press, 1961.

[44] A. Putrino, D. Sebastiani, and M. Parrinello, J. Chem. Phys. **113**, 7102 (2000).

[45] D. Sebastiani, *Development of a new ab initio approach for NMR chemical shifts in periodic systems*, PhD thesis, Universität Stuttgart, 2001.

[46] R. Ditchfield, J. Chem. Phys. **56**, 5688 (1972).

[47] W. Kutzelnigg, Isr. J. Chem. **19**, 193 (1980).

[48] T. A. Keith and R. F. W. Bader, Chem. Phys. Lett. **210**, 223 (1993).

[49] D. Marx and M. Parrinello, Z. Phys. B Cond. Mat. **95**, 143 (1994).

[50] M. Tuckerman, D.Marx, M. Klein, and M. Parrinello, J. Chem. Phys. **104**, 5579 (1996).

[51] R. P. Feynman, Rev. Mod. Phys. **20**, 367 (1948).

[52] D. Ceperley, Rev. Mod. Phys. **67**, 279 (1995).

[53] C. Pierleoni, D. M. Ceperley, B. Bernu, and W. R. Magro, Phys. Rev. Lett. **73**, 2145 (1994).

[54] D. Marx and M. Parrinello, J. Chem. Phys. **104**, 4077 (1996).

[55] M. Sprik, M. L. Klein, and D. Chandler, J. Chem. Phys. **83**, 3042 (1985).

[56] L. Knoll and D. Marx, Eur. Phys. J. D **10**, 353 (2000).

[57] D. A. Case, J. Biomol. NMR **15**, 95 (1999).

[58] T. Metzroth, *Struktur- und Reaktionsaufklärung durch Kombination von Theorie und Experiment: Anwendungen und methodische Aspekte der Quantenchemie*, Phd thesis, Johannes Gutenberg-Universität Mainz, 2006.

[59] M. Schulz-Dobrick, T. Metzroth, H. W. Spiess, J. Gauss, and I. Schnell, ChemPhysChem **6**, 315 (2005).

[60] L. D. Fosdick and H. F. Jordan, Phys. Rev. **143**, 58 (1966).

[61] M. E. Tuckerman and G. J. Martyna, J. Phys. Chem. B **104**, 159 (2000).

[62] S. Rossano, F. Mauri, C. J. Pickard, and I. Farnan, J. Phys. Chem. B **198**, 7245 (2005).

[63] J. L. Burdett and M. T. Rogers, J. Am. Chem. Soc. **86**, 2105 (1964).

[64] I. Matanovic and N. Doslic, J. Phys. Chem. A **109**, 4185 (2005).

[65] J. Schmidt, *Analyse experimenteller NMR-Parameter in Festkörpern mittels Computersimulation*, Diplomarbeit, Johannes Gutenberg-Universität Mainz, 2004.

[66] J. T. Hynes, J. P. Klinman, H.-H. Limbach, and R. L. Schowen, editors, *Hydrogen-Transfer Reactions*, volume 2, Wiley-VCH, Weinheim, 2007.

[67] C. Deller, private communication, 2007.

[68] A. Hoffmann and I. Schnell, private communication, 2004.

[69] C. S. Tautermann, A. F. Voegele, and K. R. Liedl, J. Chem. Phys. **120**, 631 (2004).

[70] F. H. Allen, Acta Crystallogr. **B58**, 380 (2002).

[71] G. Bruno and L. Randaccio, Acta Cryst. Sect. B **36**, 1711 (1980).

[72] B. B. Garrett, A. B. Denison, and S. W. Rabideau, J. Phys. Chem. **71**, 2606 (1967).

[73] T. Tsukahara, M. Harada, H. Tomiyasu, and Y. Ikeda, J. of Supercritical Fluids **26**, 73 (2003).

[74] J. G. Powles, M. Rhodes, and J. H. Strange, Mol. Phys. **11**, 515 (1966).

[75] M. Luhmer and J. Reisse, Progress in Nuclear Magnetic Resonance Spectroscopy **33**, 57 (1998).

[76] E. H. Hardy et al., J. Chem. Phys. **119**, 6184 (2003).

[77] R. Baumert, R. Ludwig, and A. Geiger, J. Mol. Model. **2**, 379 (1996).

[78] H. Huber, Chem. Phys. Lett. **112**, 133 (1984).

[79] M. J. Frisch et al., Computer code Gaussian 98, Revision A.7, 1998.

[80] J. VandeVondele et al., J. Chem. Phys. **122** (2005).

[81] I.-F. W. Kuo, private communication, 2007.

[82] H.-S. Lee and M. E. Tuckerman, J. Chem. Phys. **125**, 154507 (2006).

[83] A. K. Soper, F. Bruni, and M. A. Ricci, J. Chem. Phys. **106**, 247 (1997).

[84] A. K. Soper, Chem. Phys. **258**, 121 (2000).

[85] G. Hura, J. M. Sorenson, R. M. Glaeser, and T. Head-Gordon, J. Chem. Phys. **113**, 9140 (2000).

[86] J. M. Sorenson, G. Hura, R. M. Glaeser, and T. Head-Gordon, J. Chem. Phys. **113**, 9149 (2000).

[87] P. Pyykkö, Mol. Phys. **99**, 1617 (2001).

[88] B. Kirchner, D. J. Searles, A. J. Dyson, P. S. Vogt, and H. Huber, J. Am. Chem. Soc. **122**, 5379 (2000).

[89] M. E. Tuckerman, Statistical mechanics lecture notes, 2003, `http://www.nyu.edu/classes/tuckerman/stat.mech/`.

[90] D. A. McQuarrie, *Statistical Mechanics*, HarperCollinsPublishers Inc., 10 East 53rd Street, New York, N.Y. 10022, 1976.

[91] P. Pulay, Mol. Phys. **17**, 167 (1969).

[92] A. D. Corso and R. Resta, Phys. Rev. B **50**, 4327 (1994).

[93] L. C. Balbás, J. L. Martins, and J. M. Soler, Phys. Rev. B **64**, 165110 (2001).

[94] W. G. Hoover, Phys. Rev. A **31**, 1695 (1985).

[95] D. Frenkel and B. Smit, *Understanding Molecular Simulation*, Academic Press, Inc., 525 B Street, Suite 1900, San Diego, CA 92101-4495, USA, 1996.

[96] G. J. Martyna, D. J. Tobia, and M. L. Klein, J. Chem. Phys. **101**, 4177 (1994).

[97] M. E. Tuckerman, J. Alejandre, R. López-Rendón, A. L. Jochim, and G. J. Martyna, Journal of Physics A **39**, 5629 (2006).

[98] J. P. Barker and R. O. Watts, Chem. Phys. Lett. **3**, 144 (1969).

[99] W. L. Jorgensen, J. Chandrasekhar, J. D. Madura, R. W. Impey, and M. L. Klein, J. Chem. Phys. **79**, 926 (1983).

[100] B. Chen, J. Xing, and J. I. Siepmann, J. Phys. Chem. B **104**, 2391 (2000).

[101] K. Laasonen, M. Sprik, M. Parrinello, and R. Car, J. Chem. Phys. **99**, 9080 (1993).

[102] I.-F. W. Kuo and C. J. Mundy, Science **303**, 658 (2004).

[103] M. J. McGrath et al., ChemPhysChem **6**, 1894 (2005).

[104] C. J. Mundy, private communication, 2007.

[105] H. Ogoshi and K. Nakamotu, J. Chem. Phys. **45**, 3113 (1966).

[106] H. Gottlieb, V. Kotlyar, and A. Nudelman, J. Org. Chem. **62**, 7512 (1997).